The non-linear evolution of edge localized modes

Ronald Wenninger

München 2012

The non-linear evolution of edge localized modes

Ronald Wenninger

Dissertation

der Fakultät für Physik
der Ludwig–Maximilians–Universität
München

durchgeführt am
Max–Planck–Institut für Plasmaphysik

vorgelegt von
Ronald Wenninger
aus München

München, den 17.10.2012

Erstgutachter: Prof. Dr. Harald Lesch
Zweitgutachter: Prof. Dr. Hartmut Zohm
Tag der mündlichen Prüfung: 09.01.2013

Zusammenfassung

Edge localized modes (ELMs) sind Instabilitäten am Rand von Tokamakplasmen in Regimes mit hoher Einschlussqualität (H-mode). Ohne ELMs ist der Transport in der Randschicht herkömmlicher Plasmen in H-mode zu niedrig, um einen stationärer Zustand zu ermöglichen. Andererseits wird angenommen, dass große, nicht abgeschwächte ELMs in zukünftigen, größeren Fusionsanlagen Leistungsflussdichten im Divertor verursachen, die weit über den Toleranzgrenzen vorhandener Materialien liegen. Deshalb ist es unerlässlich, das Ausmaß des Energieverlustes pro ELM und die resultierende ELM-Frequenz in solchen Anlagen kontrollieren zu können. Um im Verständnis der Fragen fortzuschreiten, wodurch ELM-Größen determiniert sind und wie Methoden zu ihrer Abschwächung funktionieren, ist es notwendig, die nichtlineare Entwicklung der Erosion des Plasmarandes möglichst genau zu charakterisieren. Um dies zu erreichen werden experimentelle Daten mit Ergebnissen einer ELM-Simulation unter Verwendung des Codes JOREK (reduzierte, nichtlineare MHD) verglichen. Hierbei wird eine eigens entwickelte *synthetische magnetische Diagnostik* angewendet. Die experimentellen Daten werden mit einigen Diagnostiken mit hoher Abtastrate an den Fusionsexperimenten ASDEX Upgrade und TCV in einer Vielzahl von toroidalen und poloidalen Positionen gemessen.

Ein zentrales Element dieser Arbeit bildet die detaillierte Charakterisierung von dominanten magnetischen Störungen während ELMs. Diese Signaturen der Instabilität können am deutlichsten zeitlich nahe dem Beginn der Erosion des Plasmarandes beobachtet werden. Dominante magnetische Störungen werden von Stromstörungen verursacht, welche auf oder innerhalb der letzten geschlossenen Flussfläche lokalisiert sind. Unter gewissen Voraussetzungen weisen dominante magnetische Störungen - wie andere in H-mode beobachtete Randschichtinstabilitäten - Ähnlichkeiten zu Solitonen auf. Außerdem werden sie erwartungsgemäß häufig korreliert mit Störungen der Elektronentemperatur beobachtet.
An TCV ist es möglich, die zeitliche Entwicklung der toroidalen Struktur von dominanten magnetischen Störungen zu charakterisieren. Die toroidalen Störungsprofile zu allen Zeitschritten vom Überschreiten des Hintergrund-Fluktuationsniveaus bis hin zum Erreichen des maximalen Störungsniveaus sind ähnlich zueinander. Dies ist ein Zeichen für nichtlineare Kopplung. Für die meisten ELMs ist die zugehörige dominante toroidale Modennummer 1. Dies führt in Übereinstimmung mit linearen und nichtlinearen MHD-Rechnungen zu der Schlussfolgerung, dass es von der linearen zur nichtlinearen Phase einen Übergang von mittleren ($n \approx 10$) zu niedrigen ($n \approx 1$) dominanten toroidalen Modennummer gibt. Deshalb ist es besonders wichtig, die Frage der ELM-Größe mit nichtlinearen Instrumenten zu behandeln. Weiterhin wird die Frage gestellt, ob die Interaktion dieser nichtlinearen Störung mit der Gefäßwand zu einer vorübergehenden Sättigung der Störung führen kann.
Um das Verständnis der ELM-Entwicklung voranzutreiben, werden dominante magnetische Störungen mit ELM-Signaturen korreliert, die typischerweise vorher (Kohärente Vorläufer

von ELMs) bzw. nachher (ELM-Filamente) beobachtet werden. Der Transport während ELMs ist von einer Konkurrenz zwischen prallelem Transport zum Divertor und Transport in radial ausgeworfenen ELM-Filamenten geprägt. Eine spezielle Analysemethode zur verbesserten Korrelation von dominanten magnetischen Störungen und ELM-Filamenten wird im Rahmen dieser Arbeit entwickelt. Die darauf basierende Beobachtung, dass beide Strukturen sich in unterschiedliche senkrechte Richtungen bewegen, kann hinsichtlich der starken Verscherung der senkrechten Rotation in diesem radialem Bereich verstanden werden. Außerdem haben dominante magnetische Störungen Eigenschaften vergleichbar zu einem Auslöser für die radiale Bewegung von ELM-Filamenten.

Die im Rahmen dieser Arbeit gesammelten Ergebnisse ermöglichen die Entwicklung einer Vorstellung der Vorgänge während ELMs, welche vollständiger ist als alle vorher entwickelten. Es wird erwartet, dass dies zu einem erweiterten Verständnis von ELMs und Methoden zu ihrer Abschwächung sowie zu einem Modell von ELMs beiträgt, das die Vorhersage ihrer Ausmaße und Entwicklung ermöglicht.

Abstract

Edge localized modes (ELMs) are instabilities in the edge of tokamak plasmas in the high confinement regime (H-mode). Without them the edge transport in ordinary H-mode plasmas is too low to establish a stationary situation. However in a future device large unmitigated ELMs are believed to cause divertor power flux densities far in excess of tolerable material limits. Hence the size of energy loss per ELM and the resulting ELM frequency must be controlled. To proceed in understanding how the ELM size is determined and how ELM mitigation methods work it is necessary to characterize the non-linear evolution of pedestal erosion. In order to achieve this experimental data is compared to the results of ELM simulations with the code JOREK (reduced MHD, non-linear) applying a specially developed *synthetic magnetic diagnostic*. The experimental data is acquired by several fast sampling diagnostics at the experiments ASDEX Upgrade and TCV at a large number of toroidal/poloidal positions.

A central element of the presented work is the detailed characterization of dominant magnetic perturbations during ELMs. These footprints of the instability can be observed most intensely in close temporal vicinity to the onset of pedestal erosion. Dominant magnetic perturbations are caused by current perturbations located at or inside the last closed flux surface. In ASDEX Upgrade under certain conditions dominant magnetic perturbations like other H-mode edge instabilities display a similarity to solitons. Furthermore - as expected - they are often observed to be correlated to a perturbation of electron temperature.
In TCV it is possible to characterize the evolution of the toroidal structure of dominant magnetic perturbations. Between growing above the level of background fluctuations and the maximum perturbation level for all time instance a similar toroidal structure is observed. This rigid mode-structure is an indication for non-linear coupling. Most frequently the dominant toroidal mode number is **1**. Consistent with linear and non-linear MHD calculations this leads to the conclusion that the dominant toroidal mode number from the linear to the non-linear phase has a transition from intermediate ($n \approx 10$) to low values ($n \approx 1$). This structural transition emphasizes the need to approach the question of ELM-sizes non-linearly. Furthermore the question is raised, whether the interaction of this modified non-linear perturbation and the conducting wall leads to a temporary saturation of the perturbation.
Dominant magnetic perturbations are compared with ELM signatures typically observed earlier (coherent ELM precursors) or later (ELM filaments) in order to obtain information and understanding of the ELM evolution. The transport during ELMs is characterized by a competition between parallel transport to the divertor and transport in radially ejected ELM filaments. The analysis method *diagnostic mapping*, which has been developed in the course of this thesis, allows to carry out an improved correlation of dominant magnetic perturbations and ELM filaments. The resulting observation of propagation of both features in different perpendicular directions is understood as a consequence of the strong perpendicu-

lar rotation shear in this radial region. Furthermore dominant magnetic perturbations have characteristics of a trigger for the radial propagation of ELM filaments.

The results gathered in the framework of this thesis enable the development of a picture of the processes during ELMs, which is more complete than any before. It is expected that this will contribute to a further extended understanding of ELMs and methods to mitigate them and to an ELM model, which is capable of reliably predicting ELM sizes and evolution.

Contents

Chapter 1

Introduction

It is projected that the global energy demands will have a rise of 40% between 2009 and 2035 [1]. Furthermore it is *very likely* that greenhouse gases (e.g. CO_2), which are a substantial byproduct in the combustion of fossil fuels, have a climate-changing effect [2]. By the end of the century there may be the need for a technology producing a significant amount of energy in an environmentally friendly and economical way. Nuclear fusion has the potential to be developed as a source of energy fullfilling these criteria. It is associated with negligible production of greenhouse gases and radioactive waste with long half-life.
The fusion reaction of two nuclei with lower masses than iron is exothermic. However to initiate a fusion process the Coulomb barrier between the nuclei involved has to be overcome or tunneled through.[1] If the distance between nuclei is low enough the attracting nuclear force, which is a residual effect of the more powerful strong interaction between quarks, becomes dominant. A candidate fusion reaction must be exothermic, involve only two reactants[2], involve reactants of low atomic number[3], have two or more products[4] and conserve both protons and neutrons[5]. These criteria are met by following reactions:

$$\mathrm{D}_1^2 + \mathrm{D}_1^2 \longrightarrow \mathrm{He}_2^3\ (0.817\mathrm{MeV}) + n_0^1\ (2.45\mathrm{MeV}) \qquad (\approx 50\%) \qquad (1.1)$$

$$\mathrm{D}_1^2 + \mathrm{D}_1^2 \longrightarrow \mathrm{T}_1^3\ (1.01\mathrm{MeV}) + \mathrm{H}_1^1\ (3.02\mathrm{MeV}) \qquad (\approx 50\%) \qquad (1.2)$$

$$\mathrm{D}_1^2 + \mathrm{T}_1^3 \longrightarrow \mathrm{He}_2^4\ (3.50\mathrm{MeV}) + n_0^1\ (14.1\mathrm{MeV}) \qquad (1.3)$$

$$\mathrm{D}_1^2 + \mathrm{He}_2^3 \longrightarrow \mathrm{He}_2^4\ (3.67\mathrm{MeV}) + \mathrm{H}_1^1\ (14.7\mathrm{MeV}) \qquad (1.4)$$

For a reaction with two reactants the volume rate (i.e. number of reactions per volume) can be expressed as $n_1 n_2 \langle \sigma v \rangle$, where n_i are the particle densities of the two reactants, σ is the cross section, v is the relative velocity and the brackets indicate averaging over the velocity distribution. Among the reactions above, the D-T reaction (equation 1.3) has the highest values of the reaction parameter $\langle \sigma v \rangle$ for Maxwellian distributions with temperatures between 1keV and 1MeV as illustrated in figure 1.1. Due to this one of the most promising solutions is to heat a D-T mixture to sufficient temperatures (thermonuclear fusion). In the relevant temperature range this mixture is in the state of a plasma.

[1] For the D-T reaction the Coulomb barrier is 415keV. Due to the tunnel effect already at particle energies of 10-20keV significant fusion rates are observed.

[2] For terrestrial fusion the cross sections of three body collisions are too low.

[3] The Coulomb repulsion is proportional to the product of the atomic numbers of the two nuclei.

[4] This allows simultaneous conservation of energy and momentum by the involved particles and avoids electromagnetic radiation.

[5] The cross sections for the weak interaction (β^+ decay) are too small.

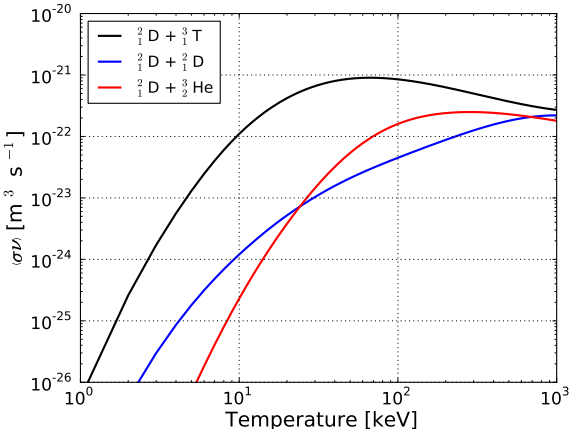

Figure 1.1: Reaction parameter $\langle\sigma v\rangle$ for three nuclear reactions averaged over Maxwellian distributions [3].

In a D-T plasma of sufficient temperature fusion born α-particles provide an additional heating channel. When this α-heating power reaches a level that it can fully replace the external heating power *ignition* is reached. A criterion for ignition is given by the triple product[6]

$$nT\tau_E > 3 \times 10^{21}\mathrm{m}^{-3}\mathrm{keVs}, \tag{1.5}$$

where τ_E is the energy confinement time (energy content divided by loss power) and T is the temperature [4]. Since the 1950s the achieved triple product has increased by seven orders of magnitude up to about $1 \times 10^{21}\mathrm{m}^{-3}\mathrm{keVs}$. Already below ignition conditions, when the fusion power P_F is equal to the heating power P_H, *break even* ($Q = P_F/P_H = 1$) is reached. The international nuclear fusion research and engineering project ITER has the objectives to reach $Q = 10$ in pulsed operation ($\tau_{\mathrm{pulse}} = 400\mathrm{s}$) and $Q = 5$ in steady state [5].

1.1 Magnetic confinement

The plasma temperatures necessary for D-T fusion reactions are a number of orders of magnitudes above the highest melting points. Hence one of the key challenges of thermonuclear fusion is to maintain high temperature gradients between the plasma and the vessel containing it. This can be reached by application of magnetic fields. As all particles of a fusion plasma up to a negligible minority are charged, they have helical trajectories around magnetic field lines (Lorentz force).[7] Hence apart from this gyration their main motion is parallel to the magnetic field. To improve particle and energy confinement of a magnetic confinement device in a first step the parallel[8] losses need to be restricted. This can be accomplished by toroidal geometry (i.e. field lines without ends).
The motion of the gyration center perpendicular to the magnetic field is highly restricted

[6]This inequality is valid for flat radial profiles of density and temperature. For parabolic radial profiles the threshold increases to $5 \times 10^{21}\mathrm{m}^{-3}\mathrm{keVs}$. Accounting for impurities like α-particles raises the value again to $\approx 1 \times 10^{22}\mathrm{m}^{-3}\mathrm{keVs}$.

[7]The radius of the circular motion around the magnetic field line is called the *Lamor radius*. For 2T and 1keV it is about 50μm for electrons and 3mm for deuterium ions.

[8]The terms *parallel* and *perpendicular* used without reference always refer to the local magnetic field direction.

compared to the parallel motion. It is the basis of magnetic confinement fusion, that this is the case especially for the velocity component down the pressure gradient, which is referred to as *radial component*. There can be an additional perpendicular drift motion with constant velocity, if a particle gyrating around a magnetic field is subject to an additional force. Important for this work are

- the drift due to an electric field ($\boldsymbol{E} \times \boldsymbol{B}$-drift):
  $\boldsymbol{v} = (\boldsymbol{E} \times \boldsymbol{B})/B^2$ (radial component possible),
- the drift due to a pressure gradient (diamagnetic drift):[9]
  $\boldsymbol{v} = (\nabla p \times \boldsymbol{B})/(qnB^2)$ (radial component not possible) and
- the drift due to a gradient of the magnetic field (∇B-drift):
  $\boldsymbol{v} = -mv_\perp^2/(2qB^3)\nabla B \times \boldsymbol{B}$ (radial component possible).

Other net radial perpendicular transport of particles can be caused by other drifts or collisions or turbulence (section 1.3).
In addition to particle and energy confinement sufficient power needs to be deposited in the plasma. For magnetic confinement devices a number of techniques have been developed. Accelerated and neutralized hydrogen particles (ASDEX Upgrade 50-100keV) are launched into the plasma. This heating schema called *neutral beam injection* is at the same time a fueling method in existing devices. Other heating schemes transfer energy from electromagnetic waves to the plasma particles. This is usually achieved by launching at a frequency, where the plasma has a resonance. Examples are *ion cyclotron resonance heating*, *electron cyclotron resonance heating* or *lower hybrid heating*.[10]
The quantity β is a description of the quality of magnetic plasma confinement. It balances the confined thermal energy and the magnetic energy necessary to achieve that. β and the *poloidal* β respectively are defined as

$$\beta = \frac{\int p dV / \int dV}{B_0^2/2\mu_0} \tag{1.6}$$

$$\beta_p = \frac{\int p dS / \int dS}{B_a^2/2\mu_0} \text{ with } B_a = \frac{\mu_0 I_p}{l}, \tag{1.7}$$

where the integrals are over the plasma volume and a poloidal cross-section respectively, B_0 is the toroidal magnetic field on the axis, I_p is the plasma current and l is the length of the poloidal perimeter. β_p has a special relevance in the context of plasma instabilities.

1.2 The Tokamak configuration

A configuration with a pure toroidal field is not stable, as the the ∇B-drift would lead to an up-down charge separation and consequently the $\boldsymbol{E} \times \boldsymbol{B}$-drift would result in an outward transport. Hence a poloidal component of the magnetic field is necessary.
The toroidal magnetic field in any magnetic fusion device of toroidal geometry is created by magnetic coils (figure 1.2). In a *tokamak* the poloidal magnetic field is caused by a toroidal

[9] The diamagnetic drift is not a drift of the center of the gyration of the particles. However the net velocity of the fluid is given by $(\nabla p \times \boldsymbol{B})/(qnB^2)$.

[10] Ion cyclotron resonance heating and electron cyclotron resonance heating launch at the fundamental or harmonics of the ion or electron Lamor frequency. In contrast to this lower hybrid heating is based on Landau damping.

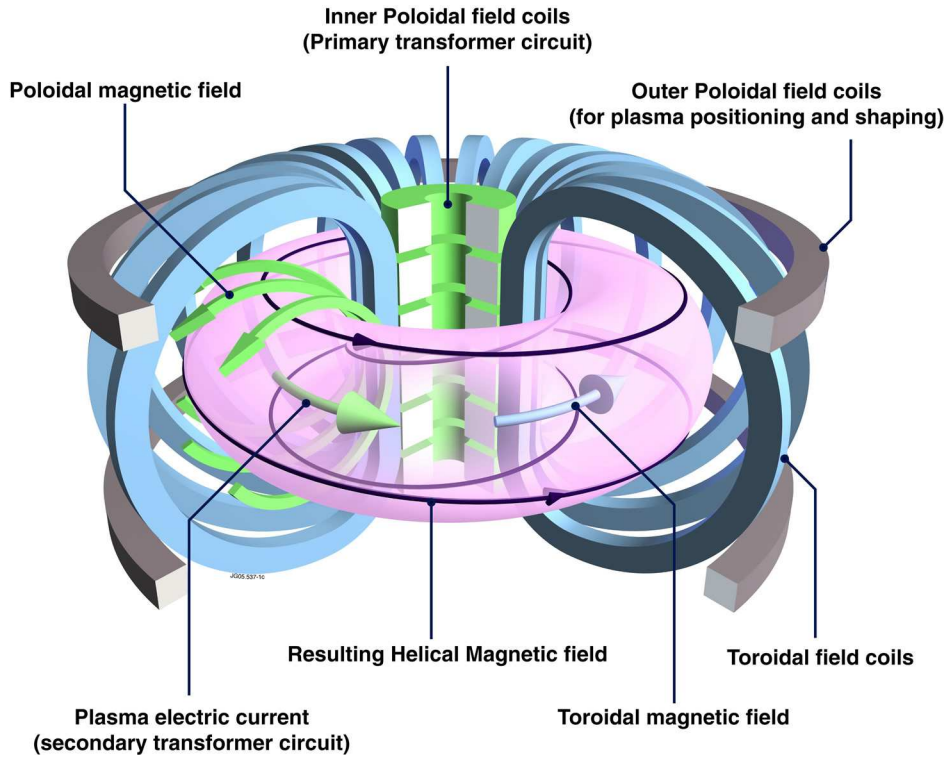

Figure 1.2: Schematic view of the components of the magnetic field and their origin. Note that in ASDEX Upgrade the resulting helical magnetic field has opposite inclination (helicity).

current. This current can be created by a transformer with primary coil in the center of the torus and the plasma acting as secondary winding (figure 1.2). In this operational mode the tokamak is not suited for steady state operation. It is questionable if a sufficient poloidal magnetic field can economically be produced by other current drive options, which are compatible with steady state operation [6]. From an engineer's point of view the tokamak is the simplest magnetic confinement design to produce substantial amounts of fusion power.

For tokamak plasmas in equilibrium, which are symmetric in the toroidal angle ϕ, the magnetic field lines approximately lie on nested surfaces (figure 1.3) called *flux surfaces*. Furthermore the current lines lie also on these surfaces and there is constant pressure on these surfaces.[11] In the center of the plasma, where the poloidal magnetic field vanishes there is a magnetic field line with toroidal direction only called *magnetic axis* (figure 1.3). Around the magnetic axis field lines either close on themselves (*rational*) or cover an entire flux surface. The *last closed flux surface (LCFS)* is the outermost flux surface with no field lines connecting to solid components of the experiment. The distance between the magnetic axis and a flux surface is referred to as *minor radius* r. The minor radius of the LCFS is denoted as *minor plasma radius* a.
The choice of an appropriate coordinate system is a key to the solution of many physical problems. In the context of tokamaks cylinder coordinates (R, Z, ϕ) as illustrated in figure 1.3 are an appropriate system to start. It is beneficial to maintain the coordinate ϕ for

[11] These properties follow form the assumption that there are contours of constant pressure in combination with the MHD momentum equation 2.4.

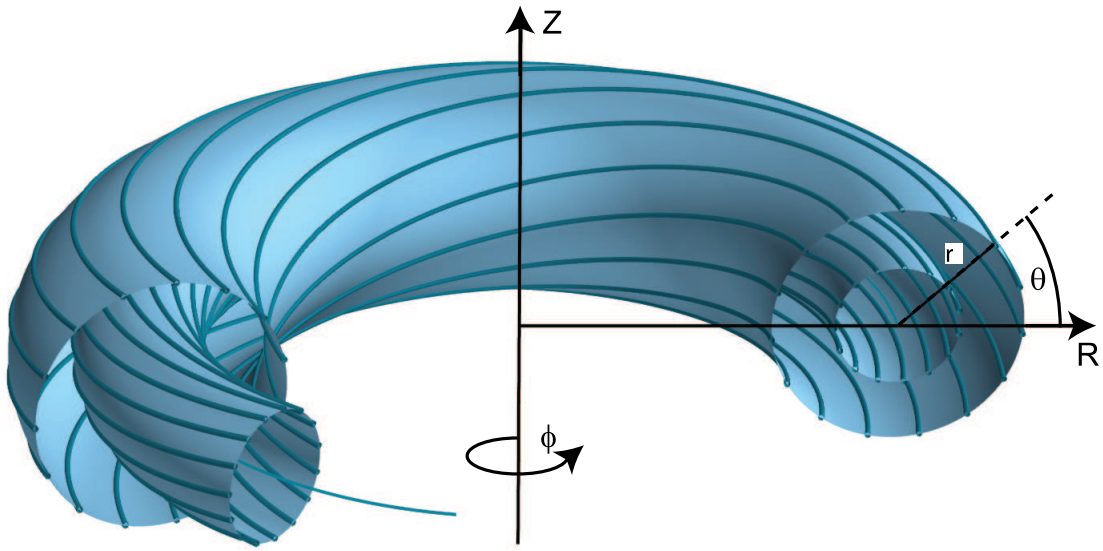

Figure 1.3: Schematic view of the field lines on two flux surfaces with circular cross sections and magnetic axis. The safety factor on the inner (outer) flux surface is 1 (2).

reasons of symmetry. The *poloidal magnetic* flux $\psi(R, Z)$ can be defined[12] as the vertical magnetic field integrated over the area of a horizontal circle through (R, Z) with center $(0, Z)$ divided by 2π

$$\psi(R, Z) = \int_0^R B_Z(R', Z) R' dR'. \tag{1.8}$$

ψ is constant on flux surfaces due to $\nabla \cdot \boldsymbol{B} = 0$. The normalized poloidal flux is defined as

$$\psi_N = \frac{\psi - \psi_{\text{axis}}}{\psi_{\text{LCFS}} - \psi_{\text{axis}}}, \tag{1.9}$$

where ψ_{axis} (ψ_{LCFS}) are the poloidal flux on the magnetic axis (LCFS). ψ_N is a convenient coordinate for the 'magnetic distance' of a flux surface to the magnetic axis, as it assigns the values 0 and 1 to the magnetic axis and the LCFS. The derived quantity $\rho_{\text{pol}} = \sqrt{\psi_N}$ has the advantage of being close to linear in r at the outboard mid plane.
For the parametrization of a position on a certain flux surface at a certain toroidal angle the poloidal angle θ as illustrated in figure 1.3 is frequently used.
The field line inclination can either be described locally by $d\theta/d\phi$ or globally by the *safety factor* q, which is defined as the number of toroidal turns of a field line for a full poloidal turn. For example for a rational field line, which is passing each toroidal (poloidal) position n (m) times it is $q = m/n$. The radial variation of the field line inclination, which is relevant in view of instabilities, can also be expressed globally or locally. Globally in the large aspect

[12]Back transformation: $B_R = \frac{1}{R}\frac{\partial \psi}{\partial R}, B_Z = -\frac{1}{R}\frac{\partial \psi}{\partial Z}$

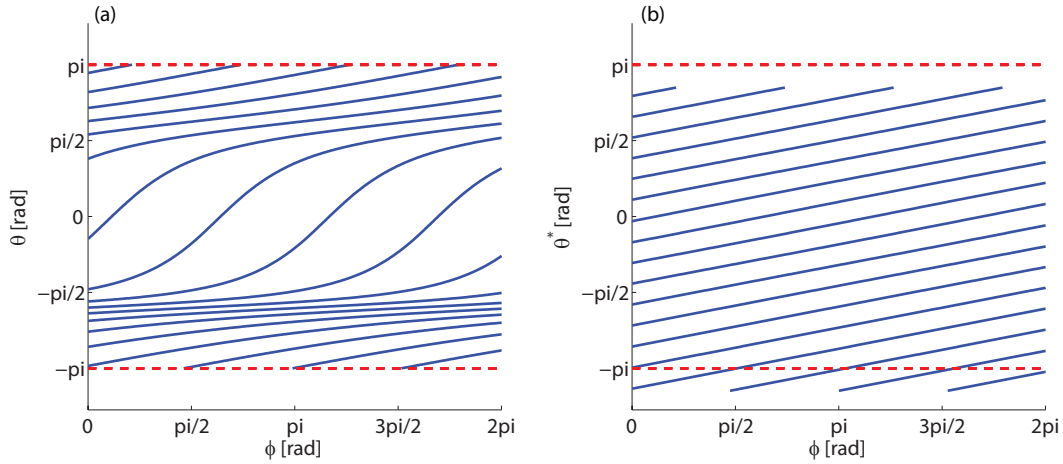

Figure 1.4: Magnetic field lines on a flux surface: (a) Poloidal angle θ and (b) straight field line angle θ^* as function of the toroidal angle ϕ.

ratio circular cross section approximation the *magnetic shear* is defined as

$$s = \frac{r}{q}\frac{dq}{dr}. \tag{1.10}$$

Figure 1.4(a) shows that in coordinates ϕ and θ the magnetic field lines in a tokamak are not straight. For the analytic description of perturbation structures it is sometimes helpful to have a parametrization of the poloidal coordinate, in which field lines do appear as straight lines. An alternative poloidal parametrization with this property is given by the *straight field line angle* θ^* (figure 1.4(b)). For the points on a field line passing through $(\phi, \theta) = (0, 0)$ this is defined by[13]

$$\theta^* = \frac{\phi}{q}. \tag{1.11}$$

An alternative but equivalent definition of θ^* is given in [7].
Non-circular plasma cross sections lead to interesting properties of tokamak plasmas like advanced performance [8]. This is connected to the fact that the shape of the plasma cross section has an influence on stability (subsection 2.2.2). To describe the shape of non-circular plasma cross sections in low order the quantities *elongation* κ and *triangularity* δ as defined in figure 1.5 are introduced.
There are several possible configurations for the LCFS in a tokamak. Two of them are displayed in figure 1.6. In the limiter configuration the main plasma is in direct contact with the solid state limiter. In contrast in a configuration with an X-point it is possible to move the solid state contact further away from the main plasma to the divertor. Due to this, plasmas in diverted configurations are generally cleaner than limited configurations. The X-point has zero poloidal field, which is usually achieved by additional poloidal field coils.

1.3 H-Mode

In several magnetic confinement devices operational conditions have been found, where the energy and particle confinement time is significantly increased with respect to standard op-

[13] In the JOREK calculations $\theta^* = 0$ on the connection line between magnetic axis and X-point.

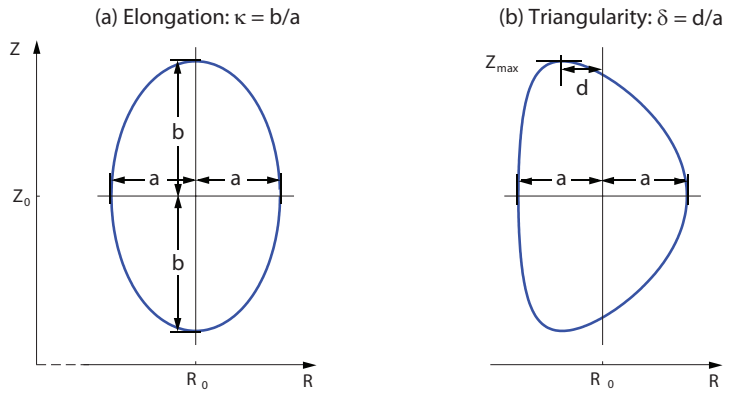

Figure 1.5: Definition of (a) elongation κ and (b) triangularity δ for a minor plasma radius a. Figure adapted from [9].

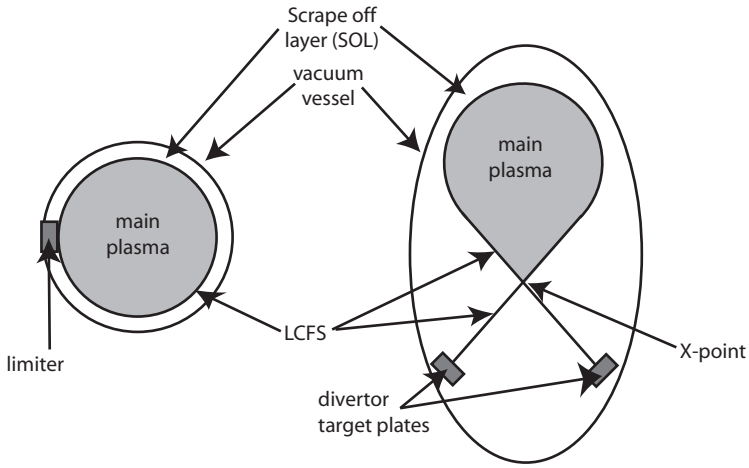

Figure 1.6: Schematic view of LCFS configurations: Limiter configuration (left) and configuration with X-point and divertor (right).

eration. Among these devices are all tokamaks with divertor plus auxiliary heating [10, 11] as well as limited tokamaks [12] and stellarators [13]. The H-mode was first observed in the ASDEX tokamak [10], where it was found to have an energy confinement time higher by a factor of 2 when compared to the low confinement regime (*L-mode*). In [10] the only difference in the externally controlled parameters is a higher ($\approx 20\%$) neutral beam injection power in the H-mode case compared to the L-mode case.
To first order the heat flux density $\boldsymbol{q}$ and particle flux density $\boldsymbol{\Gamma}$ can be described by $\boldsymbol{q} = -Kn\nabla T$ and $\boldsymbol{\Gamma} = -D\nabla n$, where K and D are the heat and particle diffusivity (transport coefficients). Figure 1.7 shows profiles of electron temperature T_e, density n_e and pressure p_e in discharge AUG17741 [14]. The main changes of the gradients of these quantities introduced by the L-H transition can be observed in a narrow layer at the edge of the plasma ($0.95 < \rho_{\mathrm{pol}} \leq 1$). In this area, which is called *pedestal*, the gradients of both T_e and n_e are significantly increased. Further inside the gradients are only slightly increased or decreased. Hence during the L-H transition the transport coefficients mainly change in the pedestal.

Fully understanding the physics of the L-H transition would first require the ability to

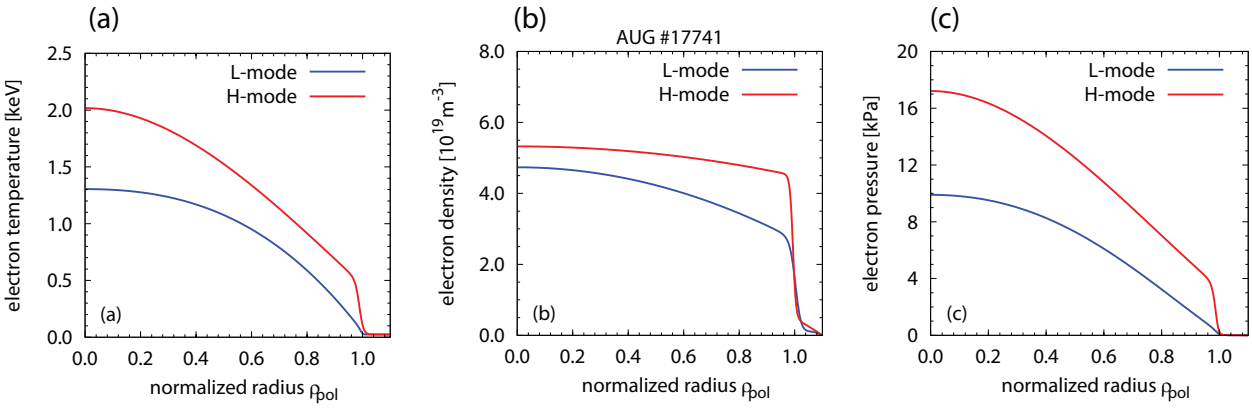

Figure 1.7: Profiles of (a) electron temperature, (b) electron density and (c) electron pressure in discharge AUG17741. L-mode (blue, $t = 1.6$s) and H-mode (red, $t = 2.1$s). The figure has been adapted from [14].

reproduce experimental L-mode transport coefficients in numerical simulations. Classical transport predictions (i.e. transport due to collisions) and also neo-classical transport predictions (i.e. transport due to collisions regarding radial excursion of trapped particles[14] on banana-orbits) clearly underestimate the experimentally measured values of the transport coefficients. Turbulence is a candidate phenomenon to explain the high transport coefficients in experiments.
A mechanism, which is discussed to explain L-H transition, is turbulence suppression by perpendicular flow shear (i.e. differential perpendicular rotation) [15, 16]. It has been observed experimentally that after the L-H transition edge density fluctuations are abruptly suppressed [17]. Furthermore a strong flow shear has been reported from a number of experiments [18, 19, 20, 21].

Modification of the density and temperature profiles can also lead to changes in the toroidal edge current density. The relevant current component called *bootstrap current* is due to a neo-classical effect. In the presence of density or temperature gradients trapped particles have an asymmetry in the parallel velocity distribution. Due to collisions there is a transfer of momentum to passing electrons and ions leading to a net current - the bootstrap current. It has been known for several decades that the bootstrap current scales with density and temperature gradients [22]. Calculations solving the Fokker-Planck equation[15] with the full collisional operator allowed the accurate determination of the bootstrap current [23, 24]. They have shown that a density gradient as well as a gradient in electron or ion temperature drives bootstrap current. It is

$$\langle j_{bs} B \rangle \propto \; c_0 \left[c_1 \frac{\partial \ln n_e}{\partial \psi} + c_2 \frac{\partial \ln T_e}{\partial \psi} + c_3 \frac{\partial \ln T_i}{\partial \psi} \right], \tag{1.12}$$

[14] If the absolute value of the magnetic field increases along a field line, energy is transfered from the parallel to the perpendicular motion (gyration). In a tokamak this leads to a reflection in the parallel direction for particles with relatively high perpendicular velocity (*trapped particles*). Particles with relatively lower perpendicular velocity are not reflected (*passing particles*).

[15] The Fokker-Planck equation is equivalent to the kinetic equation (section 2.2) with a Coulomb collision operator accounting for energy scattering and pitch angle scattering.

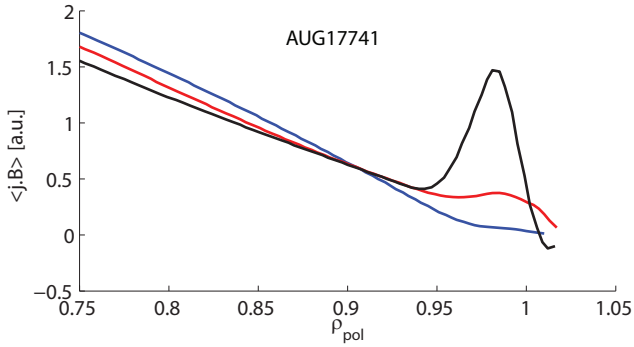

Figure 1.8: Flux surface averaged $\boldsymbol{j} \cdot \boldsymbol{B}$ from a CLISTE reconstruction using magnetic data and pressure profiles for discharge AUG17741. The time windows correspond to the ones in figure 1.7 (red and blue) and 3.0 to 3.5s (black).

where $\langle\rangle$ is a flux surface average, c_0 is a constant with identical sign as I_p and $c_1, c_2 > 0$ and c_3 such that the bracket is positive. These findings have been confirmed for conditions similar to H-mode by guiding center simulations including a Monte Carlo model of pitch-angle scattering [25]. Furthermore it has been found that similar values can be obtained from equilibrium reconstruction constrained by kinetic profiles and scrape off layer (SOL) currents ($I_{\mathrm{pol,sol,out}} \rightarrow$ section 4.1) [26].
Figure 1.8 shows a comparison of the flux surface averaged product $\langle \boldsymbol{j} \cdot \boldsymbol{B} \rangle$ for three time windows in discharge AUG17741. As $\boldsymbol{B}$ is nearly constant the main differences are due to differences in the toroidal current density. In comparison to the L-mode case (blue) in the early H-mode phase (red) an additional peak at the plasma edge is observed. In the later H-mode phase (black) this peak has considerably increased. Closer analysis shows that this peak is associated with bootstrap current.
The bootstrap current is regarded to play an important part in the context of H-mode edge instabilities and especially edge localized modes.

1.4 Motivation and objectives of this thesis

The H-mode regime in tokamaks is frequently associated with instabilities at the plasma edge called *edge localized modes* (ELMs) (chapter 2). ELMs are events of bursty nature appearing with frequencies between some Hz and some hundreds of Hz. They enhance momentarily energy and particle transport and thus allow the maintenance of stationary H-mode. On the other hand in a future device ELMs may cause energy deposition far in excess of tolerable material limits [27]. Hence the energy deposition during ELMs has to be controlled.
Schemes for H-mode operation without ELMs or with ELMs releasing low amounts of energy have been proposed (e.g. type III ELMs, quiescent H-mode, quiescent H-mode with balanced neutral beam injection [28, 29, 30]) . However it is not clear, if in a reactor size device stationary operation with high confinement and no or small ELMs can be achieved. A large amount of research is dedicated to the development of ELM mitigation techniques. Among these are ELM control by pellet injection [31, 32] and ELM control by resonant magnetic perturbations [33].
Extensive effort has been dedicated towards understanding the physics of ELMs. On the

theoretical side the majority of investigations are directed at the linear physics of edge instabilities in tokamaks. However it is recognized that quantitative predictions of the ELM size require non-linear studies (section 2.2.3). More recently non-linear codes to simulate ELMs like JOREK [34] have been constructed and are under further development.
In parallel to these theoretical studies a large number of experimental investigations of ELMs have been performed, some of which correlated measurements from several diagnostics. Besides an extensive number of open questions there is also scope for improvement with respect to the problems arising from the 3D geometry of the perturbation in combination with the fact that the relevant diagnostics generally are in a variety of locations. Any improvement in this direction could particularly enable an improved reconstruction of the magnetic perturbation structure. Furthermore the capabilities of diagnostics are continuously evolving and new diagnostics are becoming available, which is especially the case at ASDEX Upgrade.
The combination of these new experimental possibilities and ideas and theoretical tools motivates this thesis, which should address the following questions:

- Is it possible to reconstruct the ELM evolution until the early non-linear phase?
- How is the evolution of the magnetic perturbation structure until the early non-linear ELM phase characterized?
- What is typically the dominant toroidal mode number of the non-linear magnetic perturbation?
- Has the ELM evolution already arrived at the non-linear phase when the observed magnetic perturbations exceed the background fluctuation level?
- Are there significant differences between the linear and the non-linear magnetic perturbation structure?
- Is it possible to correlate perturbations of the magnetic field and other key parameters?
- How are magnetic perturbations and filaments observed in the scrape off layer linked to each other?
- How is the pedestal erosion correlated to the evolution of magnetic perturbations?

In chapter 2 key experimental observations related to ELMs and the current understanding of this instability in the framework of magnetohydrodynamics are reviewed. The chapter ends with a section on the non-linear, reduced MHD code JOREK, which has been employed in this thesis for an ELM simulation. Chapter 3 describes the synthetic diagnostic module (SYNMAG) for JOREK, which has been developed in the course of the work presented. SYNMAG evaluates the evolution of signals in virtual magnetic probes and hence enables an improved comparison between simulation and experiment. Arrangements and tools related to the experimental investigations are introduced in chapter 4. Here information on diagnostics that are employed and details of the analyzed discharges are provided. Furthermore the chapter provides information on central tools, which have been developed or adapted within the frame of the presented work, for the analysis of experimental data.
Chapter 5 describes the main results obtained in the experiments ASDEX Upgrade[16] [35] and TCV[17] [36]. Here the main focus is on the characterization of dominant magnetic

[16]Max-Planck-Institut für Plasmaphysik, Garching, Germany
[17]Centre de Recherches en Physique des Plasmas, École polytechnique fédérale de Lausanne, Lausanne, Switzerland

perturbations during ELMs. This already provides answers to a number of questions listed above. Furthermore the relation to signatures before and after these dominant magnetic perturbations is investigated. Related findings from a JOREK simulation are reported in detail in chapter 6. Chapter 7 summarizes the main results in experiments and simulation and discusses some key aspects of ELMs, which are addressed in the questions above.

Chapter 2

Edge Localized Modes

In recent decades ELMs have been the focus of several reviews with both experimental and theoretical orientation [28, 37, 38]. As an introduction a number of key experimental observations related to ELMs are recapitulated. After that the current understanding of this type of instability in the framework of magnetohydrodynamics (MHD) is described. In the last part of the chapter the code JOREK is described, which simulates ELMs non-linearly in a simplified MHD model.

2.1 Key experimental observations related to Edge Localized Modes

ELMs are a feature of the H-mode regime [10] of tokamak plasmas. They may be described as sudden losses of particles [39] and energy [28] from the pedestal region often described as *ELM crash*. ELMs are embedded in the *ELM cycle*. Figure 2.1 shows the evolution of several relevant quantities within this cycle. At the three times marked by vertical dashed lines ELM crashes can be identified. After these crashes all quantities recover on a slower time scale towards their pre ELM values. The duration between subsequent ELMs (inverse ELM frequency) is partly determined by the length of this recovery phase. In some cases after this phase the plasma seems to rest for a number of ms in a fully recovered state before the next ELM crash happens. A detailed description of the ELM cycle for an ASDEX Upgrade discharge can be found in [40].
Several types of ELMs are distinguished [28]. Type I ELMs, which are the main focus of this work, can be identified by a combination of

a) increasing ELM frequency with increasing energy flux through the LCFS P_{sep} [28] and[1]
b) relative losses $\Delta W_{\mathrm{mhd,ELM}}/W_{\mathrm{ped}}$ of at least a few percent of the thermal energy of the pedestal [41] .[2]

Temporally close to the onset of increased particle and energy flux in the divertor (and often before) magnetic perturbations can be registered. In an MHD picture these magnetic perturbations may be regarded as the footprint of the deformation of surfaces of constant

[1] $P_{\mathrm{sep}} = P_{\mathrm{tot}} - \frac{dW_{\mathrm{mhd}}}{dt} - P_{\mathrm{rad}}(\mathrm{core})$, where P_{tot} is the total heating power, W_{mhd} is the thermal plasma energy and $P_{\mathrm{rad}}(\mathrm{core})$ is the power radiated from the plasma core.
[2] $W_{\mathrm{ped}} = 3 n_{\mathrm{ped}} T_{\mathrm{ped}} V_{\mathrm{plasma}}$, where V_{plasma} is the total plasma volume and $T_{e,\mathrm{ped}} \approx T_{i,\mathrm{ped}}$ is assumed.

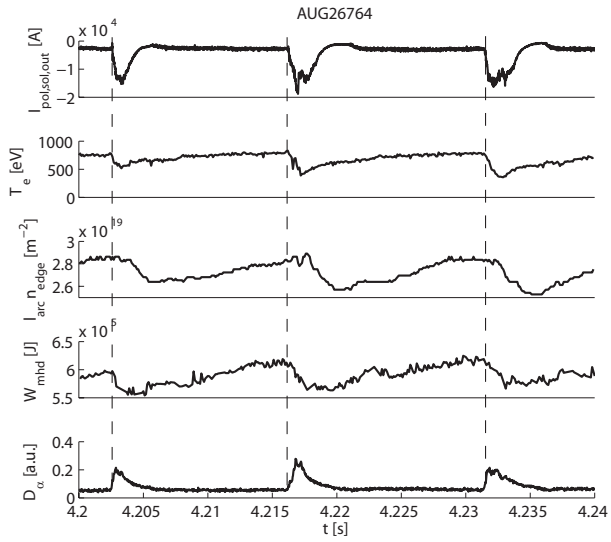

Figure 2.1: Evolution of several physical quantities within the ELM cycles in discharge AUG26764: Current to the outer divertor $I_{\mathrm{pol,sol,out}}$, electron temperature T_e at $\rho_{\mathrm{pol}} = 0.95$ from electron cyclotron emission spectroscopy, electron density n_{edge} integrated along the edge interferometer line of sight inside the confined plasma, thermal plasma energy W_{mhd} obtained from equilibrium reconstruction and intensity of the D_α radiation. Vertical dashed lines indicate ELM crashes.

poloidal magnetic flux. Therefore they may serve as a tool to investigate ELM phases even before the onset of increased particle and energy flux in the divertor.
At JET the associated ELM loss of pedestal thermal plasma energy has been found to be up to 20%, where W_{ped} is about $30 - 50\%$ of the full plasma energy [42]. Typical timescales for these losses are in the case of ASDEX Upgrade of the order of 1ms (figure 4.6). Usually the majority of the energy $\Delta W_{\mathrm{mhd,ELM}}$ lost during the ELM crash is accounted for by the energy E_{div} deposited on the divertor target plates plus the energy E_{rad}, which is radiated during this process. In [43] it has been reported that in ASDEX Upgrade $E_{\mathrm{div}} + E_{\mathrm{rad}}$ represent $75 - 95\%$ of $\Delta W_{\mathrm{mhd,ELM}}$. The missing part of $\Delta W_{\mathrm{mhd,ELM}}$ is assumed to be deposited on the remaining plasma facing components. In discharges with double null configuration (i.e. with X-points at the top and bottom of the device) in DIII-D it was found that virtually no energy is deposited on the inner divertor [44]. This suggests at least in the case of double null configurations that the ELM associated perturbations are predominantely on the outboard side of the plasma.
As ELMs are associated with both convective and conductive transport, besides increased energy flux to the divertor there is also an enhanced particle transport to the divertor. This has been observed via Langmuir probes [45, 46]. Under certain conditions related to the detachment state [47], when the D_α radiation in the divertor shows a strong increase correlated with the ELM. Furthermore in ASDEX Upgrade the ELM crash is correlated to an increase of the current $I_{\mathrm{pol,sol,out}}$ [40], which represents the sum of the currents through four shunts connected to outer divertor tiles with identical toroidal but different poloidal positions in the SOL. This rise is speculated to be due to a thermoelectric effect between the outer and the inner divertor target plates.
Type I ELMs are associated with field aligned plasma filaments propagating in the plasma

edge (pedestal region and SOL), which have been observed by several diagnostics. In these filaments density and temperature are perturbed by values comparable to the pre-ELM equilibrium quantities [48]. Footprints of these filaments on the divertor of ASDEX Upgrade have been observed by infrared thermography [49]. With fast framing cameras they have been directly observed in MAST [50]. The following simple model for ELM energy losses has been proposed by Kirk on the basis of observations at MAST [51]:
For the first $50-100\mu$s during which filaments can be observed by fast cameras, they remain near the LCFS. During this time their presence already leads to increased losses. After this time the filaments propagate radially away from the LCFS. It is suggested that in the course of this process a reconnection event occurs so that the filament is no longer attached to the plasma.[3] At the time of this reconnection $50-75\%$ of the total particle and energy loss has already occured.

From the engineering perspective ELMs may be associated by severe problems for future devices. The high amount of energy deposited in short time intervals on the plasma facing components are limiting the life times of the components due to material erosion. In particular the power flux density and the density of deposited energy arriving at the divertor target plates needs to be confined [27, 41, 52].

2.2 Plasma edge instabilities in the MHD picture

There are a range of descriptions of plasmas with a background magnetic field, each with different regimes of validity. The simplest self-consistent one is the theory of magnetohydrodynamics (MHD), which is derived for instance by Freidberg [53]. Following the systematics of this derivation a sequence of plasma descriptions with decreasing complexity and increasing sets of assumptions leading to the MHD model is listed:

- In a **many-body problem** each particle is described by one equation of motion linked to all others via interaction terms. For any realistic problem the number of equations to solve simultaneously is beyond what can be managed with state of the art technology.

- The **kinetic description** is a statistical approach, which describes the plasma by a distribution function. This description can be approached via the so-called Klimontovitch distribution function $f_\alpha^K(\boldsymbol{x},\boldsymbol{v},t)$ describing the density of particles of species α in the phase-space-volume $d^3\boldsymbol{x}d^3\boldsymbol{v}$ as a sum of delta functions centered at the position of each particle in phase space [54]. This description is equivalent to the many-body problem.
  As f_α^K is not smooth, averaging over a volume in phase space is carried out, which has an extension that is small compared to the system size and thermal velocity respectively. The resulting distribution function f_α describes the mesoscopic particle density distribution. It satisfies a continuity equation called *kinetic equation*:
  $$\frac{\partial f_\alpha}{\partial t}+\boldsymbol{v}\cdot\nabla f_\alpha+\frac{q_\alpha}{m_\alpha}(\boldsymbol{E}+\boldsymbol{u}\times\boldsymbol{B})\cdot\nabla_{\boldsymbol{v}} f_\alpha=\left(\frac{\partial f_\alpha}{\partial t}\right)_c, \tag{2.1}$$
  where the term on the right describes the effect of forces on the microscopic scale (i.e. collisions). The kinetic equation in combination with the Maxwell equations and two

[3] Before this detachment event filaments are equivalent to peaks of the perturbation of the flux surfaces with $k_\perp \gg k_\parallel$.

equations expressing current and charge density in terms of the distribution function represent a closed set of equations.

- The transition to the **two-fluid description** starts by taking appropriate moments of the kinetic equation giving mass, momentum and energy of each species. The main assumption made here is that the velocities follow a Maxwell distribution. Replacing the distribution function by these moments leads to a loss of information. The final set of two-fluid equations consists of three conservation laws (continuity equation, momentum equation and energy conservation) for each of the two species plus Maxwell equations. A generic problem associated with taking moments is that there are more unknowns than equations. Hence the two-fluid equations are not closed.

2.2.1 Magnetohydrodynamics

More assumptions are made in order to arrive at the single fluid description (MHD). Now, essentially the high-frequency, short-wavelength information is reduced from the model. In particular this means that the displacement current in Maxwell's version of Ampére's law is neglected and that quasineutrality is assumed. Furthermore the electron inertia is neglected. These assumptions introduce strong restrictions with respect to the range of phenomena that can be captured:

- Electromagnetic waves of interest should have phase velocities much smaller than the speed of light ($\omega/k \ll c$). As well the characteristic thermal velocities of both electrons and ions should be non-relativistic ($V_{T_e}, V_{T_i} \ll c,\ V_{T_\alpha} = (2T_\alpha/m_\alpha)^{1/2}$).
- The characteristic frequencies should be small compared to the electron plasma frequency ($\omega \ll \omega_{pe},\ \omega_{pe} = (n_0 e^2/m_e\epsilon_0)^{1/2}$) and the electron cyclotron frequency ($\omega \ll \omega_{ce},\ \omega_{ce} = eB/m_e$).
- The characteristic length scales should be large compared to the Debye length ($a \gg \lambda_d,\ \lambda_d = V_{T_e}/\omega_{pe}$) and to the electron gyro radius ($a \gg r_{Le},\ r_{Le} = V_{T_e}/\omega_{ce}$).
- The assumption of a Maxwell distribution made in the transition to the two-fluid description necessitates sufficient collisions. However in a typical fusion plasma the mean free path is of the order 1km, corresponding to an ion collision time of the order 1ms. Therefore MHD is not a good description of the dynamics parallel to the field lines. However phenomena with relatively large parallel wavelength may still be well described by MHD. The modes described in subsections 2.2.2.2 to 2.2.2.4 belong to this class.

There is also a class of low-frequency, long-wavelength plasma modes with times scales and length scales, which are not too different from MHD. These modes called *drift waves* can not be captured in the MHD description due to the neglecting of electron inertia.

On the basis of these assumptions it is possible to introduce a set of single fluid variables:

$$\begin{aligned} \text{Mass density } \rho &= m_i n \\ \text{Fluid velocity } \boldsymbol{v} &= \boldsymbol{v_i} \\ \text{Current density } \boldsymbol{j} &= en(\boldsymbol{v_i} - \boldsymbol{v_e}) \\ \text{Pressure } p &= nT = p_e + p_i \\ \text{Temperature } T &= T_e + T_i \end{aligned} \tag{2.2}$$

Finally this leads to the closed set of MHD equations

$$\text{Continuity equation:} \quad \frac{d\rho}{dt} + \rho\nabla\cdot\boldsymbol{v} = 0 \tag{2.3}$$

$$\text{Momentum equation:} \quad \rho\frac{d\boldsymbol{v}}{dt} = \boldsymbol{j}\times\boldsymbol{B} - \nabla p \tag{2.4}$$

$$\text{Ohm's law:} \quad \boldsymbol{E} + \boldsymbol{v}\times\boldsymbol{B} = 0 \quad \text{(ideal MHD)} \tag{2.5}$$

$$\boldsymbol{E} + \boldsymbol{v}\times\boldsymbol{B} = \eta_{\parallel}\boldsymbol{j} \quad \text{(resistive MHD)} \tag{2.6}$$

$$\text{Adiabatic equation of state:} \quad \frac{d}{dt}\left(\frac{p}{\rho^{\gamma}}\right) = 0 \tag{2.7}$$

$$\text{Maxwell equations:} \quad \nabla\times\boldsymbol{E} = -\frac{\partial\boldsymbol{B}}{\partial t} \tag{2.8}$$

$$\nabla\times\boldsymbol{B} = \mu_0\boldsymbol{j} \tag{2.9}$$

$$\nabla\cdot\boldsymbol{B} = 0, \tag{2.10}$$

where $\eta_{\parallel}$ is the parallel resistivity, $\gamma = 5/3$ is the adiabatic index and μ_0 is the vacuum permeability. In the MHD regime the two-fluid energy equation containing higher moments reduces to the adiabatic equation of state 2.7. Therefore the MHD equations are a closed set of 14 scalar variables and 14 scalar equations.[4]

2.2.2 Linear instability theory

The reduction of a given MHD problem to the linearized problem by removing non-linear aspects is a method, which is often applied. The linearized problem usually has a simpler form and sometimes can be even solved analytically. On the other side removing the non-linear terms usually reduces the validity of the model often to the early growth phase only, when the perturbations are small compared to equilibrium quantities.

2.2.2.1 The energy principle

An efficient tool to study stability properties of a linearized MHD system is the energy principle. In the following the main steps of its derivation are outlined. The fully detailed derivation of the energy principle can be found in [53].
Each quantity is expressed as sum of an equilibrium quantity and a perturbed quantity: $Q(\boldsymbol{r},t) = Q_0(\boldsymbol{r}) + \tilde{Q}_1(\boldsymbol{r},t)$ with $\tilde{Q}_1 \ll Q_0$. Furthermore a displacement vector $\boldsymbol{\xi}$ is introduced. This is a quantity of first order in $\tilde{Q}_1/Q_0$ defined by

$$\tilde{\boldsymbol{v}}_1 = \frac{d\boldsymbol{\xi}}{dt}. \tag{2.11}$$

It represents the displacement of the plasma from the equilibrium position. $\boldsymbol{\xi}$ is further used to express all other perturbed quantities. An appropriate set of initial conditions is:

$$\begin{aligned}\boldsymbol{\xi}(\boldsymbol{r},0) = \tilde{\boldsymbol{B}}_1(\boldsymbol{r},0) = \tilde{\rho}_1(\boldsymbol{r},0) = \tilde{p}_1(\boldsymbol{r},0) = 0,\\ \frac{\partial\boldsymbol{\xi}(\boldsymbol{r},0)}{\partial t} = \tilde{\boldsymbol{v}}_1(\boldsymbol{r},0) \neq 0.\end{aligned} \tag{2.12}$$

[4] In this context equation 2.10 may not be counted. Equation 2.8 implies $\partial(\nabla\cdot\boldsymbol{B})/\partial t = 0$. Hence if $\nabla\cdot\boldsymbol{B} = 0$ is valid as a starting condition it will keep validity for all times.

Now continuity equation (2.3), adiabatic equation of state (2.7) and Faraday's Law (2.8) can be expressed in a linearized way (i.e. removing all terms of second and higher order in $\tilde{Q}_1/Q_0$ or $\boldsymbol{\xi}$):

$$\begin{aligned} \tilde{\rho}_1 &= -\nabla \cdot (\rho_0 \boldsymbol{\xi}), \\ \tilde{p}_1 &= -\boldsymbol{\xi} \cdot \nabla p_0 - \gamma p_0 \nabla \cdot \boldsymbol{\xi}, \\ \tilde{\boldsymbol{B}}_1 &= \nabla \times (\xi \times \boldsymbol{B}_0). \end{aligned} \tag{2.13}$$

These quantities can be inserted to the momentum equation giving one single equation for the displacement vector:[5]

$$\begin{aligned} &\rho \frac{\partial^2 \boldsymbol{\xi}}{\partial t^2} = \boldsymbol{F}(\boldsymbol{\xi}), \text{ with} \\ &\boldsymbol{F}(\boldsymbol{\xi}) = \frac{1}{\mu_0}(\nabla \times \boldsymbol{B}_0) \times \tilde{\boldsymbol{B}}_1 + \frac{1}{\mu_0}(\nabla \times \tilde{\boldsymbol{B}}_1) \times \boldsymbol{B}_0 + \nabla(\boldsymbol{\xi} \cdot \nabla p_0 + \gamma p_0 \nabla \cdot \boldsymbol{\xi}). \end{aligned} \tag{2.14}$$

The force operator $\boldsymbol{F}(\boldsymbol{\xi})$ describes the force on a volume element.
As none of the equilibrium quantities has a time dependence, it is possible to Fourier transform the perturbed quantities $\tilde{Q}_1(\boldsymbol{r}, t) = \sum_\omega Q_1(\boldsymbol{r}) e^{-i\omega t}$ and to treat each frequency component $Q_1(\boldsymbol{r}) e^{-i\omega t}$ separately. This transforms the force equation (2.14) into an eigenvalue problem:

$$-\omega^2 \rho \boldsymbol{\xi} = \boldsymbol{F}(\boldsymbol{\xi}). \tag{2.15}$$

It is possible to show that the force operator $\boldsymbol{F}$ is self-adjoint.[6] Therefore the eigenvalues ω^2 are real. Two possible situations can be distinguished:

- **Stability**: If $\omega^2 > 0$, ω is real and the system is oscillating.
- **Instability**: If $\omega^2 < 0$, ω is imaginary and an exponentially growing solution exists.

In principle this allows the calculation of growth rates and eigenfunctions. However in practice this task turns out to be extremely challenging. The self-adjointness of $\boldsymbol{F}$ allows as an alternative a *variational formulation*, which is obtained by multiplying equation 2.15 by $\boldsymbol{\xi}^*$ and integrating over the entire volume:

$$\begin{aligned} \omega^2 &= \frac{\delta W(\boldsymbol{\xi}^*, \boldsymbol{\xi})}{K(\boldsymbol{\xi}^*, \boldsymbol{\xi})}, \text{where} \\ \delta W(\boldsymbol{\xi}^*, \boldsymbol{\xi}) &= -\frac{1}{2} \int \boldsymbol{\xi}^* \cdot \boldsymbol{F}(\boldsymbol{\xi}), \\ K(\boldsymbol{\xi}^*, \boldsymbol{\xi}) &= \int \rho_0 |\xi|^2 dV. \end{aligned} \tag{2.16}$$

In [53] it is shown that any allowable function $\boldsymbol{\xi}$ for which ω^2 becomes an extremum is an eigenfunction with eigenvalue ω^2. On the basis of this the *energy principle* can be derived. It states that a situation is stable if and only if $\delta W(\boldsymbol{\xi}^*, \boldsymbol{\xi}) \geq 0$ for all allowable displacement functions. Inversely this implies that the system is unstable, if there is one displacement

[5] Here for simplicity $\tilde{\boldsymbol{B}}_1$ is not yet replaced by $\nabla \times (\xi \times \boldsymbol{B}_0)$.
[6] $\boldsymbol{F}$ is self-adjoint means: If $\boldsymbol{\xi}$ and $\boldsymbol{\eta}$ are arbitrary displacements it is $\int \boldsymbol{\eta} \boldsymbol{F}(\boldsymbol{\xi}) d\boldsymbol{r} = \int \boldsymbol{\xi} \boldsymbol{F}(\boldsymbol{\eta}) d\boldsymbol{r}$.

function with a negative $\delta W(\boldsymbol{\xi}^*, \boldsymbol{\xi})$.
Now it is beneficial to transform δW into a more intuitive form. This is done by separating the integration area into a fluid (plasma), a surface, and a vacuum part.

$$\delta W = \delta W_F + \delta W_S + \delta W_V, \text{with} \tag{2.17}$$

The three contributions can be written as follows:

$$\delta W_V = \frac{1}{2} \int_{\text{vacuum}} \frac{B_1^2}{2\mu_0} dV \tag{2.18}$$

The vacuum contribution δW_V only consists of magnetic energy and is always positive (i.e. stabilizing).

$$\delta W_S = \int_{\text{surface}} (\boldsymbol{n} \cdot \boldsymbol{\xi}_\perp)^2 \boldsymbol{n} \cdot \left[\!\left[\nabla \left(p_0 + \frac{B_0^2}{2\mu_0} \right) \right]\!\right] dS \tag{2.19}$$

Here $\boldsymbol{n}$ is the surface normal and $[\![\ ]\!]$ represents the jump of a quantity at the surface. The index $\perp$ refers here to the equilibrium magnetic field. The surface contribution δW_S vanishes unless surface currents flow on the plasma-vacuum boundary.

$$\begin{aligned} \delta W_F = \frac{1}{2} \int_{\text{fluid}} \Bigg[& \frac{B_{1\perp}^2}{2\mu_0} + \frac{B_{0\perp}^2}{2\mu_0} (\nabla \cdot \boldsymbol{\xi}_\perp + 2\boldsymbol{\xi}_\perp \cdot \boldsymbol{\kappa})^2 + \gamma p |\nabla \cdot \boldsymbol{\xi}|^2 - \\ & 2(\boldsymbol{\xi}_\perp \cdot \nabla p)(\boldsymbol{\kappa} \cdot \boldsymbol{\xi}_\perp) - j_\parallel \left(\boldsymbol{\xi}_\perp \times \frac{\boldsymbol{B}_0}{B_0} \right) \cdot \boldsymbol{B}_1 \Bigg] dV \end{aligned} \tag{2.20}$$

$\boldsymbol{\kappa} = [(\boldsymbol{B}_0 \cdot \nabla)\boldsymbol{B}_0]/B_0^2$ represents the curvature of the equilibrium field. The first three terms of this formulation of the fluid component δW_F describe stabilizing effects: energy required to bend magnetic field lines (shear Alfvén wave), energy necessary to compress the magnetic field (compressional Alfvén wave) and energy required to compress the plasma (sound wave). The two terms in the second line of equation 2.20 can be positive or negative. The first one, which is proportional to ∇p is associated with *pressure driven* instabilities. The second one is proportional to $j_\parallel$. This becomes negative for *current driven* instabilities (e.g. kink instabilities).
The peeling-ballooning mode is a frequently discussed candidate for describing ELMs linearly. In the following the pressure driven ballooning mode and the current driven peeling mode are introduced separately. After that the coupled peeling-ballooning mode is discussed.

2.2.2.2 Pressure driven instabilities

The Rayleigh-Taylor instability occurs at the interface between two fluids of different densities, when the lighter fluid is pushing the heavier fluid. A similar instability called *interchange instability* can be observed in a plasma with a guiding magnetic field, which is then playing the part of gravity. The interchange instability is associated with a displacement that is assumed to be constant in phase along a field line ($k_\parallel = 0$).
As none of the parameters in the linearized equations for the displacement (2.13) has a dependence on the toroidal angle the toroidal eigenmodes are independent and can be treated

separately.[7] To fulfill the condition $k_\parallel = 0$ also only one single poloidal mode number m is regarded. Therefore in cylindrical geometry the radial displacement can be described as:

$$\xi_{m,n}(r,\theta,\phi) = \xi_{m,n}(r)e^{i(m\theta+n\phi)}. \tag{2.21}$$

It can be shown that the field line bending term in equation 2.20 vanishes in the vicinity of a resonant surface ($q \approx m/n$). In such a case the negative contribution from the pressure drive term can dominate. The sign of the pressure drive term is negative (positive), if the curvature vector $\boldsymbol{\kappa}$ and ∇p are parallel (anti-parallel). This is referred to as *unfavorable (favorable) curvature*. In cylindrical geometry the pressure drive term is always destabilizing. The stability in such a configuration versus localized interchange is described by the *Suydam criterion*:

$$-\frac{8\mu_0 p'}{r_{\mathrm{res}} B_z^2} < \left(\frac{q'}{q}\right)^2, \tag{2.22}$$

where r_{res} is the radial location of the resonant surface. The criterion describes the stabilizing effect of radial magnetic shear.

In a tokamak configuration the pressure drive term is destabilizing on the outboard side and stabilizing on the inboard side. For a large aspect ratio circular cross section tokamak the stability against interchange is described by the *Mercier criterion*

$$-\frac{8\mu_0 p'}{r_{\mathrm{res}} B_\phi^2}(1-q^2) < \left(\frac{q'}{q}\right)^2. \tag{2.23}$$

Thus in case of $q > 1$ (usual case) a tokamak is stable against interchange instabilities.

If one allows the perturbation to vary along a field line ($k_\parallel \neq 0$, $k_\parallel \ll k_\perp$) the perturbation can concentrate to the outboard side. For a sufficient pressure gradient the destabilizing energy can outweigh the energy necessary to bend the field lines. This type of instability called *ballooning instability* requires the interaction of multiple poloidal mode components. The radial displacement of such an eigenmode can be described as:

$$\xi_n(r,\theta^*,\phi) = \sum_m \xi_{mn}(r)e^{i(m\theta^*+n\phi)}, \tag{2.24}$$

where θ^* is the straight field line angle, m is the poloidal mode number and n is the toroidal mode number. The single (m,n)-components are parallel to the field lines (i.e. constant in phase along field lines). The inclination is introduced by an overlap of neighboring components.
To study this visually in the following a perturbation structure for a cylindrical tokamak (infinite aspect ratio tokamak) is constructed with maximum amplitude in one poloidal position and minimum amplitude in the opposite position [38]. The radial eigenfunctions $\xi_{m,n}$ are modeled by a convolution of Gaussians with a finite overlap with their neighbors and an overall envelop function that concentrates the main displacement to the plasma edge (figure 2.2(a)). Figure 2.2(b) shows the resulting structure of the displacement as a function of the poloidal position. The perturbation amplitude peaks on the right plasma boundary while it is negligible on the left plasma boundary. Towards the plasma center this amplitude generally approaches zero, which is an effect of the envelop function.

[7] Note that this is not the case if the perturbation has reached a level where non-linear effects have to be regarded!

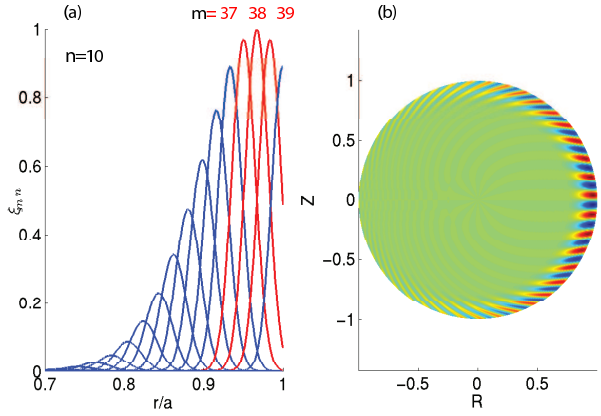

Figure 2.2: (a) Radial eigenfunctions ξ_{mn} for a cylindrical tokamak and $n = 10$. Eigenfunctions for $m = 37 - 39$ are highlighted in red. (b) Displacement as a function of poloidal position.

In a large aspect ratio circular cross section tokamak the most unstable pure high-n ballooning mode[8] has been shown to occur in the limit $n \to \infty$ [55].
A normalized quantity to describe the steepness of the edge pressure gradient in the context of pressure driven instabilities is

$$\alpha_{\text{circ}} = -\frac{2\mu_0 R_0 q^2}{B_\phi^2}\frac{dp}{dr}, \tag{2.25}$$

where R_0 is the major radius on the magnetic axis and B_ϕ is the local toroidal magnetic field. α_{circ} balances the destabilizing force due to pressure gradient and the stabilizing force due to field line tension (compare equation 2.20) assuming circular cross section. Equality of these forces corresponds to $\alpha_{\text{circ}} = 2$. A generalization towards arbitrary cross sections is given by [56]

$$\alpha = -\frac{\mu_0 \frac{dp}{d\psi}\frac{dV}{d\psi}\sqrt{\frac{V}{2\pi^2 R}}}{2\pi^2}. \tag{2.26}$$

This definition is used in the linear stability calculations for TCV with the code KINX (subsubsection 2.2.2.4).

2.2.2.3 Current driven instabilities

Kink modes are classical current driven instabilities. Internal kink modes (i.e. zero edge displacement) [57] have minor relevance in view of ELMs. The external kink mode is a current-driven instability, which has been suggest by Manickam [58] to be the instability associated with ELMs.
Peeling modes have finite displacement and finite current density at the plasma edge. If the corresponding resonant surface is just outside the LCFS the energy contribution from δW_S can be negative (destabilizing) for peeling modes. This has been shown by Laval [59] for pinch configurations with arbitrarily shaped cross sections. In circular plasmas the $n = 1$ peeling mode is the most unstable one.

[8] The corresponding expansion is in $1/\sqrt{n}$.

A more general peeling stability criterion has been proposed by Connor [60]:

$$\alpha_{\text{circ}} \left\{ \frac{r}{R} \left(1 - \frac{1}{q^2} \right) + s\Delta' - f_t \frac{Rs}{2r} \right\} > Rqs \left(\frac{j_{\parallel}^{\text{driven}}}{B} \right)_{\text{edge}}, \tag{2.27}$$

where Δ' is the radial derivative of the Shafranov shift[9], f_t is the trapped particle fraction and $j_{\parallel}^{\text{driven}}$ is the externally driven current. The first two terms on the left reflect the fact that the peeling mode for a weakly shaped, large aspect ratio equilibrium can be stabilized by a pressure gradient (1st term) or by a Pfirsch-Schlüter current (2nd term). The third term accounts for bootstrap current, which has a destabilizing effect on the peeling mode. In the banana collisionality regime this term is expected to be dominant on the left hand side. At higher collisionalities (lower f_t) this dominance is expected to vanish. In summary the peeling mode is expected to be unstable at low and stable at high collisionalities.
There are a number of characteristic differences between the radial mode structure of ballooning and peeling modes (figure 2.3). Peeling modes consist of a relatively low number of coupled poloidal Fourier harmonics [60]. The dominant poloidal component of peeling modes is usually the one with the resonant surface closest to the LCFS. Peeling mode extend further towards the plasma center. Therefore it is possible to distinguish these modes on the basis of the radial mode structure.
The effect of X-point and LCFS on the stability of peeling modes has been studied analytically [61]. It has been found that despite $\delta W < 0$, the growth rate tends to zero as the outermost flux surface approximates a LCFS with an X-point.

2.2.2.4 Peeling-Ballooning modes

It was suggested by Connor [60] that ballooning modes coupled to peeling modes might play an important part in the physics of ELMs. In such a peeling-ballooning mode the displacement structure would find a hybrid state between both types of instabilities. In this situation δW would be minimized and in particular it would be lower than for a pure peeling mode or for a pure ballooning mode.
Two ways to study peeling-ballooning modes have been applied. The first approach derives an energy functional δW for the peeling-ballooning mode by expansion in $1/n$ and transformation into an appropriate coordinate system [55]. Also it is possible to numerically solve the linearized set of MHD-equations in straight field line coordinates. In order to analyze the dependence of the stability on the two MHD instability drives a reference equilibrium is modified in normalized edge pressure gradient and toroidal current density. For each point in this space the largest growth rate over all toroidal mode numbers regarded is considered. Lower values of this growth rate correspond to stability, while higher ones are related to instability. A natural stability boundary is at the growth rate $\gamma = 0$. Often stabilization due to diamagnetic drift is accounted for, which increases the stability boundary to $\gamma = \omega_{*i}/2$ [38, 62], where the ion diamagnetic drift frequency is defined as

$$\omega_{*i} = \frac{1}{e \cdot n} \frac{dp_i}{d\psi}. \tag{2.28}$$

[9]The Shafranov shift is an outward displacement of the centers of magnetic flux surfaces with respect to the center of the bounding surface. This displacement increases with increasing β_p.

Figure 2.3 shows the ideal MHD stability map for a TCV discharge obtained by calculations with the code KINX [63]. Along the stability boundary separating stable and instable regions three sections can be distinguished:

- At high α and low $j_\parallel/\langle j\rangle$ high n modes of type ballooning first become unstable.
- At high α and high $j_\parallel/\langle j\rangle$ intermediate n modes of type peeling-ballooning first become unstable.
- At low α and high $j_\parallel/\langle j\rangle$ low n modes of type peeling first become unstable.

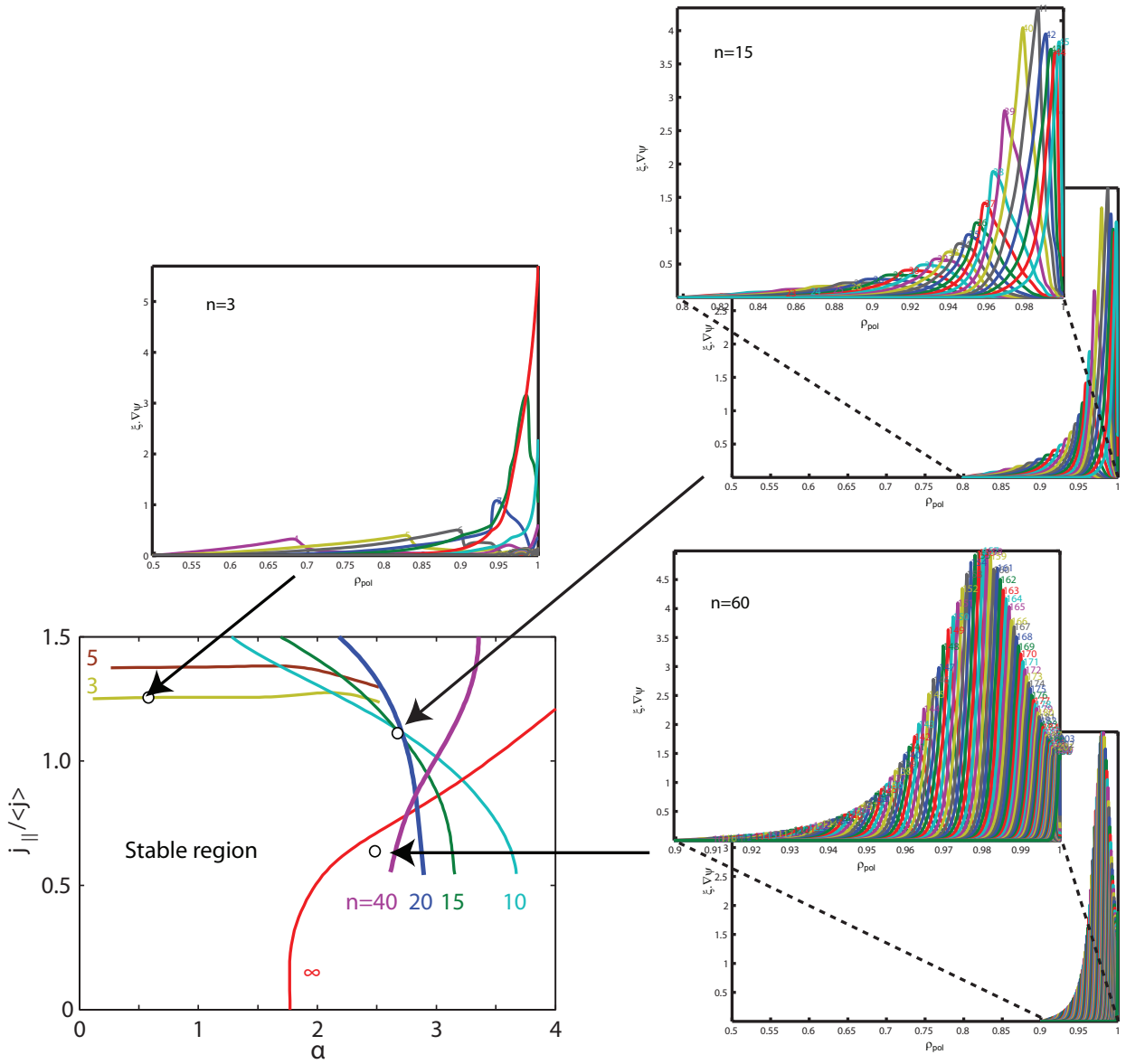

Figure 2.3: Bottom left: Ideal MHD stability map for discharge TCV38008 obtained by calculations with the code KINX [63]. The stability lines correspond to $\gamma = 0$. $j_\parallel/\langle j\rangle$ is the normalized parallel current density at maximum pressure gradient. The figure is adapted from [64]. Other figures: Radial displacement structure for three positions on the stability boundary ($n = 3$, $n = 15$ and $n = 60$). For $n = 15$ and $n = 60$ radial close-ups are displayed additionally.

The instability types for the first and the last case can be inferred from the radial mode structure, which is plotted in figure 2.3 for the three types. In the middle case ($n = 15$ dominant) an intermediate number of poloidal mode components are coupled. Furthermore the displacement of the outermost component ($m = 45$) has a higher maximum value compared to the next two components ($m = 44$ and $m = 43$) and a lower maximum value compared to the dominant component ($m = 41$). This suggest that the mode has both peeling and ballooning characteristics.

Is there an upper limit on the pressure gradient due to peeling-ballooning modes? Figure 2.4 shows stability diagrams for ballooning modes in the α-s-space[10] calculated on the basis of [55]. Applying the model describing flux surfaces as concentric circles there are two stability regions:

- **1st stability region**: Left of upper branch of stability boundary. This is the region each discharge has to start in.
- **2nd stability region**: Below lower branch of stability boundary

Transferring from concentric circles to cycles with different centers (i.e. allowing for Shafranov shift) connects both stability regions. As α and s are coupled by the Bootstrap current there is only limited flexibility in changing the discharge trajectory in α-s-space. In the figure these trajectories would start from the top left region and propagate to the right and downwards, when increasing the pressure gradient. Thus the crucial question is, whether the trajectory can pass the stability boundary at low α and s. The access to the second stability regions is supported by conditions that lead to field lines running longer through regions of favorable curvature than through areas of unfavorable curvature. One of these conditions is a large Shafranov shift at high β_p as shown in figure 2.4. Another condition supporting second stability access is high elongation and high triangularity [65]. Ozeki showed that the DIII-D plasma can be moved into the connection between first and second stability region [65].
The question, whether the peeling-ballooning stability can explain the onset of ELMs, is of high importance. To address this question an operational point reflecting the conditions in an experiment is introduced in the stability diagram. The coordinates of this point correspond to α and j_ϕ in the experiment - often in various phases of the ELM cycle. In [66] it has been shown for a JET discharge that 2ms before type I ELMs the operational point is close to the stability boundary in contrast to after the ELM, where the operational point is in the stable region. However results of such investigations should be treated with care due to experimental uncertainties with respect to α and j_ϕ. The value of the toroidal current density j_ϕ is usually not measured but often inferred using the formula proposed in [23, 24]. For a single H-mode phase the edge current density has been measured by exploiting the Zeeman effect in lithium [67]. The obtained profiles were in fair agreement with neoclassical estimations. A systematic comparison of such measured and calculated edge current density profiles has not been performed. Furthermore it has been shown that a misalignment of the pressure input data relative to the magnetic input data of a few mm has a large impact on the stability calculated by ILSA [68].

[10] For a large aspect ratio tokamak one can show that $s \propto 1/j$.

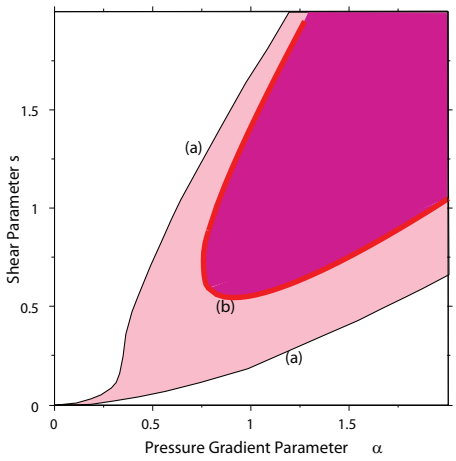

Figure 2.4: Diagram of ballooning stability regions in the space spanned by normalized pressure gradient α and normalized shear s. The stability calculations have been performed by H.P. Zehrfeld in a semi-analytical way on the basis of [55]: (a) Flux surfaces modeled poloidally by concentric circles. (b) Flux surfaces modeled poloidally by circles.

2.2.3 Non-Linear evolution

At some stage during the growth of an ELM the perturbation becomes significant compared to the equilibrium quantities. Under these conditions the assumption that led to the linearized set of equations 2.13 is not justified anymore. Therefore a linearized model is not a good description for such a situation.
What is the relevance of the non-linear evolution of ELMs? The analysis of a DIII-D ELM has shown similarities between the radial structures of the eigenfunction related to a certain toroidal mode number and the electron temperature pedestal erosion during the ELM (ELM affected area) [69]. On the basis of this it has been speculated, that the ELM size is determined by the linear structure of the instability [69]. However for type-I ELMs at JET it has been shown that similar affected area in electron temperature can correspond to significantly different sizes of ELMs [42]. It has been concluded that quantitative predictions of the ELM size requires non-linear studies [70].

In a non-linear situation the individual toroidal mode components can not be treated separately any more. Furthermore approaches similar to the ones presented in context to the energy principle are not possible. Wilson and Cowley [71, 72, 62] have elaborated an extension of the ballooning mode theory [55, 73] for the early non-linear phase. Non-linearities accounting for weakening of the field (making it easier for the field lines to be displaced outwards) and changes in the mean pressure profile due to the perturbation have been introduced.
A number of interesting results have been extracted from this model. The poloidal flux is expected to develop finger shaped perturbations pointing radially outward. The growth of these fingers is expected to be *explosive* (i.e. $\xi \propto (t_0 - t)^{-\lambda},\ 1 < \lambda < 2$). The mathematical treatment breaks down before the singularity is reached and it is not expected that the radial velocity of the finger exceeds the speed of sound [71]. The fingers are predicted to narrow in the perpendicular direction. If several fingers are initialized, one is expected to eventually dominate and suppress the others [71].

2.3 Reduced Magnetohydrodynamics

The code JOREK described in section 2.4 uses a version of the MHD model applying further assumptions. This model called *reduced magnetohydrodynamics* has been derived by Strauss [74, 75]. In addition to the standard assumptions of MHD the following assumptions are made:

- Only perturbations of the magnetic field within the poloidal plane are regarded ($\lambda_\perp/\lambda_\parallel \approx \epsilon,\ \lambda_\perp/a \approx \epsilon$). This leads to the suppression of fast magnetosonic waves, which significantly constrain the computational speed of solving the full MHD equations but do not significantly contribute to instabilities [76]. This implies as well that the current density has only a toroidal component.
- The toroidal magnetic field dominates over the poloidal magnetic field ($B_\phi \gg B_{pol}$).

Consequently the magnetic field can be described as

$$\boldsymbol{B} = (F_0 \hat{e}_\phi + \nabla\psi \times \hat{e}_\phi)/R, \tag{2.29}$$

which leads to a similar expression for the fluid velocity:

$$\boldsymbol{v} = v_\parallel \boldsymbol{B} - R\nabla u \times \hat{e}_\phi. \tag{2.30}$$

On the basis of this it is possible to reduce the MHD equations to a set that is less complex to solve numerically. The reduced MHD model used in JOREK includes also terms accounting for resistivity and viscosity. Additionally conductive and diffusive terms to describe transport effects as well as particle and heat source terms are in place. A good overview of the physics in JOREK is given by the following form of the equations, where $\boldsymbol{B}$ and $\boldsymbol{v}$ is not yet replaced by the terms given in 2.29 and 2.30:

$$j = \Delta^*\psi = R\frac{\partial}{\partial R}\left(\frac{1}{R}\frac{\partial\psi}{\partial R}\right) + \frac{\partial^2\psi}{\partial Z^2}, \tag{2.31}$$

$$\omega = \nabla^2_{pol} u = \frac{1}{R}\frac{\partial}{\partial R}\left(R\frac{\partial u}{\partial R}\right) + \frac{\partial^2 u}{\partial Z^2}, \tag{2.32}$$

$$\frac{\partial\psi}{\partial t} = \eta j - (\boldsymbol{v}_{pol}\cdot\nabla)\psi - F_0\frac{\partial u}{\partial\phi}, \tag{2.33}$$

$$\frac{\partial\rho}{\partial t} = -\nabla\cdot(\rho\boldsymbol{v}) + \nabla\cdot(D_\perp\nabla_\perp\rho) + S_\rho, \tag{2.34}$$

$$\rho\frac{\partial T}{\partial t} = -\rho\boldsymbol{v}\cdot\nabla T - (\gamma-1)p\nabla\cdot\boldsymbol{v} + (K_\perp\nabla_\perp T + K_\parallel\nabla_\parallel T) + S_T, \tag{2.35}$$

$$\hat{e}_\phi \times \rho\frac{\partial\boldsymbol{v}}{\partial t} = \hat{e}_\phi \times \left\{-\rho(\boldsymbol{v}\cdot\nabla)\boldsymbol{v} - \nabla p + \boldsymbol{J}\times\boldsymbol{B} + \nu\Delta\boldsymbol{v}\right\}, \tag{2.36}$$

$$\boldsymbol{B}\cdot\rho\frac{\partial\boldsymbol{v}}{\partial t} = \boldsymbol{B}\cdot\left\{-\rho(\boldsymbol{v}\cdot\nabla)\boldsymbol{v} - \nabla p + \boldsymbol{J}\times\boldsymbol{B} + \nu\Delta\boldsymbol{v}\right\}. \tag{2.37}$$

Equations 2.31 and 2.32 define the toroidal current density j and the vorticity ω, which are directly expressed in terms of the two flux functions ψ and u. Equations 2.33 to 2.37 describe how the quantities ψ, ρ and T and projections of $\boldsymbol{v}$ evolve in time. $D_\perp$ is the particle diffusivity, $K_\perp$ and $K_\parallel$ are the perpendicular and parallel heat diffusivity, S_ρ and S_T are the particle and heat sources and ν is the kinematic viscosity. The final form of the equations and a complete derivation from the MHD equations can be found in [77].

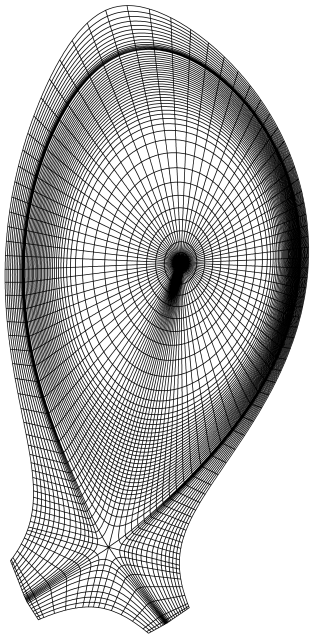

Figure 2.5: Flux-surface aligned X-point grid of the JOREK simulation with 5500 Bezier finite-elements: The number of grid points are: 96 poloidal points, 40 radial points inside the LCFS, 15 radial points outside the LCFS, 9 "radial" points in the private flux region, and 9 grid points along the divertor legs.

2.4 The non-linear MHD-code JOREK

The non-linear code JOREK has been developed by Huysmans and others with the specific aim to simulate ELMs [34]. JOREK versions according to a range of physics modules are developed or under development. Here, only the version employed for this work will be detailed [78].
JOREK evolves seven scalar variables in time: poloidal flux ψ, stream function u, toroidal current density j, toroidal vorticity ω, mass density ρ, temperature T and parallel velocity component $v_\parallel$. The evolution of these variables is described by the set of reduced MHD equations 2.29 to 2.37. The variables are discretised in the poloidal plane by cubic Bezier type elements [79] shown in figure 2.5. The finite element grid in the poloidal plane is aligned with the equilibrium flux surfaces. The domain includes the confined plasma region, the SOL region and the private flux region. The finite element grid features an X-point and also divertor target plates. For the simulation discussed in this work a grid with 5500 Bezier elements has been used.
The toroidal direction is resolved by Fourier harmonics. The number of toroidal mode components and their periodicity[11] can be chosen separately. Typically a limited number of mode components and often only $n = 0$ and one further component are chosen. The focus of the simulation analyzed in this work, which is described in [78], is on high toroidal resolution. Consequently the full set of toroidal mode components $n = 0, 1, 2, ..., 16$ is used.
For the time evolution a fully implicit system (linearized Crank-Nicholson) is used. This re-

[11] A periodicity p reduces the set of regarded toroidal mode components to $0, p, 2p, 3p, ...$.

sults in a sparse matrix, which is solved using GMRES.[12] For each time step preconditioning is applied separately to the sub-matrices corresponding to the individual toroidal harmonics using PaStiX[13] [80].
The boundary conditions for ψ are dependent on the location but fixed in time. In the regions where the equilibrium field is parallel to the boundary a Dirichlet boundary condition with $\psi_0 = \text{const}$ is applied. In the residual boundary sections (i.e. along the divertor targets) ψ_0 is varying as in the equilibrium reconstruction used as input (see below).

The simulation analyzed in this work has been performed on the basis of experimental data from ASDEX Upgrade discharge AUG23221 at 4.7s. An overview of the plasma parameters for this discharge is given in table 4.2. As input parameters for the JOREK simulation experimentally measured temperature and density profiles and the output from an equilibrium reconstruction with the CLISTE code [81] have been used. More information on the JOREK version employed in the context of this work and especially on the simulation discussed in chapter 6 can be found in [78] referred to as `eta5`.

[12] GMRES (Generalized minimal residual method) is an iterative method for the numerical solution of a non-symmetric, sparsely populated systems of linear equation.

[13] PaStiX (Parallel Sparse Matrix Package) is a scientific library that provides a high performance parallel solver for very large sparse linear systems based on direct methods.

Chapter 3

Synthetic magnetic diagnostics

This chapter describes the development of a synthetic magnetic diagnostic module (SYNMAG) acting as a post processor on JOREK simulation results.
As described in section 2.4 the code JOREK simulates the evolution of the poloidal magnetic flux ψ. In the ASDEX Upgrade studies analyzed in this thesis, this is done in the domain $\partial\Omega_J$, which is fully embedded in the ASDEX Upgrade vessel cross section $\partial\Omega_A$ as shown in figure 3.1. $\partial\Omega_A$ includes a number of conducting structures on the inboard side and the passive stabilising loop (PSL). The majority of magnetic diagnostics in ASDEX Upgrade and particularly the printed circuit probes measuring the radial magnetic field component are situated outside $\partial\Omega_J$. Hence in order to model the signals in the ASDEX Upgrade pickup coils corresponding to the evolution of the magnetic field structure evaluated by JOREK, the continuation of the magnetic field structure outside $\partial\Omega_J$ has to be calculated.

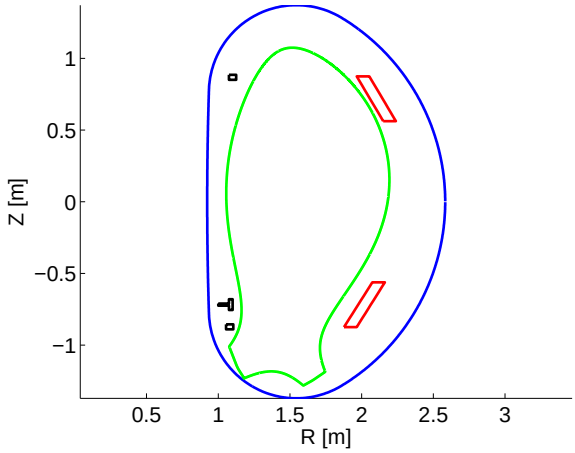

Figure 3.1: JOREK calculation domain $\partial\Omega_J$ (green) fully embedded in the ASDEX Upgrade vessel cross-section (blue). Also shown are contours of the passive stabilising loop (red) and three conducting assemblies installed on the inboard side (black).

In JOREK calculations the non-toroidal current components are zero in the equilibrium (pre ELM state). The maximum perturbed values of non-toroidal currents are more than one order of magnitude lower than the maximum toroidal currents in their direct vicinity. Therefore non-toroidal currents are neglected in the following. Combining Ampère's law and the definition of the magnetic field by the poloidal magnetic flux results in a partial differential equation describing the relation between ψ and the current density in the toroidal

direction j_ϕ

$$\begin{aligned} \triangle^* \psi &= -g(R,Z), \\ \triangle^* \psi &= R\frac{\partial}{\partial R}(\frac{1}{R}\frac{\partial \psi}{\partial R}) + \frac{\partial^2 \psi}{\partial Z^2}, \\ g(R,Z) &= R\mu_0 j_\phi. \end{aligned} \tag{3.1}$$

JOREK evaluates the evolution of the poloidal magnetic flux ψ_J within Ω_J. Due to the JOREK boundary conditions (section 2.4) for ψ_J the perturbation flux $(\psi_J - \psi_{J,0})$ on $\partial\Omega_J$ is artificially fixed to 0. This has an effect corresponding to a virtual ideal conducting wall at $\partial\Omega_J$. It influences the simulated magnetic field inside $\partial\Omega_J$. An ideal conducting wall at $\partial\Omega_J$ would cause the magnetic perturbation flux outside $\partial\Omega_J$ even to be set to zero.
In tokamak experiments transient magnetic field perturbations induce eddy currents at the surface of conducting structures. This can be quantified by the induction law combined with Ohm's law. If the structure is an ideal conductor, the induced currents will have a magnetic field that exactly cancels the component of the magnetic field perturbation, which is normal to the surface. Thus the superposition of the perturbation field and the field from the eddy currents has zero component in the direction normal to the surface, which is corresponding to ψ being constant on this surface. In order to test this effect on the real ASDEX Upgrade vessel the evolution of the poloidal magnetic field has been recorded in identical positions inside and outside the vessel. Analysis of this experiment led to the conclusion, that the ASDEX Upgrade vessel can be considered as an ideal conductor for frequencies higher than 1kHz [7].
The question, which structures installed in ASDEX Upgrade have to be considered as conductive for the construction of synthetic magnetics, has no obvious answer. However considering the same set of structures as in [7] leads to reasonable agreement between simulation and experiment (subsection 3.2.7). This set consists of the following items:

- The ASDEX Upgrade vessel
- A number of assemblies installed on the magnetic high field side
- The passive stabilising loop (PSL)

All listed structures can be seen in figure 3.1. All of these structures except the PSL are connected in a conducting way to each other. Therefore it is appropriate to assign them all the same value of ψ as boundary condition. The PSL in contrast is isolated from the other structures and thus does not necessarily have the same poloidal flux. This special PSL boundary condition is accounted for in a later step of the approach described in subsection 3.2.5.

In summary in order to convert ψ_J into magnetic signals as they would be measured in ASDEX Upgrade a post processing approach with the following properties has to be elaborated:

- The effect of the JOREK boundary condition has to be compensated.
- The effect of the main conducting structures in ASDEX Upgrade has to be accounted for.

The post processing module SYNMAG is developed to perform this steps. In addition to this approach (operation mode: JOREK-ψ) SYNMAG offers other operation modes, that allow the calculation of synthetic magnetic fields on the basis of distributions of toroidal current density either from JOREK (operation mode: JOREK-j) or from an analytical

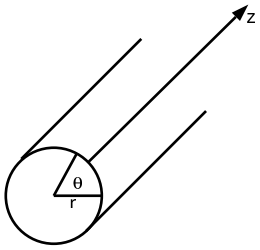

Figure 3.2: Cylindrical coordinate system for the analytical model

input (operation mode: Play).
For the solution of the associated differential equations PLTMG 10.0 [82] is used, which is a software package for solving elliptic partial differential equations in general regions of the plane. It is based on continuous piecewise polynomial triangular finite elements.

3.1 Analytical Model

The problem described above is modeled in a simplified version. This improves understanding in the given problem and provides the possibility to analytically test the developed post processing approach. Furthermore with this model it is possible to estimate the impact of the JOREK boundary condition on the plasma.
Instead of toroidal geometry with non circular flux surfaces cylindrical geometry with circular flux surfaces and coordinates (r, θ, z) as illustrated in figure 3.2 are chosen. Furthermore the current perturbation is described by a single poloidal mode number m and only current in the z-direction is considered. This current can be written as

$$j_z = \begin{cases} \cos(m\theta) & \text{for } r \leq r_P \\ 0 & \text{for } r > r_P \end{cases}, \tag{3.2}$$

where r_P is the radius of the plasma column. The magnetic field is expressed by the poloidal flux for the cylinder geometry

$$\boldsymbol{B} = -\nabla\psi \times \hat{e}_z. \tag{3.3}$$

Inserting into Ampère's Law yields

$$\frac{1}{r}\left[\frac{\partial}{\partial r}\left(-r\frac{\partial\psi}{\partial r}\right) - \frac{\partial}{\partial\theta}\left(\frac{1}{r}\frac{\partial\psi}{\partial\theta}\right)\right] = \mu_0 j_z. \tag{3.4}$$

In order to separate variables it is possible to set $\psi(r,\theta) = f(r)\cos(m\theta)$, where f is a function to be determined and $\cos(m\theta)$ reflects the fact that the symmetry imposed by the current is maintained by the magnetic field. This leads to[1]

$$f' + rf'' - \frac{1}{r}m^2 f = \begin{cases} r\mu_0 & \text{for } r \leq r_P \\ 0 & \text{for } r > r_P \end{cases} \tag{3.5}$$

[1]Here the notation $f' = \dfrac{\partial f}{\partial r}$ is used.

Depending on the radial position this constitutes an inhomogeneous and a homogeneous differential equation respectively. Solutions of these differential equations are[2]

$$\begin{aligned} f_{\text{inhom}} &= a_1 r^m + a_2 r^{-m} + \frac{\mu_0}{4-m^2} r^2, \\ f_{\text{hom}} &= a_1 r^m + a_2 r^{-m}. \end{aligned} \tag{3.6}$$

3.1.1 System without conducting wall

If there is no conducting wall at r_J and only vacuum outside the plasma, it is straightforward to derive a solution. This solution f_V can not go to infinity at r=0 and at $r \to \infty$. This constrains f_V in the following way

$$\begin{aligned} f_V^I &= a_1 r^m + \frac{\mu_0}{4-m^2} r^2 \text{ for } r \leq r_P, \\ f_V^O &= a_2 r^{-m} \text{ for } r > r_P. \end{aligned} \tag{3.7}$$

In order to ensure the magnetic field to be well-defined at r_P and to exclude surface currents at r_P, the following matching conditions at r_P have to be fulfilled

$$\begin{aligned} f_V^I(r_P) &= f_V^O(r_P), \\ \frac{\partial f_V^I}{\partial r}(r_P) &= \frac{\partial f_V^O}{\partial r}(r_P). \end{aligned} \tag{3.8}$$

This leads to the solution

$$f_V = \begin{cases} \dfrac{\mu_0}{4-m^2}\left[r^2 - \left(\dfrac{1}{m} + \dfrac{1}{2}\right) r_P^{2-m} r^m\right] & \text{for } r \leq r_P, \\ \dfrac{\mu_0}{4-m^2}\left(-\dfrac{1}{m} + \dfrac{1}{2}\right) r_P^{2+m} r^{-m} & \text{for } r > r_P. \end{cases} \tag{3.9}$$

Outside the plasma the radial decay is stronger for higher poloidal mode numbers.

3.1.2 System with ideal conducting wall

An ideal conducting wall at r_J implies $\psi(r_J, \theta) = \text{const}$. This can only be satisfied by $f(r_J) = 0$. The solution of this system is split into

$$f = f_V + f_{WJ}$$

where f_V is again the solution without the conducting wall derived in 3.1.1 and f_{WJ} represents the effect of the wall at r_J namely the magnetic field due to the surface currents on the surface at $r = r_J$. Thus f_{WJ} satisfies the homogeneous differential equation and fulfills the conditions

$$\begin{aligned} & f'_{WJ} + r f''_{WJ} - \frac{1}{r} m^2 f_{WJ} = 0, \\ & f_{WJ}(r_J) = -f_V(r_J), \\ & f_{WJ} \neq \pm\infty \text{ for } r = 0 \text{ and } r \to \infty. \end{aligned} \tag{3.10}$$

[2]For m=2 in the inhomogeneous case a special solution is $f(r) = \frac{\mu_0}{16} r^2 (4 \ln r - 1)$.

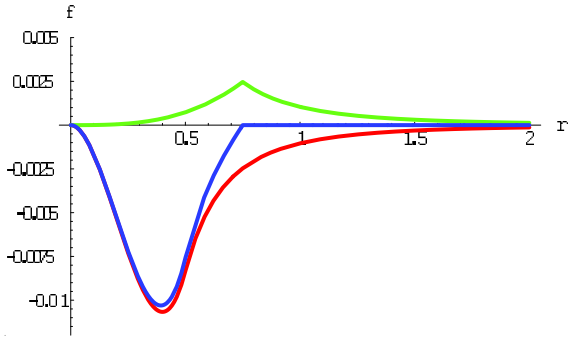

Figure 3.3: Decomposition of the radial perturbation structure f (blue) into f_V (red) and f_{WJ} (green). Parameters: $r_P = 0.5$, $r_J = 0.75$, $m = 3$

This constrains f_{WJ} in the following way

$$\begin{aligned} f_{WJ} &= a_1 r^m \text{ for } r \leq r_J, \\ f_{WJ} &= a_2 r^{-m} \text{ for } r > r_J. \end{aligned} \tag{3.11}$$

The matching conditions for this system are

$$\begin{aligned} f^I_{WJ}(r_J) &= -f_V(r_J), \\ f^O_{WJ}(r_J) &= -f_V(r_J). \end{aligned} \tag{3.12}$$

Taking all into account one arrives at the solution for f_{WJ}

$$f_{WJ} = \begin{cases} \dfrac{\mu_0}{2m(2+m)} r_P^{2+m} r_J^{-2m} r^m & \text{for } r \leq r_J \\ \dfrac{\mu_0}{2m(2+m)} r_P^{2+m} r^{-m} & \text{for } r > r_J. \end{cases} \tag{3.13}$$

Figure 3.3 shows the decomposition of f into components f_V and f_{WJ}. f is zero for $r > r_J$ and its graph has a kink at $r = r_J$. The extent of this kink can be set in relation to the current density on the surface $r = r_J$ (subsection 3.2.2). While the graph of f_V has no kink, the graph of f_{WJ} has a cusp at $r = r_J$ with

$$\lim_{r \nearrow r_P} f'_{WJ} = -\lim_{r \searrow r_P} f'_{WJ} = 0.5 \lim_{r \nearrow r_P} f'. \tag{3.14}$$

There is a damping effect of the ideal conducting wall on the plasma perturbation. In a synthetic magnetics module acting as a post-processor it is generally not possible to correct this. The effect can be quantified by the damping factor for the perturbation of poloidal flux ψ/ψ_V. For $r_P \leq r \leq r_J$ this factor becomes

$$\frac{\psi}{\psi_V} = 1 + \frac{\psi_{WJ}}{\psi_V} = 1 - \left(\frac{r}{r_J}\right)^{2m}. \tag{3.15}$$

Therefore in the limit $r = r_P$, where the damping is strongest in the plasma, the damping factor introduced by the conducting wall for dimensions similar to the ASDEX Upgrade case ($r_P = 0.5$m and $r_J = 0.75$m) is 56% for $m = 1$ and 99.97% for $m = 10$. The implications of this damping effect on the plasma perturbations in JOREK simulations are discussed in section 6.3.

3.2 Synthesis of magnetic signals

This section describes the development of an approach for the synthesis of magnetic signals, where $\partial\psi_J/\partial n$ on $\partial\Omega_J$ is used as input data. The approach fulfills all requirements detailed above. The main step consists in the solution of the no-wall problem (i.e. compensating the JOREK boundary condition). To achieve this Green's function is applied. Subsections on a special boundary treatment for the passive stabilising loop and synthetic magnetic probes finalize the chapter.

3.2.1 Concept

The poloidal magnetic flux ψ is described as $\psi(t) = \psi_0 + \tilde{\psi}(t)$, where ψ_0 is the flux function at the start of the investigated period and $\tilde{\psi}(t)$ is the perturbation from this. As the signals measured by pickup-coils are proportional to $\partial\psi/\partial t$, which is equal to $\partial\tilde{\psi}/\partial t$, it is correct to describe the magnetic perturbation field structure evaluated by JOREK by $\tilde{\psi}$. Furthermore using $\tilde{\psi}$ for the calculations has the advantage that the investigated perturbation structures are not masked by ψ_0, which is larger by several orders of magnitude. Consequently the JOREK boundary condition turns into

$$\tilde{\psi}_J(t) = 0 \text{ on } \partial\Omega_J. \tag{3.16}$$

For simplicity of notation in the remainder of this chapter the notation ψ_J with identical meaning to $\tilde{\psi}_J$ will be used.
Corresponding to an ideal conducting wall at $\partial\Omega_J$, this poloidal flux ψ_J defined on Ω_J can be continuously extended to Ω_A:

$$\psi_{JE} = \begin{cases} \psi_J & \text{in } \Omega_J \\ 0 & \text{in } \Omega_A \setminus \Omega_J. \end{cases} \tag{3.17}$$

The central idea of the approach is as follows: With the definition made above, approaching from the plasma center the normal derivative of ψ_{JE} jumps at $\partial\Omega_J$ from a finite value to 0. This jump originates from the JOREK boundary condition ($\psi_J = 0$ on $\partial\Omega_J$), corresponding to surface currents on a virtual ideal conducting wall at $\partial\Omega_J$, which has the effect of a constant flux outside Ω_J.
On the basis of this consideration an approach in two steps has been developed:

- In the first step the solution ψ_V of the no-wall problem is calculated. This corresponds to the situation without the JOREK boundary condition (i.e. without surface current on $\partial\Omega_J$) but with the current density distribution j_{JE}:

$$j_{JE} = \begin{cases} j_J & \text{in } \Omega_J \setminus \partial\Omega_J \\ 0 & \text{in } \Omega_A \setminus \Omega_J. \end{cases} \tag{3.18}$$

  ψ_V can be expressed as

$$\psi_V = \psi_{JE} - \psi_{WJ} \tag{3.19}$$

  where ψ_{WJ} is the flux component stemming form the surface currents on $\partial\Omega_J$. ψ_{WJ} is constructed from Green's functions.

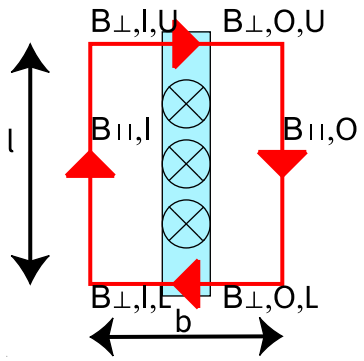

Figure 3.4: Magnetic field structure (red) of current filaments directed into the plane in a vertical surface current layer $\partial\Omega$ (light blue)

- In the second step the effect of the conducting structures in the experiment is accounted for by adding the solution ψ_{WA} of the following PDE on Ω_A

$$\begin{aligned} \triangle^* \psi_{WA} &= 0, \\ \psi_{WA} &= -\psi_V \text{ on } \partial\Omega_A. \end{aligned} \tag{3.20}$$

  The superimposed solution has the following properties

$$\begin{aligned} \psi &= \psi_V + \psi_{WA} \text{ on } \partial\Omega_A, \\ \triangle^* \psi &= -r\mu_0 j_{JE}, \\ \psi &= 0 \text{ on } \partial\Omega_A. \end{aligned} \tag{3.21}$$

  As discussed above the poloidal flux on Ω_A has to be constant corresponding to an ideal conducting structure.

3.2.2 Surface current density

The surface current density on an internal boundary $\partial\Omega$ corresponding to a given flux function ψ can be calculated starting from the integral form of Ampère's law:

$$\oint_S \boldsymbol{B} d\boldsymbol{s} = \mu_0 I, \tag{3.22}$$

where S corresponds to the red line in figure 3.4 and I is the current in the part of $\partial\Omega$ surrounded by S.
Expanding the left side of the equation and introducing the surface current density σ into the positive ϕ-direction (current per length - [A/m]) and assuming an infinitesimal thin current layer and homogeneity this becomes

$$l(B_{\parallel,I} - B_{\parallel,O}) + \frac{b}{2}(B_{\perp,I,U} - B_{\perp,I,L} + B_{\perp,O,U} - B_{\perp,O,L}) = l\mu_0\sigma. \tag{3.23}$$

Dividing by l and going to the limit $b \to 0$ gives

$$B_{\parallel,I} - B_{\parallel,O} = \mu_0\sigma \text{ on } \partial\Omega. \tag{3.24}$$

$B_\parallel$ can be expressed as

$$\frac{1}{R}\nabla\psi \cdot \boldsymbol{n} = \frac{1}{R}\frac{\partial\psi}{\partial n}, \tag{3.25}$$

where $\boldsymbol{n}$ is the outgoing normal unit vector on $\partial\Omega$. This leads to

$$\frac{1}{R}\left(\frac{\partial\psi^I}{\partial n} - \frac{\partial\psi^O}{\partial n}\right) = \mu_0\sigma \text{ on } \partial\Omega. \tag{3.26}$$

With the definition of the function ψ_{JE} made above, the surface current density in the investigated case can be described as

$$\frac{1}{R}\frac{\partial\psi^I_{JE}}{\partial n} = \mu_0\sigma \text{ on } \partial\Omega_J, \tag{3.27}$$

where ψ^I_{JE} is the flux inside $\partial\Omega_J$.

3.2.3 Green's function

Once the surface current density is known its transformation into magnetic fields is described by Green's function G. $G(\boldsymbol{r}, \boldsymbol{r}^*)$ is the poloidal flux a the point $\boldsymbol{r} = (R, Z)$ (observation point) originating from a current filament through $\boldsymbol{r}^* = (R^*, Z^*)$ (source point), which has a toroidal direction. In (R,Z)-coordinates the current density can be described by

$$g_{\text{fil}}(R, Z) = r\delta(R - R^*)\delta(Z - Z^*). \tag{3.28}$$

Using the ϕ-component[3] of the vector potential A_ϕ corresponding to such a current calculated in [83] and the fact that in this geometry ψ is equal to $-A_\phi R$ leads to

$$\begin{aligned} G(\boldsymbol{r}, \boldsymbol{r}^*) &= \frac{1}{\pi}\sqrt{\frac{RR^*}{k^2}}\left[(1 - \frac{1}{2}k^2)K(k) - E(k)\right] \text{ with} \\ k^2 &= \frac{4RR^*}{(R + R^*)^2 + (Z - Z^*)^2}, \end{aligned} \tag{3.29}$$

where K and E are elliptic integrals of the first and second kind. Figure 3.5 illustrates an example of the function G. When the source point is identical to the observation point G gets singular. In all other locations the surface plotted in figure 3.5 has a mean curvature equal to zero, which is equivalent to the surface being a *minimal surface*.
In general Green's function is the solution of a differential equation with a δ-function as source:

$$\triangle^* G(\boldsymbol{r}, \boldsymbol{r}^*) = -R\delta(R - R^*)\delta(Z - Z^*) \tag{3.30}$$

For a system with currents in the toroidal direction only the vacuum flux function ψ_V is the superposition of the flux contributions of all current filaments in the domain Ω weighted by $\mu_0 j_\phi$

$$\psi_V(\boldsymbol{r}) = \int_\Omega G(\boldsymbol{r}, \boldsymbol{r}^*)\mu_0 j_\phi(R^*, Z^*)dR^*dZ^* = \int_\Omega G(\boldsymbol{r}, \boldsymbol{r}^*)\frac{g(R^*, Z^*)}{R^*}dR^*dZ^*, \tag{3.31}$$

where $g(R, Z) = R\mu_0 j_\phi$.

[3] $A_r = A_z = 0$

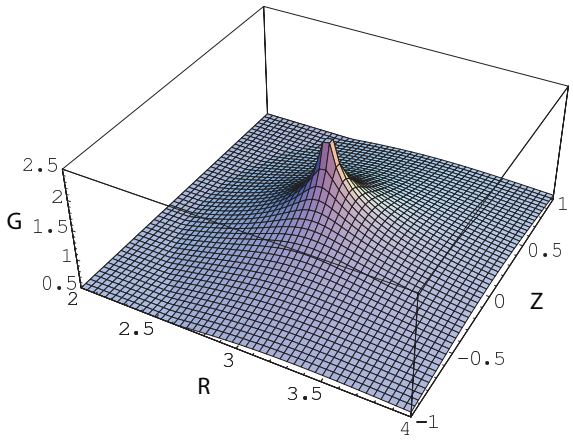

Figure 3.5: Green's function for poloidal flux with fixed source point coordinates $R^* = 3$ and $Z^* = 0$ and variable observation point coordinates.

3.2.4 Solution of the no-wall problem

Now the surface current density and Green's function can be used to calculate on $\Omega_A \setminus \Omega_J$ the flux ψ_{WJ} associated with the virtual currents in $\partial\Omega_J$ as described by equation 3.27. This can be done by evaluating in contrary to the surface integral of equation 3.31 a line integral over the contributions of all surface current filaments along $\partial\Omega_J$:

$$\psi_{WJ} = \oint_{\partial\Omega_J} G(\boldsymbol{r}, \boldsymbol{r}^*)\mu_0\sigma(s^*)ds^* = \oint_{\partial\Omega_J} G(\boldsymbol{r}, \boldsymbol{r}^*)\left(\frac{1}{R^*}\frac{\partial\psi_{JE}}{\partial n^*}\right)ds^* \tag{3.32}$$

On $\Omega_A \setminus \Omega_J$ ψ_{JE} is equal to zero. Considering equation 3.19 this results in

$$\psi_V = -\oint_{\partial\Omega_J} G(\boldsymbol{r}, \boldsymbol{r}^*)\left(\frac{1}{R^*}\frac{\partial\psi_{JE}}{\partial n^*}\right)ds^*. \tag{3.33}$$

Once ψ_V is known the flux contribution ψ_{WA} from the ASDEX Upgrade wall can be evaluated on Ω_A

$$\begin{aligned} \triangle^*\psi_{WA} &= 0, \\ \psi_{WA} &= -\psi_V \text{ on } \partial\Omega_A \ . \end{aligned} \tag{3.34}$$

The superposition $\psi_V + \psi_{WA}$ is the desired solution on $\Omega_A \setminus \Omega_J$ with properties as described above.
The derivation above is inspired by a physical picture. A second derivation, which is more guided by mathematical considerations, is presented in appendix A.2. It uses a version of Green's second identity for the operator Δ^* derived in appendix A.1. Furthermore the approach developed above is tested on the basis of the analytical model in appendix A.3.

3.2.5 Special treatment for the passive stabilising loop

The passive stabilising loop can be regarded as an assembly without conducting connection to the rest of $\partial\Omega_A$. However for the elaboration of the function $\psi = \psi_V + \psi_{WA}$ it is assumed

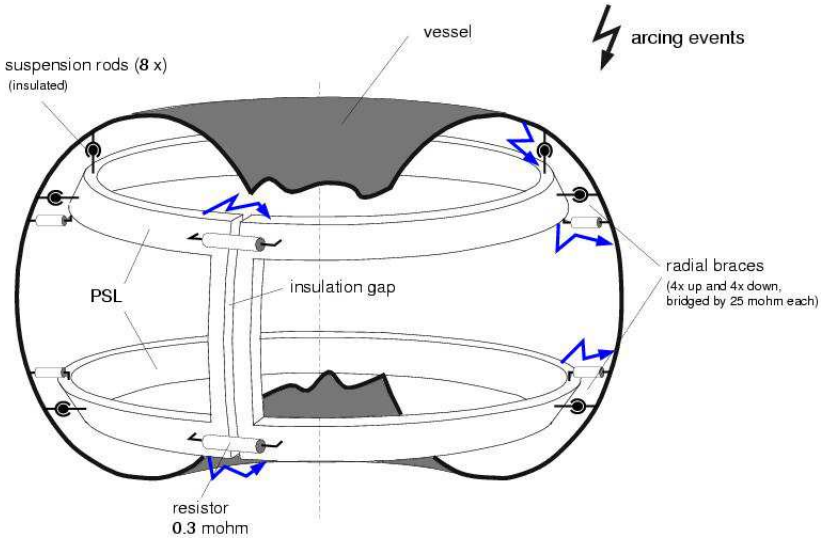

Figure 3.6: Schematic view of the passive stabilising loop

that $\psi_{\mathrm{PSL}} = \psi_{\partial\Omega_A \setminus \mathrm{PSL}} = 0$. Taking into account the missing conducting connection a correct system to solve would be

$$\begin{aligned} \triangle^* \psi &= -g(R,Z) \\ \psi &= 0 \text{ on } \partial\Omega_A \setminus \mathrm{PSL} \\ \psi &= c_{\mathrm{hom}} \text{ on PSL}, \end{aligned} \tag{3.35}$$

where c_{hom} is not fixed to 0, as it has been effectively up to this point. The equality of the flux in both branches of the PSL is justified by the fact that the branches are connected due to the saddle-like geometry of the PSL as can be seen in figure 3.6 . A solution for this system can be gained by an extension of the solution 3.21

$$\psi = \psi_{\mathrm{spe}} + c_{\mathrm{hom}} \psi_{\mathrm{hom}}, \text{ with} \tag{3.36}$$

$$\begin{array}{l|r} \triangle^* \psi_{\mathrm{spe}} = -g(R,Z) & \triangle^* \psi_{\mathrm{hom}} = 0 \\ \psi_{\mathrm{spe}} = 0 \text{ on } \partial\Omega_A \setminus \mathrm{PSL} & \psi_{\mathrm{hom}} = 0 \text{ on } \partial\Omega_A \setminus \mathrm{PSL} \\ \psi_{\mathrm{spe}} = 0 \text{ on PSL} & \psi_{\mathrm{hom}} = 1 \textit{ on } \mathrm{PSL}. \end{array}$$

To evaluate the constant c_{hom} in the superposition, the currents in the PSL for ψ_{spe} respectively ψ_{hom} are calculated. Using these and the fact that for each case they have in both PSL branches equal absolute value and opposite sign yields [7]

$$c = -\frac{I_{\mathrm{PSL},U,\mathrm{spe}} + I_{\mathrm{PSL},L,\mathrm{spe}}}{I_{\mathrm{PSL},U,\mathrm{hom}} + I_{\mathrm{PSL},L,\mathrm{hom}}}. \tag{3.37}$$

Figure 3.7 shows distributions of the poloidal flux in a tearing mode simulation described in subsection 3.2.7 for three different cases. While in (a) the PSL is not treated as a part of the boundary $\partial\Omega_A$, it is in (b) and (c). In (b) the constant c_{hom} is set to 0, which is equivalent to $\psi_{\mathrm{PSL}} = \psi_{\mathrm{vessel}}$. In (c) the constant c_{hom} is calculated by the PSL currents as detailed above. Consequently in 3.7 (c) vessel boundary and PSL appear to have less identical poloidal magnetic flux compared to the situation in figure 3.7 (b).

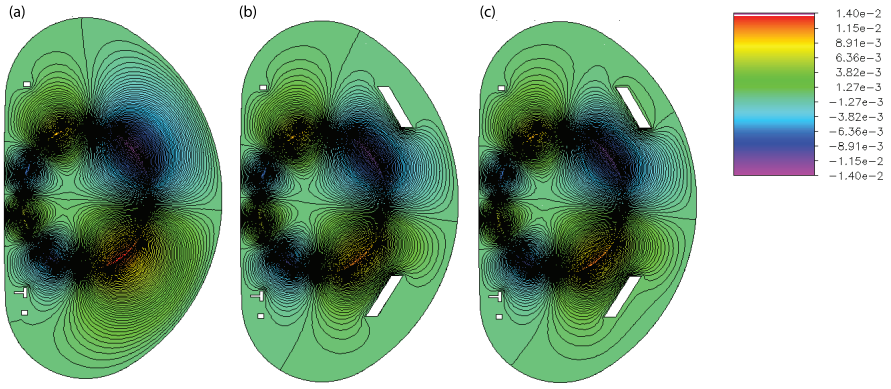

Figure 3.7: Contour of poloidal flux for a tearing mode with different treatments of the PSL: (a) PSL not regarded as a boundary (b) PSL part of $\partial\Omega_A$ with identical poloidal flux ($c_{\text{hom}} = 0$) (c) PSL part of $\partial\Omega_A$ with individual poloidal flux ($c_{\text{hom}} \neq 0$).

3.2.6 Synthetic magnetic probes

Once the flux function ψ corresponding to the realistic ASDEX Upgrade boundary is obtained as described above the last step is to convert this information by synthetic probe modules into synthetic magnetic signals. In the basic version, the synthetic magnetic probes are described as objects without extension. For all probe locations $\nabla\psi$ is evaluated. On the basis of this the magnetic field component in the direction of the probe orientation is evaluated. Time derivation leads to the synthetic signals.
Additionally a version has been developed, in which the synthetic magnetic probes are described with realistic dimensions. Here a one dimensional (two dimensional) array of points in the intersection of the probe with the analyzed poloidal plane has been created for probes measuring B_{rad} (B_{pol}).[4] In all points of these arrays the relevant field components are evaluated. The values of $\partial\psi/\partial R$ and $\partial\psi/\partial Z$ are constant on each triangle of the triangulation due to the linearity in the description of ψ. Therefore for the B_{rad}-coils the triangularization has been refined and adapted to the positions of the points in these arrays to overcome associated discretisation problems. For the summation of these field components in the case of the B_{rad}-coils a weighting has been applied, which is accounting for the spiral geometry of the circuit.

3.2.7 Validation of the synthetic magnetic diagnostic module

In order to validate the performance of the synthetic magnetic diagnostic module SYNMAG a comparison analysis has been carried out. Results from SYNMAG in the operation mode 'Play' have been cross-checked with results from the Mirnov Interpretation Code (MIC)[5] [7] and also with experimental results. A perturbation current density distribution, which is

[4]The directions within the poloidal plane perpendicular and parallel to the flux surface are denoted as *rad* and *pol*.

[5]MIC also uses PLTMG to solve the partial differential equation.

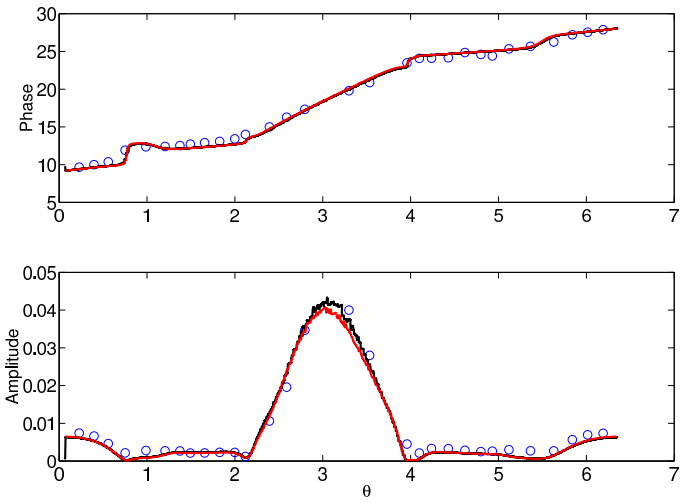

Figure 3.8: Comparison of phase and amplitude of a tearing mode (ASDEX Upgrade discharge AUG4816 at $t = 1.009$s): Experimental data (blue), data synthesized by MIC (black) and data synthesized by SYNMAG (red)

used to simulate tearing modes in [7], has been chosen:

$$j = \begin{cases} 0 & \text{for } |r - r_{q_{res}}| > w_{\text{half}} \\ I_0 \dfrac{|B_\phi|}{|B_{\text{pol}}|} \dfrac{1}{R} \sin(m\theta^* + \varphi) & \text{for } |r - r_{q_{res}}| \leq w_{\text{half}}. \end{cases} \tag{3.38}$$

As experimental reference ASDEX Upgrade discharge AUG4816 at $t = 1.009$s is chosen. This is a circular plasma with a $(m, n) = (3, 1)$ mode on the $q = 3$ surface, which is located about 1.3cm inside the LCFS. With both codes calculations for two values of the constant phase shift ($\varphi = 0$ and $\varphi = \pi/2$) are performed. For each code the amplitude and phase of the perturbation field on a loop of positions close to the ASDEX Upgrade vessel wall is synthesized. Additionally amplitude and phase of the mode in each probe of the poloidal Mirnov probe array, which is in a constant distance of about 5cm inward from this loop, is evaluated. Figure 3.8 shows phase and amplitude of the mode as a function of θ derived from the experiment and simulated by MIC and SYNMAG. There is good agreement of all three curves for both cases. Especially between the two codes there is virtually no discrepancy.

Chapter 4

Experimental arrangements and analysis tools

This chapter aims at introducing experimental possibilities and boundary conditions. Furthermore several central methods for the analysis of experimental data are introduced.

4.1 Key diagnostic systems

A significant number of diagnostics are included in the analysis of discharges performed at ASDEX Upgrade described in chapter 5. Fast sampling diagnostics are of clear advantage when it comes to resolving the time scales related to ELMs. Furthermore the perturbations associated with ELMs evolve on a time scale which is fast compared to their rotation. Hence spatial resolution is another crucial aspect. In ASDEX Upgrade and also in TCV the sets of magnetic probes are among the most advantageous diagnostics in terms of spatial and temporal resolution for the investigation of ELMs. Therefore magnetic probes constitute the central diagnostic in this thesis. Especially in the ASDEX Upgrade case, data from several other fast sampling diagnostics have been exploited and correlated to magnetic data.

ASDEX Upgrade

Figure 4.1 provides an overview of the geometry of some of the diagnostics employed in ASDEX Upgrade.

Magnetic measurements

ASDEX Upgrade is equipped with an extensive set of probes measuring the temporal derivative of magnetic field components. Among these there is a set of pick-up coils, which are designed as rectangular spirals of copper tracks printed on an insulator plate [84]. The dimensions of the volume enclosed by the windings ((radial,poloidal,toroidal): (0.1mm,100mm,100mm) and (0.1mm,50mm,100mm) respectively)[1] of these printed circuit probes allow to position them for measurements of the radial component of $\dot{\boldsymbol{B}}$, such that the

[1]The probes of the high resolution poloidal array have a lower poloidal extension compared to the other ones (compare figure 4.9).

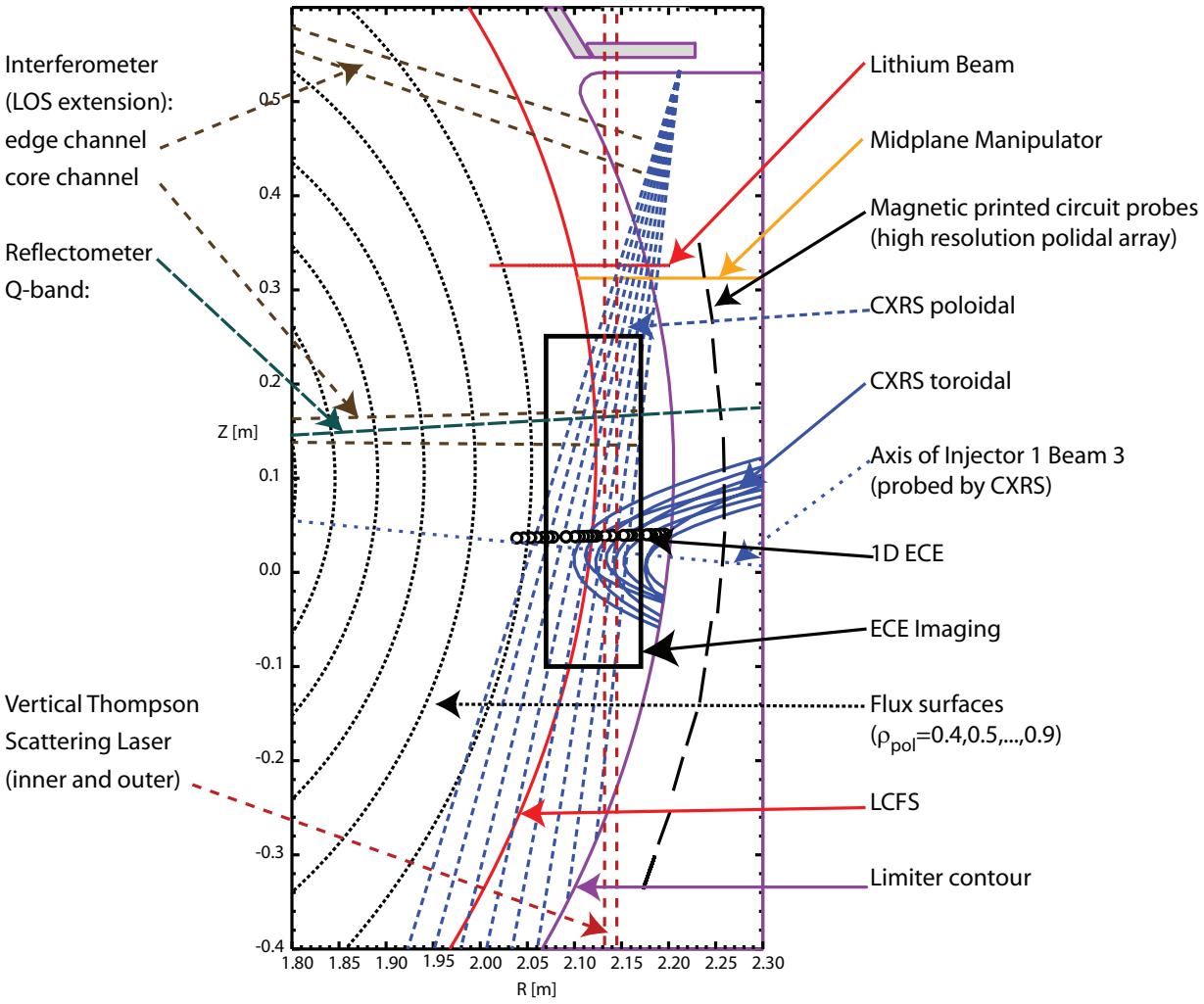

Figure 4.1: Outboard part of poloidal cross section of ASDEX Upgrade together with equilibrium and geometry of a selection of employed diagnostics.

average distance between windings and the LCFS is low ($\approx$ 10cm).[2] The poloidal positions of a high resolution array of printed circuit probes is shown in figure 4.1. The toroidal/poloidal positions of most of the printed circuit probes in ASDEX Upgrade can be seen in figure 4.9 (circles).
All printed circuit probes are connected by twisted pair cables to ADCs, where the cables are terminated by 2MΩ. The ADCs include a low pass filter (Bessel, 3dB limit frequency 512kHz). They digitize the incoming voltage U with 14bit resolution and 2MHz sampling rate. The calibration of the signals is done frequency independent by $dB/dt = -U/A_{eff}$, where A_{eff} is the effective area of the probe. In [85] the frequency dependent response of the printed circuit probes on a magnetic field produced by a Helmholtz coil has been measured (figure 4.2). The response maxima are between 150kHz and 200kHz.

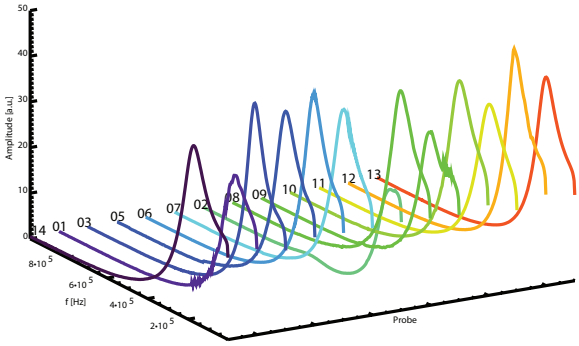

Figure 4.2: Response of printed circuit probes on a magnetic field with varying frequency and constant amplitude. Figure adapted from [85].

In addition to printed circuit probes a triple axis magnetic probe mounted on the mid plane manipulator is employed (subsection 5.3.1). This probe includes one cube of 20mm edge length (similar to the one described in [86]), on which three mutual perpendicular coils are wound. The probe measures the time derivative of the magnetic field components in the $R-$, $Z-$ and $\phi-$direction. This information in combination with equilibrium reconstruction allows to calculate the time derivative of the magnetic field components in the poloidal plane parallel (dB_{pol}/dt) and perpendicular (dB_{rad}/dt) to the flux surface.[3]
The data acquisition chain for the triple axis magnetic probe starts with a band pass filter (1kHz to 1MHz). The output signals from this are transfered to identical ADCs as in the case of the printed circuit probes.

Electron cyclotron emission spectroscopy (1D + 2D)

Electrons in a magnetically confined plasma are gyrating around magnetic field lines and therefore are emitting cyclotron radiation at a fundamental frequency and higher harmonics. The fundamental frequency for a given local magnetic field strength is distributed in a narrow frequency band.[4] As the main magnetic field component in a tokamak plasma is a function of the radial position ($B_\phi \propto 1/R$) only a small radial region is emitting at a certain frequency. In the case of an optical thick plasma the intensity distribution of this radiation can be described

[2] In the remainder of this work radial magnetic field measured with this probes at ASDEX Upgrade are referred to as B.
[3] Identical calibration for the two raw signal components parallel to the poloidal plane is assumed.
[4] The deviation from a δ-function is due to relativistic and Doppler effects.

by Planck's law. As $\hbar\omega \ll kT_e$ Rayleigh-Jeans law can be applied to infer a proportional relation between radiation intensity and electron temperature. Therefore spectroscopy of electron cyclotron emission (ECE) radiation is a standard method to measure the electron temperature.
Without wall reflections, an optical depth of $\tau > 3$ is needed to measure more than 95% of the black-body radiation. In H-mode plasmas this is usually fulfilled at locations inside the steep gradient region. In [87] a profile of the optical thickness τ has been calculated for one time in an ASDEX Upgrade H-mode plasma on the basis of the profiles of electron density and temperature. The transition ($\tau = 3$) from optical thick to thin coincides well with the location of the LCFS. For optically thin conditions solving the radiation transport equation would be necessary in order to infer reliable values of the electron temperature [88].
ASDEX Upgrade is equipped with an ECE system (1D) measuring in X2-mode (second harmonic, electric field vector perpendicular to the guiding magnetic field) in 60 locations along one radial path as illustrated in figure 4.1. This system[5] has a temporal resolution corresponding to 32kHz and a radial resolution of about 1cm. In addition to this an ECE imaging (ECEI) diagnostic [87] is installed in ASDEX Upgrade, which samples with 0.5MHz radiation temperature in X2-mode on a rectangular grid of positions located in one poloidal plane. By adjusting the probed frequencies this grid can be shifted radially. Figure 4.1 shows the boundary of this grid as it is positioned in discharge AU27082 (R = 2.07m to 2.17m, $Z = -0.10$m to 0.25m).

Gas puff imaging

The availability of fast framing cameras recording in the visual spectrum leads to improved possibilities of diagnosing structures of increased radiation (e.g. during ELMs). The situation can be further improved by appropriate gas puffing. A discussion of the question, whether the increased radiation corresponding to ELM filaments is due to density or temperature perturbations or a mixture of both, can be found in subsection 5.10.2.
In the cases presented in subsection 5.10.2 a Phantom v710 camera recording 256 x 256 pixels with a 12μs integration time and a frame rate of 79kframes/s has been used. This time resolution constitutes a compromise between collecting sufficient signal and capturing relevant time scales. To visualize radiation patterns associated with ELMs it is important to isolate events happening on corresponding time scales. Hence a dynamic background subtraction technique is applied in order to remove radiation components varying on slower time scales. From each frame the average of the set of frames starting 10 frames earlier and finishing 10 frames later has been subtracted.
Two tangential views from the same port in different horizontal directions are used (figure 4.3). Gas has been supplied from locations in the recessed wall of main chamber ports (0.5m width, 1.0m height and 1.0m depth) in three different sectors. In the experiments reported in subsection 5.10.2 two view-gas-settings detailed in table 4.1 are used.

Table 4.1: Fast camera observation setups

View-gas-setting	S_1	S_2
View	sector 13 to sector 1	sector 13 to sector 9
Gas inlet	sector 1 and sector 13	sector 9

[5]Since 2012 a system with a resolution corresponding to 1MHz is also available.

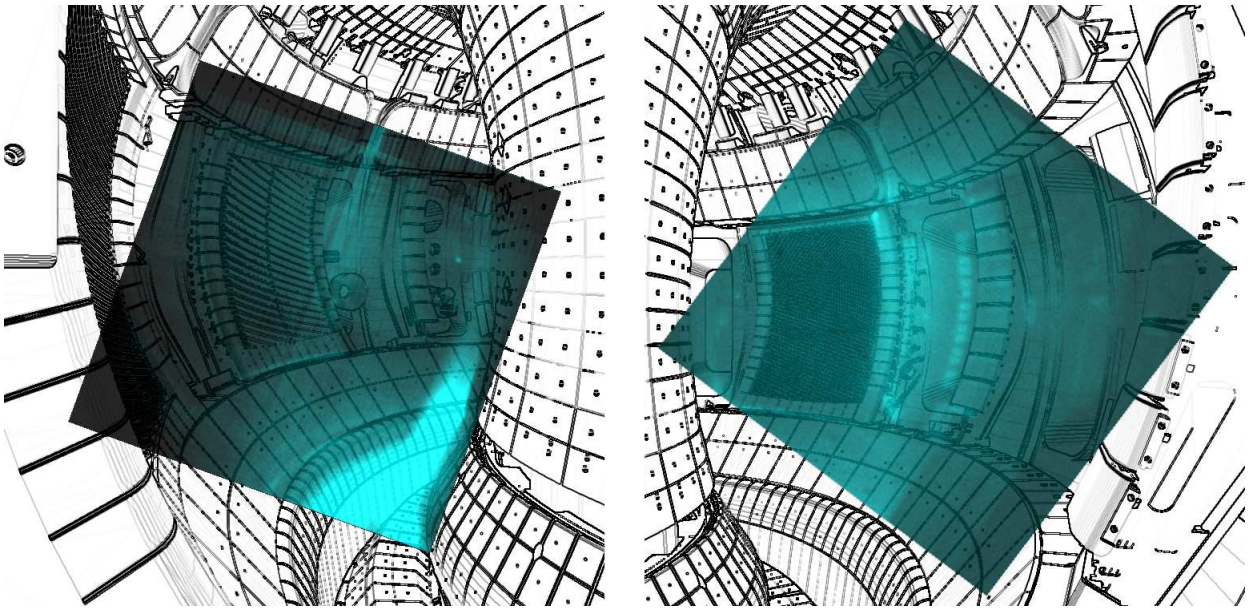

Figure 4.3: Camera views from sector 13 to sector 9 (left, view-gas-setting S_2) and from sector 13 to sector 1 (right, view-gas-setting S_1): The background images (contours) display a picture of the internal vessel structures from view point of the camera. Overlaid with some transparency are single frames recorded by the fast framing camera.

Thomson scattering

Electromagnetic waves are scattered elastically by charged particles. As the scattering cross section decreases quadratically with increasing mass, electromagnetic waves are mainly scattered by electrons. Thomson scattering is the scattering of electromagnetic radiation by free (unbound) electrons. Dependent on the the parameter $\alpha = |\boldsymbol{k}|\lambda_d$ with $\boldsymbol{k}$ as the scattering vector and λ_d as the Debye length, either single electrons ($\alpha > 1$, incoherent Thomson scattering), or plasma waves related to the plasma ions ($\alpha < 1$, coherent Thomson scattering) determine the scattering spectrum. For incoherent Thomson scattering the frequency of electromagnetic radiation scattered by a single electron is Doppler-shifted by $\Delta\omega = \boldsymbol{v} \cdot \Delta\boldsymbol{k}$, where $\boldsymbol{v}$ is the velocity vector of the electron.
For incoherent Thomson scattering the scattering spectrum contains key information on the electron population. The intensity of the total scattered radiation is directly proportional to the electron density. The width of the scattered spectrum is determined by the temperature of the electrons. If the spectrum is sufficiently resolved also current density and further information can be inferred.
The vertical Thomson scattering diagnostic at ASDEX Upgrade consists of up to six vertically launched, Nd-YAG laser beams, which are radially slightly displaced against each other (see laser path in figure 4.1). Scattered light is collected from 16 scattering volumes of 2.5cm height, which are vertically displaced by 6cm from each other. The resulting radial resolution for measurements at the plasma edge is 3mm in the steep gradient region and increases to 1.5cm around the LCFS and in the SOL [89]. Each laser fires pulses of 15ns duration and 1J energy with a repetition rate of 20Hz.

Laser interferometry

In ordinary mode (electric field vector parallel to the guiding magnetic field) for frequencies much larger than the plasma frequency ($\omega_{pe} = (n_0 e^2/m_e\epsilon_0)^{1/2}$) the difference of the refraction index in vacuum and plasma is proportional to the electron density. Splitting an electromagnetic wave into two parts and sending these along two paths of identical length, propagating through vacuum and plasma respectively, leads to a phase shift $\Delta\phi$. This phase shift is then proportional to the line integrated plasma electron density. In order to measure the temporal evolution of this phase shift, a Mach-Zehnder interferometer is frequently chosen [4]. When phase detection is done via the heterodyne principle, a frequency shifter ($\Delta\omega_0$) and subdivisions of the beam lines are introduced, to obtain finally two signals oscillating with $\Delta\omega_0$ and shifted in phase against each other by $\Delta\phi$.
The time resolution of such a system is limited by $\Delta\omega_0$. For the DCN laser interferometer at ASDEX Upgrade $\Delta\omega_0$ is 10kHz, which is equal to the sampling rate of the system. Other limitations are posed by the history dependent nature of the measurement. So called *fringe jumps* are errors in the measurement of $\Delta\phi$ resulting from counting errors by integer multiples of 2π. They appear, if the laser beam passes strong density gradients (e.g. due to injected deuterium ice pellets, ELMs or sawtooth crashes) leading to deflection and/or widening of the beam. As a consequence the laser intensity exiting the plasma is too low for a reliable reconstruction of $\Delta\phi$. Furthermore fast density evolutions can lead to similar erratic behavior. The line of sight of the core and edge channel of the ASDEX Upgrade DCN laser interferometry system is illustrated in figure 4.1.

Lithium beam impact excitation spectroscopy

In this diagnostic, high energetic lithium ions are accelerated, neutralized and injected into the plasma. The lithium atoms can either be excited due to collisions with plasma particles or ionized. Taking into account the lifetime in the excited state leads to a system of coupled differential equations describing the number of lithium atoms in several states as a function of a coordinate along the beam line [90]. This excitation profile is closely connected to the measured emission profile (2p-2s), which in the plasma edge has a minor dependence on the electron temperature but a strong dependence on the electron density. Therefore from the radial deexcitation emission profiles electron density profiles at the plasma edge can be inferred.
Until $\approx$ 2008 for the analysis of lithium beam data at ASDEX Upgrade an iterative method solving numerically for the density as a function of the radial position has been used [91]. Now lithium beam data are exclusively analyzed employing integrated data analysis [92] (i.e. applying Bayesian theory, see below). Advantages of this approach are a more accurate error estimate, an extension of the investigated region radially inwards, that the method works as well at lower density plasmas and a significantly improved temporal resolution ($\geq 50\mu$s). The geometry of the lithium beam at ASDEX Upgrade is shown in figure 4.1.

Charge exchange recombination spectroscopy

Neutral deuterium atoms injected into the plasma collide with impurity ions leading to charge exchange reactions: $A^{Z+} + D^0 \rightarrow (A^{(Z-1)+})^* + D^+$. The spectrum emitted from the recombined ions, which are born in an excited state, is analyzed. The impurity temperature and their velocity component parallel to the line of sight can be deduced from the Doppler

width and shift of this spectrum. The amount of deuterium atoms with relevant velocities is significantly higher in the volume of neutral beam injection compared to the rest of the plasma. The intersection of this beam with the lines of sight constitutes relatively localized measurement volumes. In principle the measured spectra include also line integrated passive components from electron excitation, recombination and thermal charge exchange. However at the plasma edge the active component is dominant.
The lines of sight of the poloidal and toroidal edge charge exchange recombination spectroscopy (CXRS) systems in ASDEX Upgrade and also the central axis of the neutral beam they are directed at are illustrated in figure 4.1. The radial distance of lines of sight is 10mm. However by application of radial plasma sweeping the radial resolution can be reduced down to 3mm for the toroidal system and 5mm for the poloidal system respectively. The sampling rate of the system is 0.45kHz [93].
The combination of measurements of the poloidal and toroidal flow velocity of the impurities and their pressure gradient allows the derivation of profiles of the radial electric field

$$E_R = \frac{1}{n_\alpha Z_\alpha e}\frac{\partial p_\alpha}{\partial r} - v_{\theta,\alpha}B_\phi + v_{\phi,\alpha}B_{\mathrm{pol}}, \tag{4.1}$$

where Z_α denotes the charge state of the species α. The impurity pressure gradient $\partial p_\alpha/\partial r$ is calculated from profiles of impurity temperature and density, which is also measured by the CXRS system. In section 5.6 E_R will be used to calculate the velocity $v_{E\times B}$ corresponding to the $E \times B$-drift.

Reflectometry

In a reflectometry system a microwave or mm-wave beam with a frequency $f_0 = \omega/2\pi$ is launched into the plasma and reflected when the refractive index approaches zero (cutoff condition). For O-mode polarization (electric field vector parallel to the guiding magnetic field), which is used in this work, the cutoff condition is $\omega = \omega_{pe}$. The radial position of the density cutoff layer may be determined using density profiles from other diagnostics. The phase shift of the incident and reflected waves is sensitive to the radial displacement of the density cutoff layer.
In this work, a frequency hopping reflectometer dedicated to density fluctuation measurements has been used [94]. A specified launch frequency pattern is pre-programmed and repeated continuously throughout a single plasma discharge. The probe frequency is held constant during typically 6-15ms and the switching time to another frequency is around 1ms. This reflectometer is composed of two frequency bands, Q (33-49.2GHz) and V (49.4-72GHz) covering the density range $1.35 - 6.10^{19}\mathrm{m}^{-3}$. The Q and V bands antenna are located in the outboard side of ASDEX Upgrade (figure 4.1). The sampling rate of the system is 2MHz.

Divertor diagnostics

To study the timing of effects at the divertor due to ELMs measurements of the divertor current $I_{\mathrm{pol,sol,out}}$ are regarded. This current has a strong rise in absolute value correlated to the onset of the ELM. The measurements are taken at four (three for discharges AUG23221, AUG24059, AUG25764) shunts connected to outer divertor tiles with identical toroidal, but different poloidal positions (figure 4.4). The dominant current component is measured at the lowest tile. The measurements are sampled with a rate of 100kHz.
Further information on the divertor is obtained by collecting light. With a wide angle lens

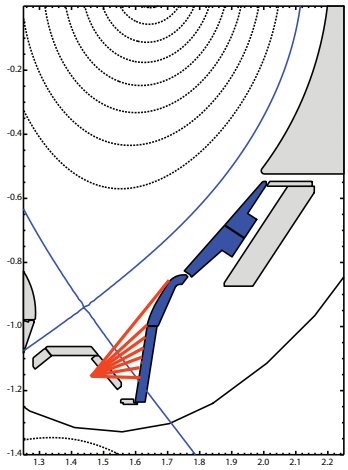

Figure 4.4: Outer divertor of ASDEX Upgrade in poloidal cross section. The divertor tiles, through which a part of the measured divertor current is flowing are displayed in blue. The poloidal projection of the view of the D_α-diagnostic is illustrated in red.

an area of the outer divertor in sector 11 is observed from below the roof-baffle in sector 7 (figure 4.4). The collected light is D_α-filtered and its total intensity is sampled at 40kHz.

Integrated data analysis

Integrated data analysis (IDA) is a powerful tool to enhance the information that can be gained by a single diagnostic system or a set of diagnostic systems [95]. Based on Bayesian statistics and measurement data, it infers plasma conditions, for which such a measurement is most probable. This is done considering a forward model of the measurement. Measurement uncertainties are regarded as well as prior informations (e.g. that a certain parameter has positive sign). At ASDEX Upgrade electron density and temperature profiles are routinely calculated using IDA.

TCV

Magnetic measurements

TCV is equipped with an extensive set of magnetic probes [96], which are mounted between the wall and graphite protection tiles inside the vacuum vessel. The probes measure the component of the time derivative of the magnetic field, which is tangential to this wall in the poloidal plane. The transfer functions of the probes and also all elements of the amplifying chain have been well characterized and fully regarded by a frequency dependent calibration. 12-bit ADCs are used. For the investigated discharge TCV42062 the sampling rate has been set to 250kHz.
There are toroidal arrays of magnetic probes in three vertical positions consisting of 16 (8) equidistant probes on the outboard side (inboard side). In TCV42062 the upper toroidal coil sets with positions corresponding to probe numbers 17 (outboard) and 4 (inboard) in figure 4.5 have been used. Therefore the measured directions for these probes are in good agreement with the poloidal direction.[6]

[6]In the remainder of this work for TCV measured magnetic field into this direction is referred to as B.

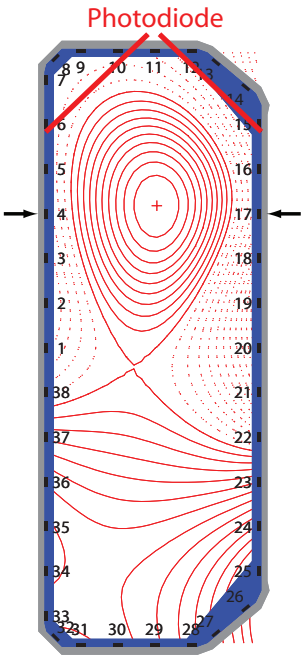

Figure 4.5: Poloidal cross section of TCV including vacuum vessel (gray), tile aperture (blue), positions of magnetic probes of the poloidal array (black) and contours of the poloidal flux (red) for discharge 42062 at 0.7s. The wide angle view of the optics connected to the photo diode is indicated by two lines.

D_α-radiation measurement

D_α-radiation is measured by a photo diode. It is connected to wide angle optics with a view from the top of TCV as indicated in figure 4.5. Hence the collected light can originate from the main plasma, the outer and inner wall and the divertor region. The signal is sampled with a rate of 50kHz.

4.2 Investigated discharges

Several H-mode discharges performed in ASDEX Upgrade and TCV are analyzed in detail in the context of this work.

ASDEX Upgrade

Table 4.2 summarizes a number of plasma parameters of the ASDEX Upgrade discharges that are analyzed in detail or used as input for JOREK simulations (AUG23221). The abbreviations in table 4.2 correspond to (#) number of the discharge, (Δt) time interval of flat top phase used for data analysis, (Conf) configuration (LSN / USN: lower single null / upper single null), (I_P) plasma current, (B_ϕ) toroidal magnetic field, (δ_{up} and δ_{low}) upper and lower triangularity at the LCFS, (q_{95}) safety factor at the surface of 95% of the poloidal magnetic flux at the LCFS, (W_{mhd}) plasma stored energy obtained from equilibrium reconstruction, (n_{edge}) line averaged density from interferometry edge channel, (P_{NBI}) neutral beam input power, (P_{ICRH}) ion cyclotron resonance heating input power, (P_{ECRH}) electron cyclotron resonance heating input power and (ELMs) ELM type. All quantities are averaged

Table 4.2: Overview of the main parameters of the ASDEX Upgrade discharges analyzed or used as input for JOREK simulations

#	Δt [s]	Conf	I_P [MA]	B_ϕ [T]	δ_{up} [1]	δ_{low} [1]	q_{95} [1]	W_{mhd} [MJ]	n_{edge} [$10^{19}\mathrm{m}^{-3}$]	P_{NBI} [MW]	P_{ICRH} [MW]	P_{ECRH} [MW]	ELMs
23221	4.6 - 4.8	LSN	1.0	-2.5	0.10	0.40	-4.8	0.63	6.6	7.5	1.2	1.3	I
24059	3.7 - 3.8	LSN	1.0	-2.5	0.09	0.38	-4.7	0.48	7.1	4.8	1.2	0	I(?)
25764	1.6 - 1.9	LSN	1.0	-2.4	0.10	0.42	-4.4	0.86	5.3	7.5	0	0.9	I
26299	1.8 - 2.8	LSN	1.0	-2.5	0.05	0.44	-4.0	0.63	6.8	7.4	0	0.9	I
26324	2.5 - 3.5	LSN	1.0	-2.5	0.26	0.48	-4.4	0.77	7.3	7.7	0	0.8	I
26510	1.4 - 1.5	LSN	0.8	-2.0	0.09	0.39	-4.3	0.39	6.7	4.8	0	0	I
26703	2.3 - 2.4	USN	1.0	-2.5	0.34	0.15	-4.2	0.62	10.5	7.4	0	0.8	I
26704	1.7 - 1.8	USN	1.0	2.5	0.38	0.18	4.4	0.86	7.2	7.3	0	0.8	I
26764	4.0 - 5.0	LSN	0.8	-2.4	0.04	0.45	-5.3	0.52	4.2	5.4	0	0.9	I(?)
27082	2.3 - 2.4	LSN	1.0	-2.5	0.09	0.36	-4.6	0.55	7.0	4.9	0	2.1	I(?)
27112	1.9 - 2.0	LSN	1.0	-2.4	0.07	0.35	-4.3	0.47	7.3	4.4	0	0	I
27242	1.4 - 1.8	LSN	0.8	-2.4	0.03	0.44	-5.2	0.44	4.1	4.9	0	0	I

over the relevant time interval.
For all time intervals listed it is attempted to determine, if the ELMs are of type I. Among a number of key plasma parameters the main feature regarded is the scaling of ELM frequency with P_{sep}. In most cases there is a clear indication of type I ELMs ($dP_{\mathrm{sep}}/df_{\mathrm{ELM}}>0$). In three cases there are also indications of a type I character, however a definite determination of the ELM type is not achieved.
For discharge AUG25764, which is the most intensely analyzed ASDEX Upgrade discharge in this work, there is a clear indication. While increasing (decreasing) the input power in this discharge the ELM frequency increases (decreases). In addition, during the investigated phase the discharge is heated with 7.5MW by neutral beam injection, which is significantly further above the typical L-H-threshold for the parameters of this discharge ($P_{LH} \approx 1.6$MW [97]) than type III ELMs are usually observed. Furthermore it is possible to clearly discriminate between ELM event and inter-ELM phase, which is usually not the case for type II ELMs. On the basis of these observations and the criteria given in [28] it is inferred that the ELMs in discharge AUG25764 are of type I.

TCV

The analysis also includes one discharge performed in the experiment TCV. Discharge TCV42062 is performed in a diverted lower single null configuration [98]. Key parameters are: Plasma current 300kA, magnetic field on magnetic axis 1.43T, safety factor at 95% poloidal flux 2.3, central (pedestal top) electron density $5 \times 10^{19}\mathrm{m}^{-3}(3.8 \times 10^{19}\mathrm{m}^{-3})$, central (pedestal top) electron temperature 2.5keV (0.5keV). The discharge is heated with 135kW Ohmic power, 900kW ECRH power (X3) launched from the top of the vacuum vessel and 520kW ECRH power (X2) launched from the low field side in the X-point vicinity. In a similar discharge (TCV42547) an increase in X2 input power leads to an increase in ELM frequency, documenting the type I character of these ELMs [98].

4.3 ELM time marker

For the comparison of different ELMs it is beneficial to mark for each ELM a time of a certain characteristic event. To identify such a time some facts about the ELM evolution are reviewed.

ELMs are known to be associated with drops of typical plasma parameters like electron temperature [28] and density [39] on the pedestal top and plasma stored energy. Under certain conditions related to the detachment state [47] the D_α-radiation in the outer divertor shows a strong increase at the same time. Correlated to these processes, the current in the outer divertor $I_{\mathrm{pol,sol,out}}$ has a strong rise in absolute value [40]. As this current can be acquired easily with high temporal resolution, it constitutes a good diagnostic to generate ELM time markers on a regular basis. For each discharge analyzed the start times $t_{\mathrm{I,div,ons}}$ of the rise of $|I_{\mathrm{pol,sol,out}}|$ is identified.[7]

To characterize the basic evolution of a typical ELM the coherent ELM averages of a number of quantities are calculated. Electron temperature and density profiles are obtained via integrated data analysis from electron cyclotron emission spectroscopy and lithium beam diagnostic in combination with interferometry. The IDA values at $\rho_{\mathrm{pol}} = 0.95$ (pedestal top) are used. The plasma stored energy is obtained from equilibrium reconstruction with 0.1ms time resolution.[8]

In discharge AUG26764 from 4.0s to 5.0s 71 ELMs are found. For each of the quantities time traces during all ELMs are aligned with respect to $t_{\mathrm{I,div,ons}}$ and offset by an average over an initial phase of the investigated time interval. For each time step averages and standard deviations are calculated. Figures 4.6(a) and (b) show these averages (thick lines) and the intervals of one standard deviation around them (thin lines). Figure 4.6(c) shows for a single ELM all quantities and additionally the time derivative of the radial magnetic field, which is not suited for coherent averaging.

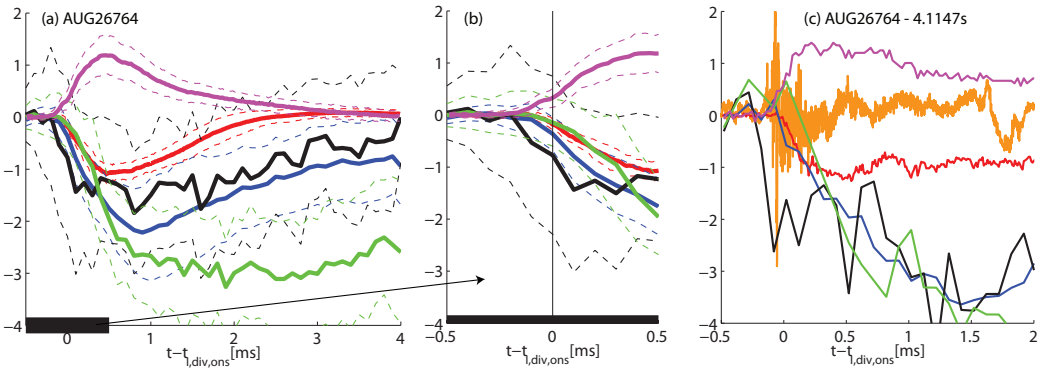

Figure 4.6: (a) Average evolution of scaled (factors in square brackets) and offset plasma quantities during ELMs in discharge AUG26764 from 4.0 to 5.0s (bold lines): Current to the outer divertor [10^4 A] (red), electron temperature at $\rho_{\mathrm{pol}} = 0.95$ [100eV] (blue), electron density at $\rho_{\mathrm{pol}} = 0.95$ [$5 \times 10^{18}\mathrm{m}^{-3}$] (black), plasma stored energy [10^4 J] (green) and D_α radiation in the outer divertor [a.u.] (magenta). Dashed lines indicate intervals of one standard deviation. (b) Close up of (a) for an interval of 1ms around $t_{\mathrm{I,div,ons}}$. (c) Evolution of the same quantities plus time derivative of the radial magnetic field [10T/s] (orange) measured at a position in the vicinity of ECE and Lithium Beam measurements for a single ELM.

[7] An algorithm has been used that detects, after subtraction of a pre-ELM average, a time in the rise phase corresponding to $5 - 25\%$ of the peak value.

[8] For non-circular plasmas integral quantities like W_{mhd} are well recoverable by equilibrium reconstruction [99]. However, during the most transient phase for about 50μs to 100μs the exact values of W_{mhd} should be treated with care. In this analysis the focus is on the timing and the dynamics of the onset of the W_{mhd} reduction. This information is considered to be robust.

It is important to note that the scatter of the $I_{\mathrm{pol,sol,out}}$ trajectories is relatively minor, even though the associated measurements are carried out at one toroidal position. Furthermore one can see that the rise of $|I_{\mathrm{pol,sol,out}}|$ begins about at the same time as

- the drop of electron temperature at the pedestal top,
- the drop of electron density at the pedestal top,[9]
- the drop in plasma stored energy and
- the onset of D_α-radiation.

In summary $t_{\mathrm{I,div,ons}}$ yielded from $I_{\mathrm{pol,sol,out}}$ is a suitable marker ($\pm 100\mu$s) for the onset of pedestal erosion due to ELMs.
For TCV the time $t_{\mathrm{D}\alpha\mathrm{,ons}}$ of the onset of D_α-radiation is used as ELM time marker. It has to be noted that the diagnostic employed for this partly views the main chamber.

4.4 Frequency band selection

The typical ELM signature from pickup coils measuring the radial magnetic field at ASDEX Upgrade is broadband extending from a few kHz to several hundreds of kHz. Figure 4.7(a) shows the decomposition of such a signal into high and low frequency components. To isolate the low frequency component a 10^{th} order Chebyshev Filter ($f_{\mathrm{pass}} = 60$kHz, $f_{\mathrm{stop}} = 100$kHz) is applied. This low frequency component is subtracted from the original signal to obtain the high frequency component.
The high frequency component usually shows a very fast rise close to a prompt onset. This is frequently followed by a decay with an exponential-like envelope. Particularly in the decay phase, high and low frequency components can exhibit quite different dynamics. In the example illustrated in figure 4.7(a) the low frequency component still has relatively high excursions, while the high frequency part has decayed to a level significantly below the peak level. Figure 4.7(b) shows the squared modulus of the Fourier transform of the original signal for the time interval indicated in figure 4.7(a), which is proportional to the power spectral density. This distribution shows highest values for frequencies lower than 50kHz and a clear decay from 80 to 100kHz. Based on these observations it is assumed that the high and low frequency components are the footprint of at least two different physical processes, which may well be strongly linked.
The focus of this analysis is on ELM associated plasma edge phenomena. Analyzing temperature and density measurements obtained by Thomson scattering typically 10 to 20 blobs per full toroidal rotation are found [100]. In another study structures observed by infrared thermography in the divertor have been mapped back to the mid plane and extrapolated to 8 to 20 peaks per toroidal rotation [49]. Both ranges agree with the corresponding values for filaments observed by gas puff imaging in this work (subsection 5.10.2). Linear MHD stability analysis finds similar upper limits for the mode number of the most unstable components in peeling-ballooning modes [101]. Recent non-linear gyrofluid simulations [102] suggest that ion temperature gradient driven micro instabilities may also be involved in the mechanism of the ELM. Although this would involve smaller scales ($n \approx 30 - 100$), these are not in the focus of this study, as it is assumed that ELMs are initially driven by MHD (chapter 2). A frequency of 6kHz, as derived from measurements (section 5.6), is used as an upper limit for the plasma toroidal rotation frequency. This limits the frequency, with

[9] The apparent delay of the onset of electron temperature with respect to electron density is doubtful due to the relatively large standard deviation for the density.

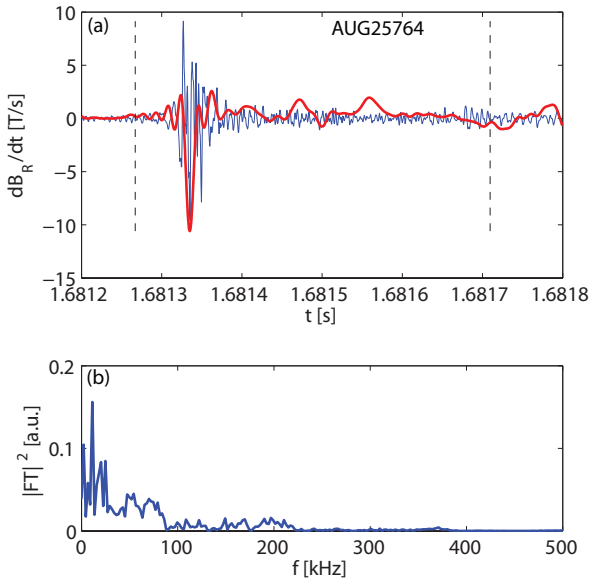

Figure 4.7: (a) Decomposition of signal of the time derivative of the radial magnetic field during an ELM in discharge AUG25764 in a high (blue) and low (red) frequency component. (b) Squared modulus of the Fourier transformed of the original signal for the time interval confined by the vertical dashed lines in (a).

which the features of interest are expected to pass the probes, to below 120kHz. On the basis of these considerations, and in order to simplify tracking of these features over several adjacent diagnostic channels, the low pass filter described above is used for the analysis of data recorded with high time resolution.

4.5 Diagnostic mapping

As described above various diagnostics are available at ASDEX Upgrade, which are capable of temporally resolving ELM associated processes. However these measurements are probing the plasma at an extensive variety of toroidal, poloidal and radial positions. Additionally, some measurements are volume integrated, some are line integrated and some are well localized.
An accurate approach to correlate different signals recorded during ELMs must take into account these different measurement positions. Therefore a method of mapping measurement positions to a common reference surface has been developed. This is done based on the assumption, that for the investigated structures the parallel wave number is so small that plasma parameters, like density or temperature, do not change significantly along a field line on the magnetic low field side.
Each diagnostic is identified with a certain diagnostic reference point, which can be regarded as the center of the intersection of the probed area with the area of existence of the investigated feature (figure 4.8(a)). For instance, for a magnetic probe measurement of a certain feature located in the steep gradient region, the diagnostic reference point can be chosen as the intersection of the shortest connection of the probe and the magnetic axis with an appropriate plasma edge flux surface (figure 4.8(a)). In an advanced version of diagnostic

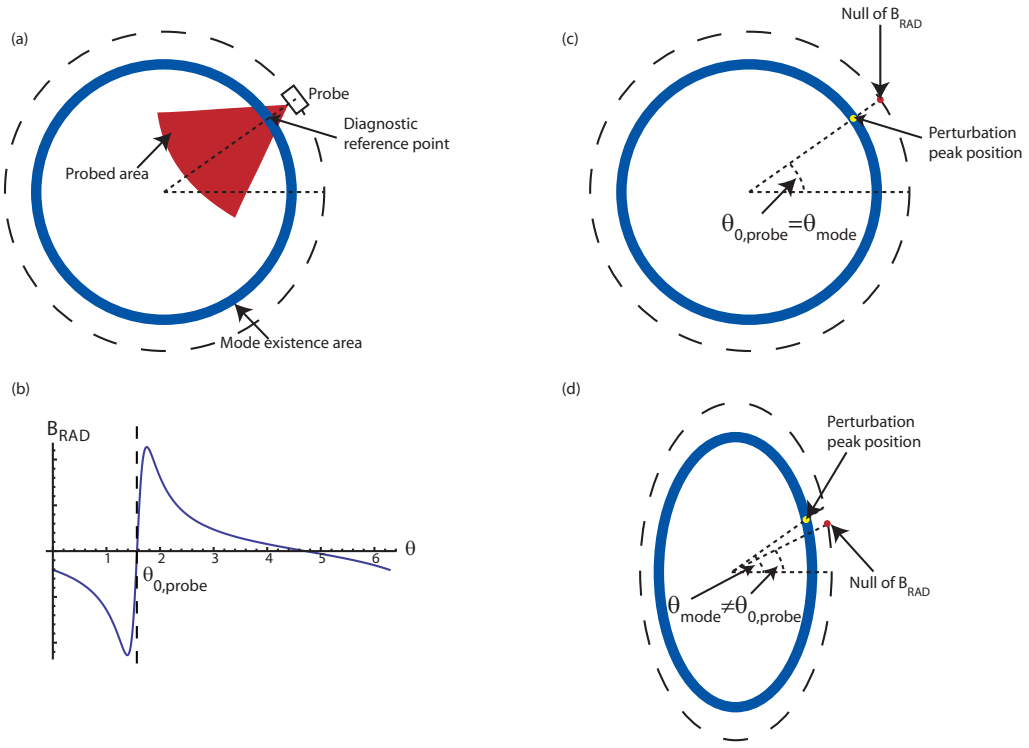

Figure 4.8: (a) Schematic view of a circular poloidal cross section: The diagnostic reference point is the center of the intersection of the mode existence area and the probed area. (b) Radial magnetic field as a function of θ for the geometry illustrated in (c). (c) Definition of poloidal angles $\theta_{0,\mathrm{probe}}$ and θ_{mode}. (d) Schematic view of an elongated cross section displaying a situation with $\theta_{0,\mathrm{probe}} \neq \theta_{\mathrm{mode}}$.

mapping this approach is refined as detailed below.
From these reference points field lines are traced to a common reference surface. This surface can be a poloidal cross-section ($\phi = \mathrm{const}$) or a surface of constant poloidal angle. In this work field lines are traced from the reference point to the outer mid plane ($\theta = 0$). This particular approach can be applied to reference points inside and outside the LCFS. Figure 4.9 shows the mapping trajectories of two poloidal and one toroidal arrays of probes measuring the time derivative of the radial magnetic field component. In the following the toroidal angle of the end points (diamonds) will be called *toroidal mapping target angle* ϕ_{map}.
For the analysis of magnetic perturbations during ELMs this approach essentially reduces from three spatial dimensions to one spatial dimension expressed in ϕ_{map} by two assumptions:

- The investigated perturbation is at a certain radial position.
- For the investigated structures, the parallel wave number is small.

In this work, the first assumption is that the perturbation is at or inside the LCFS. This is justified in section 5.6. Due to the very limited local magnetic shear at the outboard side the method is not very sensitive to the choice made here. The second assumption implies that plasma parameters, like density or temperature, do not change significantly along a field line on the magnetic low field side. This assumption will be justified qualitatively in section 5.1.

To motivate the advanced version of diagnostic mapping a screw-pinch in straight cylinder geometry, as illustrated in figure 4.8(a), is considered. The current perturbation shall be a

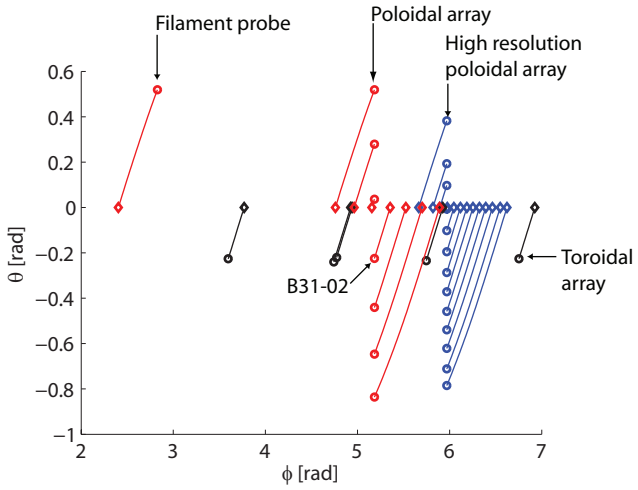

Figure 4.9: Trajectories of diagnostic mapping procedure for probes measuring time derivative of the radial magnetic field in discharge AUG25764 at 1.757s from diagnostic reference point (circles) to mapping target point (diamonds). The flux surface with $\rho_{\mathrm{pol}} = 0.95$ has been used.

single field aligned current filament. At the investigated time and z-position the peak of this filament at the poloidal angle θ_{mode} shall be at the diagnostic reference point. The radial magnetic field at the radius of a probe has a typical dependence on the poloidal angle with two nulls (figure 4.8(b)). The poloidal position of the null with the higher $|dB_{\mathrm{rad}}/d\theta|$ is called $\theta_{0,\mathrm{probe}}$. As shown in figure 4.8(c) in cylindrical geometry it is:[10]

$$\theta_{0,\mathrm{probe}} = \theta_{\mathrm{mode}} \tag{4.2}$$

ASDEX Upgrade has toroidal geometry with non-circular flux surfaces. Furthermore a number of conducting structures (e.g. passive stabilising loop) are close to the plasma. These conditions cause the equilibrium surfaces of poloidal magnetic flux to be deformed. To study the effect of these deviations from the cylindrical geometry simulations of the effect of current perturbations around one radial position with the synthetic magnetic module SYNMAG have been carried out. Current perturbations corresponding to a mode structure and also to current filaments have been used [103]. This has shown that under these more realistic conditions equation 4.2 is not fulfilled anymore. A part of this deviation is clearly related to the presence of conducting structures. It has been found that $d\theta_{0,\mathrm{probe}}/d\theta_{\mathrm{mode}}$ is a constant, which is diverging from unity towards lower values (figure 4.8(d)). For filament-like current perturbations $d\theta_{0,\mathrm{probe}}/d\theta_{\mathrm{mode}}$ scales with $1/\sigma$ and ρ_{pol}, where σ is the width of the current perturbation and ρ_{pol} is its radial location.
In the analysis presented in chapter 5, application of the standard version of diagnostic mapping (i.e. assuming equation 4.2) is mostly appropriate. However the standard version is connected to slight errors on ϕ_{map}. In one case it is beneficial to apply the advanced version (section 5.7).

[10] This is in agreement with the cylindrical model derived in section 3.1.

Chapter 5

Experimental observation of magnetic perturbations during ELMs in ASDEX Upgrade and TCV

This chapter has a focus on the main findings obtained in the experiments ASDEX Upgrade and TCV in the course of the work presented.
Perturbations of the poloidal and radial magnetic field during ELMs significantly exceeding the inter-ELM level are regularly observed in tokamak H-mode discharges. At ASDEX Upgrade the magnetic signature has a high level of variation from ELM to ELM. To demonstrate this the trajectories of the time derivative of the radial magnetic field during 20 ELMs in discharge AUG25764 are illustrated in figure 5.1. Discharge AUG25764 is characterized by a very high electron temperature[1] and low to moderate edge density. During all ELMs displayed the fluctuation level is above the inter-ELM level for 0.5ms or longer. For some of the ELMs single peaks and dips clearly dominating all others can be observed. These appear mostly short before $t_{\mathrm{I,div,ons}}$.
In order to characterize the features of a 'typical' ELM coherent ELM averaging is applied. Due to the fluctuating character of the investigated perturbations averaging over the time derivative of the radial magnetic field itself does not lead to a meaningful result. Instead of this coherent ELM averaging is applied to the RMS values of the time derivative of the radial magnetic field close to the outer mid plane (figure 5.2). On the basis of the RMS evolution the magnetic perturbation observed by a single probe can be separated into three typical components:

- **Background activity on the inter-ELM level** (blue dashed line in figure 5.2)
- **Enhanced activity correlated to the ELM** lasting for about 1ms (indicated by a red dashed line in figure 5.2): This contains the signature of a number of individual peaks / dips, which appear after $t_{\mathrm{I,div,ons}}$.
- **Dominant magnetic perturbations**[2] around $t_{\mathrm{I,div,ons}} - 0.1$ms (remaining component in figure 5.2): Only a subset of ELMs contribute significantly to this component with a low number of dominant magnetic excursions. For instance in figure 5.1(b) the main peaks and dips belong to this component.

[1] While the core electron temperature in the standard H-mode discharges in ASDEX Upgrade is usually below 3keV it is around 5keV for discharge AUG25764.

[2] In the remainder of the thesis the term *dominant magnetic perturbations* is quoted frequently. If only a single peak or dip of such a perturbation is referred to, the term *dominant magnetic excursion* is used.

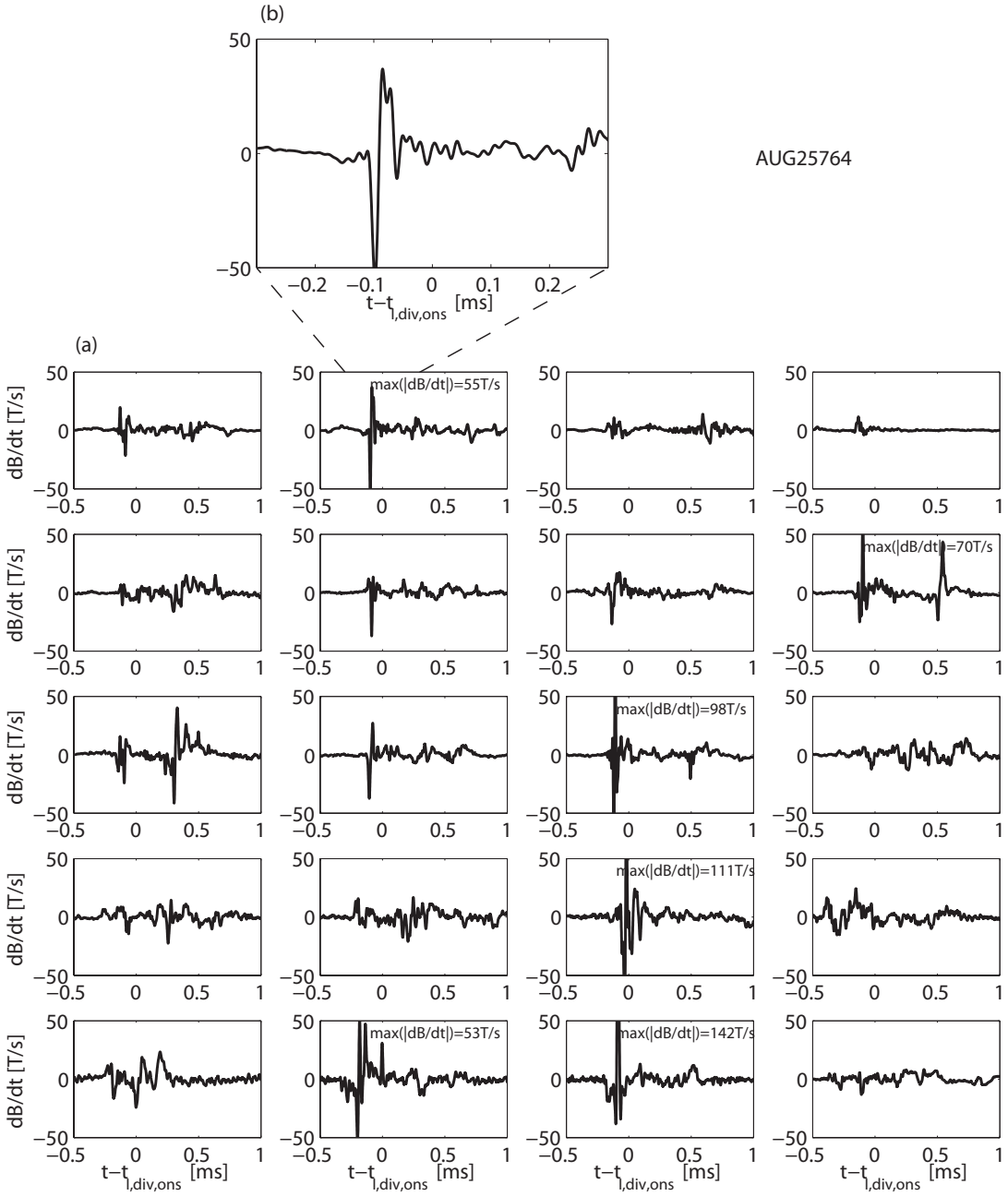

Figure 5.1: (a) Time derivative of the radial magnetic field acquired by a probe close to the outer mid plane (B31-22) for 20 ELMs in discharge AUG25764 (1 to 3s): Only ELMs with dominant inter-ELM mode activity have been disregarded. In cases where the maximum absolute value is exceeding the range displayed it is noted in the picture. (b) Close up for the second ELM.

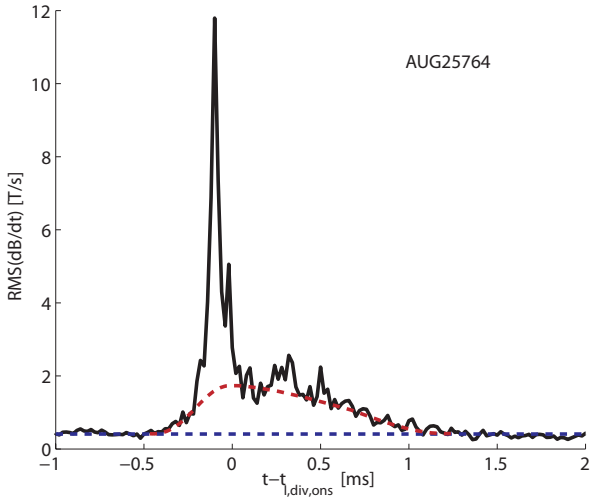

Figure 5.2: Evolution of RMS of the magnetic perturbations acquired by a probe close to the outer mid plane (B31-22) for a typical ELM in discharge AUG25764 (1 to 3s): For each ELM RMS is evaluated for boxes of 20μs duration. The resulting RMS evolution is coherently averaged over 20 ELMs, where the time $t_{\mathrm{I,div,ons}}$ serves as a reference time for the temporal alignment. The subset of ELMs regarded is the same as displayed in figure 5.1. The blue dashed line shows the inter-ELM average. The red dashed line has been drawn manually.

Besides ELMs, various other H-mode edge instabilities have been reported to show a characteristic signature recorded by magnetic probes. On certain magnetic probes the signatures of the edge snake [104], the palm tree mode [105] and the outer mode [106] diverge from a sine. They may rather be characterized by phases of constant signal, periodically interrupted by sets of a low number of dominant excursions lasting in total 0.1ms or less comparable to the ones in figure 5.1 (b).
In the remainder of this chapter magnetic perturbations during ELMs at ASDEX Upgrade and TCV are investigated. The focus of this investigation is on dominant magnetic perturbations during the early ELM phase. In the case of TCV ELMs no pre-selection in addition to the selection of the discharge (section 4.2) is applied. The magnetic diagnostic setup makes it possible to process all ELMs appearing in the selected discharge. Contrary to that for ASDEX Upgrade mainly ELMs with a low number of strong dominant excursions are investigated. This category of ELMs is of special interest, due to the similarities to the other H-mode plasma edge instabilities quoted above. Also, single dominant magnetic excursions in these ELMs have a clearer signature, which is a necessary condition for the performance of certain types of analysis.

5.1 Peak and dip trajectories

ASDEX Upgrade

In order to obtain for the ASDEX Upgrade case detailed information on the spatial structure of the current perturbation causing the dominant magnetic perturbations and their evolution diagnostic mapping as introduced in section 4.5 is applied. Figure 5.3(a) shows signals from various pick up coils measuring the radial magnetic field fluctuations during an ELM in

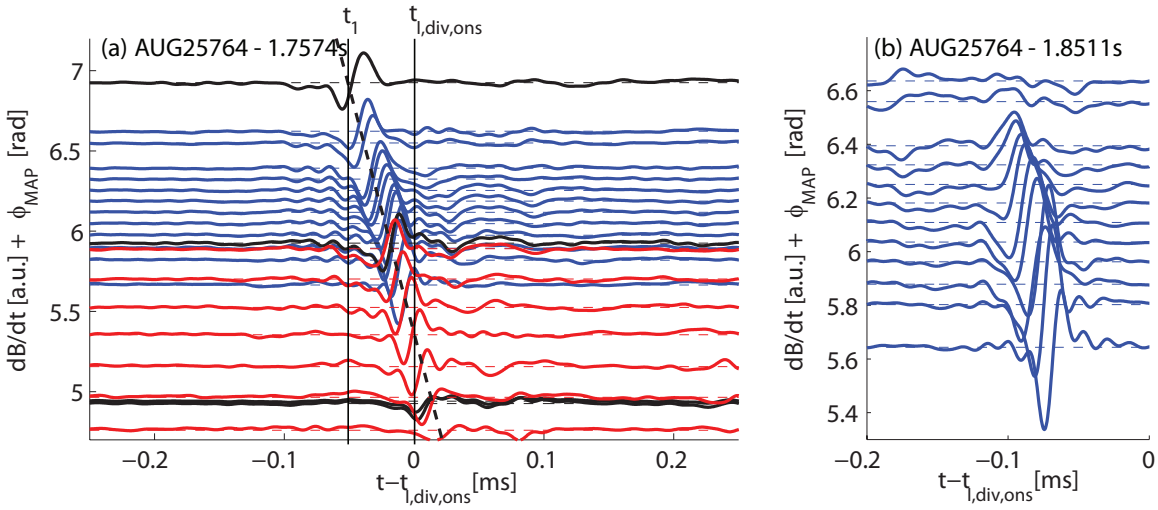

Figure 5.3: Time derivative of the radial magnetic field measured by various pick up coils (color code indicated in figure 4.9) displaced by the toroidal mapping target angle during ELMs in discharge AUG25764: (a) ELM at 1.757s: Dashed lines represent propagation of perturbation (see text). Solid vertical lines mark times t_1 and $t_{\mathrm{I,div,ons}}$. (b) ELM at 1.851s.

discharge AUG25764. The signals are displaced by the toroidal mapping target angle, where the mapping procedure has been carried out on the $\rho_{\mathrm{pol}} = 0.95$ flux surface. Within the traces from the high resolution array (blue) a very isolated set of one dip followed by one peak can be observed. A similar evolution can be observed as well on most channels of the other arrays. On the channels with lower toroidal mapping target angles the peak intensity is reduced. Magnetic perturbations with comparable strong localization have been observed during ELMs at DIII-D [107].
In the space spanned by time and toroidal mapping target angle the points of a certain phase (e.g. zero crossing) of all arrays are located very close to one straight line (black dashed line in figure 5.3(a)). This is qualitatively consistent with a structure causing the magnetic perturbation, for which the assumption $k_{||} << k_{\perp}$ is valid and which is rotating with constant velocity in the toroidal direction.

TCV

Also during type I ELMs in TCV the time derivative of the magnetic field measured by magnetic probes exhibits peak values clearly above the inter-ELM level. Again the individual ELMs differ significantly from each other in their spatio-temporal magnetic signature. Figure 5.4 displays the time derivative of the poloidal magnetic field dB/dt and the variation in the magnetic field δB relative to a time just before the ELM for the magnetic low field side (LFS) and magnetic high field side (HFS). The overall evolution of δB during the displayed time interval is towards higher (lower) values on the LFS (HFS). This is consistent with a movement of the plasma column radially inward, which in turn is in line with a drop in β. It is remarkable that this rise (fall) in δB is not happening in all toroidal positions at the same time but with a maximum delay of 0.1ms. The toroidal range, where a given level of δB is reached earlier (later) agrees well on the LFS and HFS.

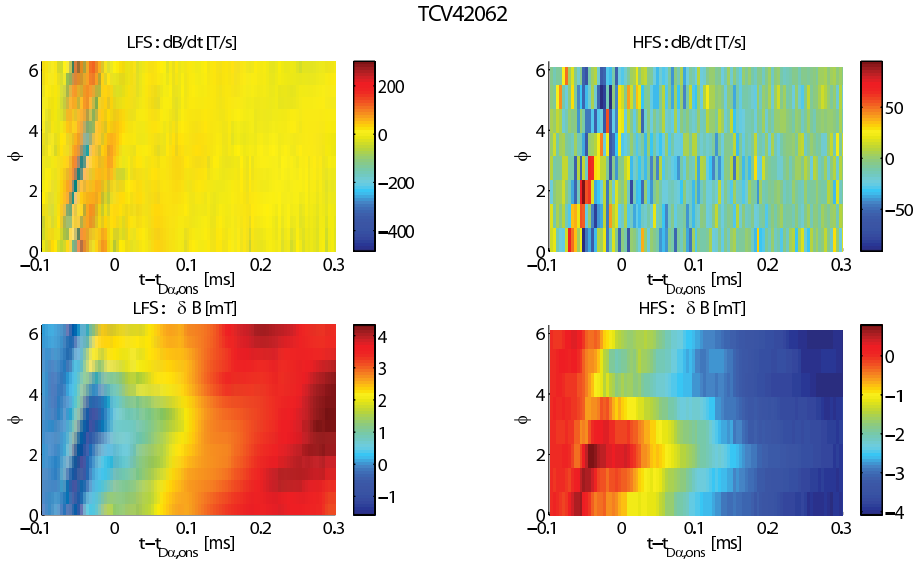

Figure 5.4: Magnetic perturbation during an ELM at 0.6107s in discharge TCV42062: dB/dt (upper row) and δB (lower row) for LFS (left) and HFS (right) as a function of time and toroidal position. δB is obtained from dB/dt by integration starting a time corresponding to the left boundary of the displayed time interval.

On the plot displaying δB on the LFS during the last 0.1ms before $t_{\mathrm{D}\alpha,\mathrm{ons}}$ another feature consisting of relatively high values of δB propagating towards higher toroidal angles can be identified. This temporarily isolated feature constitutes the trajectory of a local maximum (peak trajectory) of δB. Naturally a corresponding structure can be observed on the plot of dB/dt on the LFS. For the HFS due to the reduced number of probes per toroidal rotation the existence of peak or dip trajectories is less clear, but a trace of a peak trajectory can be identified.

5.2 Timing of dominant magnetic perturbations

The timing of the appearance of dominant magnetic perturbations during ELMs relative to the onset of pedestal erosion is investigated. Eventually this supports the development of a more detailed picture of the evolution of an ELM.

ASDEX Upgrade

A first impression of the timing of peak magnetic activity relative to the time of increase of divertor current and D_α-radiation in the outer divertor (reference time) can be obtained from figure 4.6(c). Additionally for a set of magnetic probes the times $t_{\min}$ and $t_{\max}$ are evaluated, which correspond to the maximum or minimum value of the time derivative of the radial magnetic field during the investigated ELM (figure 5.5). Here 14 ELMs with a low number of dominant magnetic excursions in discharge AUG25764 are considered. As reference time t_{ref} the onset times of current $t_{\mathrm{I,div,ons}}$ (a) and D_α radiation $t_{\mathrm{D}\alpha,\mathrm{div,ons}}$ (b) both observed in the outer divertor have been used. For both choices of reference time the strongest magnetic excursions appear between $t_{\mathrm{ref}} - 0.2$ms and t_{ref}. This is later than typical coherent ELM precursors (type I and type III) are observed at AUG and JET [108, 109].

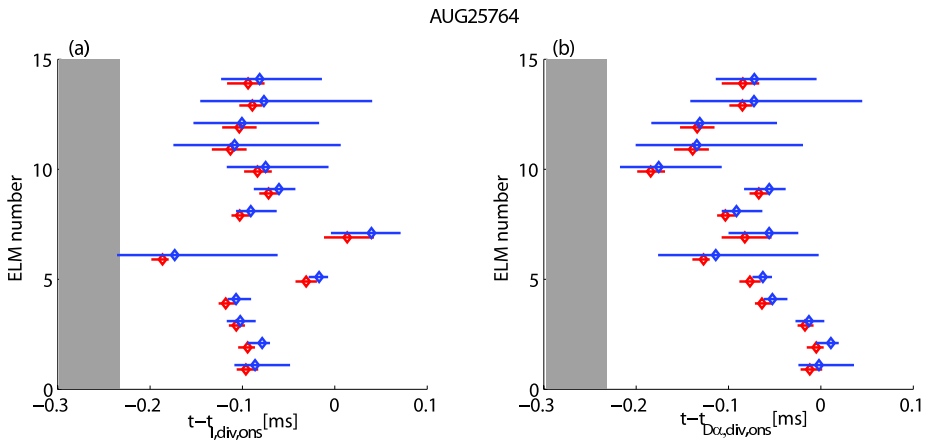

Figure 5.5: Timing of dominant magnetic excursions observed on probes of high resolution poloidal array in discharge AUG25764 from 1.5s to 2.7s: The bars correspond to $[\mu-\sigma, \mu+\sigma]$, where μ and σ are mean and standard deviation of the distribution over the probe set of $t_{\min} - t_{\mathrm{ref}}$ (red) and $t_{\max} - t_{\mathrm{ref}}$ (blue) for an individual ELM. $t_{\min}$ ($t_{\max}$) is the time, when dB/dt takes its minimum (maximum) value during the investigated ELM. For t_{ref} (a) the onset time of the current in the outer divertor $t_{\mathrm{I,div,ons}}$ and (b) the onset time of D_α radiation observed in the outer divertor $t_{\mathrm{D}\alpha\mathrm{,div,ons}}$ has been used. Diamonds indicate median value of the distribution of $t_{\min} - t_{\mathrm{ref}}$ and $t_{\max} - t_{\mathrm{ref}}$.

To further assess the timing of the strongest magnetic excursions two aspects must be considered:

Toroidal rotation: The measurements for both divertor current and divertor D_α-radiation are taken at a single toroidal position. Therefore these reference times do not necessarily correspond to the time of the first effect of the ELM at the divertor. Assuming parallel transport, there is a lag between the toroidally localised effect of a dominant magnetic excursion in the divertor and the detection of this after rotation to a toroidal position, which is observed by divertor diagnostics. The apparent toroidal rotation velocity of dominant magnetic excursions obtained in section 5.5 corresponds to $t_{\mathrm{tor,rot}} = 0.26$ms for a full rotation.

Parallel transport to the divertor: In [110], for an ASDEX Upgrade discharge in upper single null configuration with plasma parameters comparable to discharge AUG25764, information on typical time scales of parallel transport form the outer mid plane to the outer divertor has been reported. In this study a good fit of divertor infrared thermography data with results from a free streaming ion model has been found. Using this model (including the fit results) the time between the start of the parallel propagation at the mid plane and the flux at the divertor exceeding 10% to 20% of the peak value is estimated as $t_{\mathrm{par,transp}} = 215\mu$s to 238μs.

In summary the start of the enhanced parallel transport from the main plasma to the divertor can be expressed as $t_{\mathrm{st,par,transp}} = t_{\mathrm{ref}} - a \cdot t_{\mathrm{tor,rot}} - t_{\mathrm{par,transp}}$, $0 > a > 1$ (qualitatively described by the gray shaded region in figure 5.5). Dominant magnetic excursions are observed usually a few hundreds of μs later than this time. This suggests that already some time before

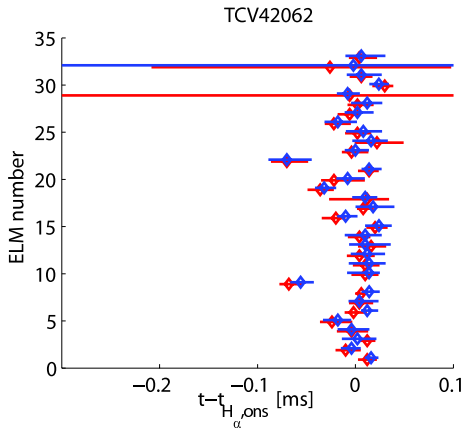

Figure 5.6: Timing of observation of dominant magnetic excursions in discharge TCV42062 from 0.6s to 0.8s: The bars correspond to $[\mu-\sigma, \mu+\sigma]$, where μ and σ are mean and standard deviation of the distribution over the probe set of $t_{\min} - t_{\mathrm{D}\alpha,\mathrm{ons}}$ (red) and $t_{\max} - t_{\mathrm{D}\alpha,\mathrm{ons}}$ (blue) for an individual ELM. $t_{\min}$ ($t_{\max}$) is the time, when dB/dt takes its minimum (maximum) value during the investigated ELM. Diamonds indicate median value of the distribution of $t_{\min} - t_{\mathrm{D}\alpha,\mathrm{ons}}$ and $t_{\max} - t_{\mathrm{D}\alpha,\mathrm{ons}}$.

the appearance of dominant magnetic perturbations the perturbation level is sufficient to cause significantly increased transport. Comparison with section 4.3 shows that the onset of temperature and density pedestal erosion (figure 4.6) is observed at the same time (±0.2ms) as $t_{\mathrm{I,div,ons}}$.

TCV

Figure 5.6 displays corresponding data from discharge TCV42062. Here as reference time $t_{\mathrm{D}\alpha,\mathrm{ons}}$ has been used. The extremely large standard deviation in some cases is caused by single peaks appearing in high temporal distance to $t = t_{\mathrm{D}\alpha,\mathrm{ons}}$. In average the dominant magnetic excursions appear at $t = t_{\mathrm{D}\alpha,\mathrm{ons}}$, which is about 0.1ms later than in the ASDEX Upgrade case. The D_α-signal analyzed here is from both divertor and main chamber (section 4.1). This explains the timing difference with respect to the ASDEX Upgrade case. Hence the timing of appearance of dominant magnetic perturbations at both experiments is consistent.

5.3 Comparison to magnetic fluctuations caused by passing mono-, bi- or multipolar structures (ASDEX Upgrade)

The objective of this section is to deduce from the magnetic field perturbation the structure of the current perturbation causing it. A forward modeling approach is employed, which compares measured trajectories of the time derivative of the magnetic field with ones resulting from basic models of the current perturbation. First this method is applied to the edge snake [104], where it results in a very clear and simple answer. After that the case of dominant magnetic excursions during ELMs is discussed. There the situation appears to be less uniform.

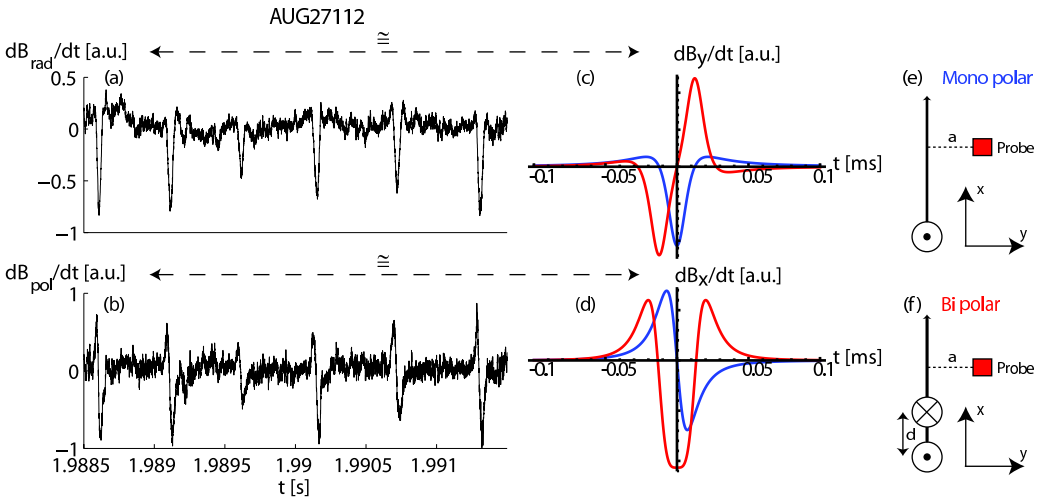

Figure 5.7: Time derivative of the magnetic field components in the poloidal plane perpendicular (a) and parallel (b) to the flux surface in discharge AUG27112. Simulated evolution of the time derivative of the magnetic field components in the y-direction (c) and x-direction (d) for the mono-polar (blue) respectively bi-polar (red) configuration. Setup of the mono-polar (e) and bi-polar (f) case. Parameters: Velocity in x-direction 6km/s, minimal distance a=0.075m, separation of poles d=0.15m

5.3.1 Application to the edge snake (excursion)

The edge snake [104] is an instability located in the edge of H-mode plasmas. To measure the magnetic perturbations associated with edge snakes, a triple axis magnetic probe mounted on the mid plane manipulator is employed (section 4.1). Figures 5.7(a) and (b) illustrate the time derivative of the magnetic field components in the poloidal plane perpendicular (dB_{rad}/dt) and parallel (dB_{pol}/dt) to the flux surface. While the large periodically appearing excursions have even symmetry for dB_{rad}/dt, they have a dominant dominant odd symmetry for dB_{pol}/dt.
To infer information about the current perturbations leading to the observed magnetic perturbations the experimental data is compared with results from very basic models. A mono-polar current filament (figure 5.7(e)) respectively a bi-polar current filament consisting of two filaments offset in the x-direction (figure 5.7(f)) are assumed. Furthermore, all filaments are parallel to the z-direction and move in the x-direction passing the probe with a finite minimal distance a. Figure 5.7 shows the qualitative evolution of the time derivative of the magnetic field components in the x-direction (c) and y-direction (d) for the mono-polar (blue) and bi-polar (red) configuration respectively.
The edge snake is radially located around a flux surface and rotates in the electron diamagnetic drift direction [104]. Thus its main propagation direction is poloidal. Therefore in the comparison between experiment and model the poloidal (radial) direction has to be identified with the x-direction (y-direction). Comparing the symmetries leads to the conclusion that, for the edge snake the bi-polar model is inconsistent with the measurements while the mono-polar model is consistent.

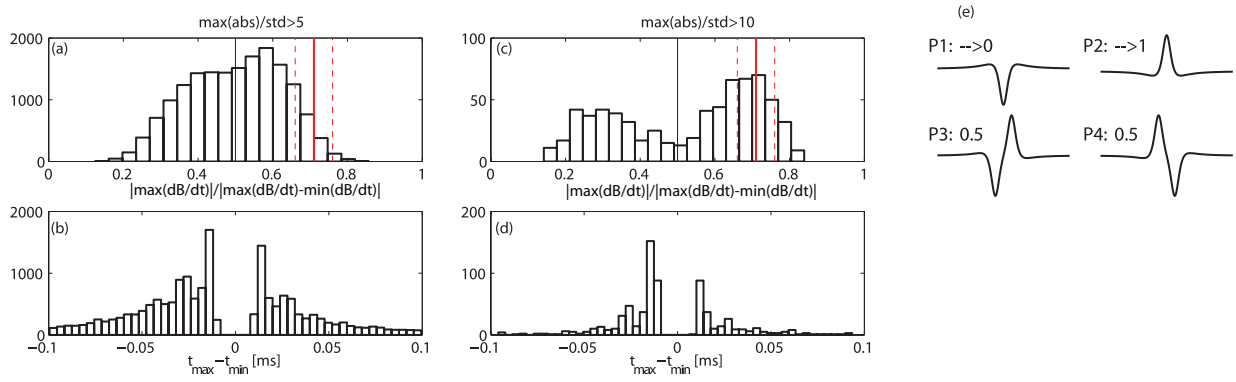

Figure 5.8: Histograms of quantities characterizing main peaks and dips of time derivative of the radial magnetic field measured by a magnetic probe at the outer mid plane for selected ELMs (criteria described in the text): (a) and (c) $|\max(dB/dt)|/|\max(dB/dt) - \min(dB/dt)|$ (red vertical lines indicate mean value and standard deviation of the corresponding quantity for the edge snake displayed in figure 5.7), (b) and (d) $t_{\max} - t_{\min}$. (e) Prototype waveforms including values for $|\max(dB/dt)|/|\max(dB/dt) - \min(dB/dt)|$: P1, P2: Mono-polar and P3, P4:Bi-polar.

5.3.2 Application to dominant magnetic perturbations

In comparison to the edge snake the signature of dominant magnetic perturbations during ELMs has a considerably larger range of possible shapes. Therefore the analysis concentrates on distributions of some indicators constructed on the basis of the extent ($\max(dB/dt)$, $\min(dB/dt)$) and timing ($t_{\max}, t_{\min}$) of the maximum and minimum of dB/dt after subtraction of the mean value in an interval of 1ms centered at $t_{\mathrm{I,div,ons}}$. The analysis is carried out with data from one magnetic probe (B31-02 - location displayed in figure 4.9). The angle between the measurement direction (perpendicular to probe) and the normal vector on the LCFS in the vicinity of the probe is of the order of a few degrees and not compensated. ELMs from discharges AUG26200 to AUG27200 fulfilling the following criteria have been used (a1 and a2 optional):

a1)	$\max(\lvert dB/dt\rvert)/\mathrm{std}(dB/dt) > 5$	(figure 5.8(a) and (b)) or
a2)	$\max(\lvert dB/dt\rvert)/\mathrm{std}(dB/dt) > 10$	(figure 5.8(c) and (d)) and
b)	$\max(dB/dt) - \min(dB/dt) > 3 \times \mathrm{std}(dB/dt)$	and
c)	$\lvert t_{\max} - t_{\min}\rvert < 0.1\mathrm{ms}$	

The first and second criteria are chosen to allow only isolated dominant events. The third one ensures that the main peak and dip are close enough to each other to belong to the same passing structure.
The shape of the perturbations is investigated guided by the four prototype waveforms illustrated in figure 5.8(e). To determine if the investigated waveforms have more similarity to an even (P1 and P2) or odd (P3 and P4) symmetry graph $|\max(dB/dt)|$ and $|\min(dB/dt)|$ are balanced.
Figure 5.8(a) shows that applying condition a1) the histogram of $|\max(dB/dt)|/|\max(dB/dt) - \min(dB/dt)|$ has its maximum close to 0.5 (e.g. $|\max(dB/dt)| = |\min(dB/dt)|$) with a slight tendency towards higher values (e.g. $|\max(dB/dt)| > |\min(dB/dt)|$).[3] The red vertical lines

[3]It should be noted that applying the same analysis to dB/dt data, which are not low pass filtered, leads to a qualitatively identical and quantitatively very similar result.

in figure 5.8(a) indicate mean value and standard deviation of the corresponding quantity for the edge snake displayed in figure 5.7. These values are far off 0 and 1, which are the ideal limits for the even symmetry prototypes. However they correspond to $|\max(dB/dt)|$ being in average higher than $|\min(dB/dt)|$ by a factor of about 2.3. Hence only a subset of the investigated ELMs at the wings of the distribution shown in figure 5.8(a) can have clear even symmetry. For the rest of the ELMs the observed waveforms are incompatible with a mono-polar current filament moving in the poloidal direction. A visual inspection of some of the investigated trajectories confirms this result. Here a significant fraction of trajectories with clear odd symmetry has been observed. A number of examples with even a short sequence of peaks or dips of similar extent to $\max(dB/dt)$ respectively $\min(dB/dt)$ has been observed as well. The latter cases are compatible with a multi-polar (both polarities in alternation) current model approaching a 'regular' MHD mode.
Using condition a2), which selects dominant peaks more strongly, results in a histogram for $|\max(dB/dt)|/|\max(dB/dt) - \min(dB/dt)|$ with two peaks around 0.25 and 0.75 (figure 5.8 (c)). This suggests that the fraction of perturbations with trajectories tending towards even symmetry is higher for this subset of ELMs. Hence the perturbation gets more comparable to an edge snake.
Vianello [111] has investigated magnetic signals acquired by a triple axis magnetic probe mounted on the mid plane manipulator during ELMs in ASDEX Upgrade. In this work it was inferred that the investigated perturbations are consistent with mono-polar current filaments propagating in the SOL. The fact, that this differs from the result of the analysis of dominant magnetic excursions above, suggests differences in the subject of the observation in the two studies. For instance the most common ELM filament in [111] occurs about 1ms after the ELM onset, while dominant magnetic excursions appear significantly closer to the onset of the pedestal erosion (section 5.2).
In figure 5.8(b) and (d) histograms of $t_{\max} - t_{\min}$ are plotted. Positive (figure 5.8(e) P3) and negative (figure 5.8(e) P4) values of this quantity are registered for similar numbers of ELMs. Using condition a2) compared to a1) reduces the average $|t_{\max} - t_{\min}|$ (i.e. dominant peaks and dips appearing closer in time). The gap at $t_{\max} - t_{\min} = 0$ corresponds to the minimal distance between peaks and dips.[4] The peaks of the distributions are located at $\pm(10 \text{ to } 20)\mu$s. Assuming a field aligned bi-polar current filaments at the LCFS rotating with a typical apparent poloidal velocity ($v_{\mathrm{ME,pol}} = 10$km/s) these times would correspond to a perpendicular distance between the filaments of 10cm to 20cm. This compares to poloidal filament extensions of 5-8cm observed by Thomson Scattering [100] and visible camera observation [112].

5.4 Dynamics of magnetic perturbations during ELMs

The onset dynamics of dominant magnetic perturbations is of special interest. It may be compared to typical MHD time scales.

TCV

The magnetic setup of TCV enables the detailed study of the growth and decay of single dominant magnetic excursions. Figure 5.9(a) shows the evolution of the magnetic pertur-

[4] If the analysis is performed without low pass filtering dB/dt the gap narrows but persists.

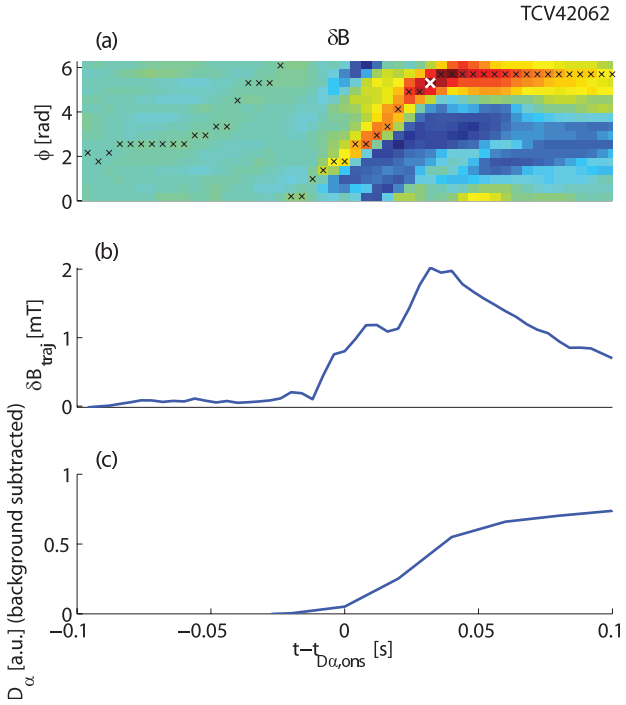

Figure 5.9: Peak trajectory of a magnetic perturbation during an ELM at 0.6107s in discharge TCV42062: (a) Evolution of δB obtained by integration starting at a time corresponding to the left boundary of the displayed time interval and subtracted by the n=0 component for each time step. White and black crosses mark the identified trajectory of the perturbation peak (algorithm described in the text). (b) δB on the peak trajectory (c) D_α-radiation from divertor and main chamber.

bation δB obtained by integration from a point in time before the ELM with the $n = 0$ component subtracted for each time step. A dedicated algorithm identifies a peak/dip trajectory of δB. It first finds the time and toroidal position (white cross in figure 5.9(a)) of the absolute maximum/minimum of δB over all probes and in a certain time window, which corresponds to the range displayed. After this alternately a step in time and the search for the local maximum/minimum of δB as a function of ϕ is carried out (black crosses in figure 5.9(a)).

In figure 5.9(b) the evolution δB_{traj} of δB on the identified trajectory is displayed. δB rises from an inter-ELM value to the peak value within some tens of μs. After that it decays on a slightly slower time scale. The D_α-radiation from divertor and main chamber (figure 5.9(c)) begins to increase at a time close to the onset of δB on the trajectory. A growth rate is not extracted from figure 5.9(b) as the earlier part of the obtained evolution of δB_{traj} might be based on background MHD activity.

In order to obtain more representative information of the dynamics of δB_{traj} coherent averaging is used. The onset time $t_{\mathrm{D}\alpha,\mathrm{ons}}$ of D_α-radiation is used as a reference time for the temporal alignment (figure 5.10(a)). Figure 5.10(b) shows the coherent average of the evolution of δB_{traj}. The rise phase is shorter than 0.1ms, while the decay phase is a little longer.

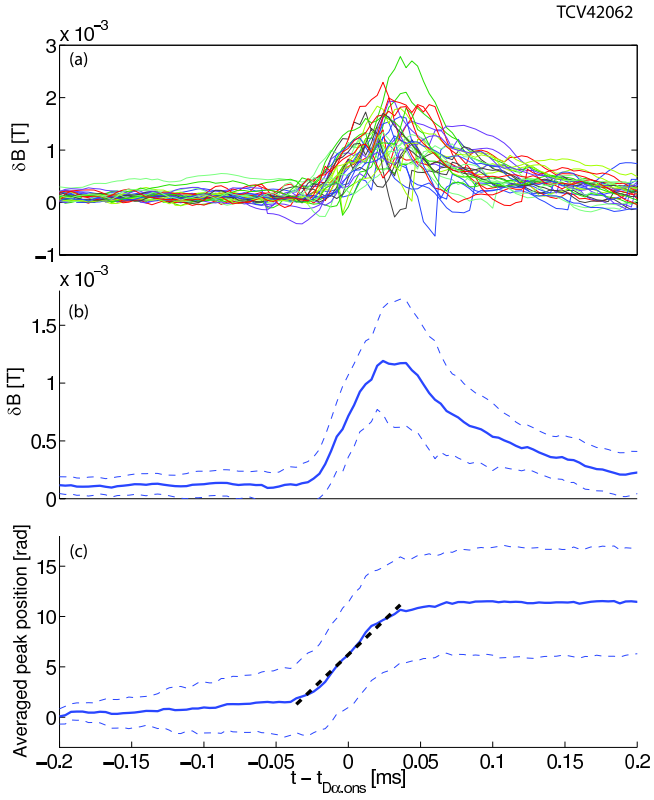

Figure 5.10: Identification of peak trajectories in combination with coherent averaging during ELMs in discharge TCV42062:(a) δB_{traj} evolution for several ELMs aligned using reference time $t_{\mathrm{D}\alpha,\mathrm{ons}}$ ($n = 0$ component subtracted for each time step). (b) Coherent average of δB_{traj} evolution (solid) with interval of width 2 standard deviations around (dashed). (c) Coherent average of the toroidal position of the peak trajectory (solid) with interval of width 2 standard deviations around (dashed). The individual trajectories have been shifted to start at $\phi = 0$ and unwrapped. The black dashed line shows the result of a linear fit during the phase of fastest propagation.

ASDEX Upgrade

In the ASDEX Upgrade case the toroidal resolution is much more limited compared to TCV, but can be extended via diagnostic mapping (section 4.5). Thus it is possible to track the evolution of the shape of a dominant magnetic perturbation with changing toroidal mapping target angle. Next to perturbations with virtually identical trajectories on all channels two classes of temporal variations are observed. Firstly some dominant magnetic perturbations are found to grow or decay. The times and values of the peak of dB/dt of all probes for the fast growing dominant magnetic perturbation displayed in figure 5.3(b) are compared. This peak value is growing within about 10μs by a factor of 4 corresponding to a growth time of $\approx 7\mu$s. After this first phase saturation can be observed. The growth time compares to typical growth times of the most unstable modes in linear stability calculations [68] of about 5μs.

Also it is possible that the shape of the time trace is morphing when changing the toroidal mapping target angle ϕ_{map} (i.e. moving from probe to probe). In the example displayed in figure 5.3(b) a transfer from a shape with dominant even symmetry (e.g. a peak only) into a shape with dominant odd symmetry (e.g. a dip followed by a peak) can be seen.

5.5 Direction and velocity of magnetic excursions

Direction and velocity of dominant magnetic excursions are of interest in a number of respects. They contribute to give information on the radial location of the current perturbations causing magnetic perturbations (section 5.6). Furthermore the direction and velocity of magnetic excursions and filaments observed with fast framing cameras will be compared in subsection 5.10.2.
Generally the measurements described here cannot clarify, whether a field aligned perturbation is propagating toroidally or poloidally or both (barber pole effect). Therefore the apparent toroidal velocity of a magnetic excursion $v_{\mathrm{ME},\phi}$ (apparent perpendicular velocity of a magnetic excursion $v_{\mathrm{ME,perp}}$) is defined as the propagation velocity of the intersection of a line parallel to the magnetic excursion with a line with $\theta = \text{const}$ (parallel coordinate = const). The conversion between these velocities is carried out on the basis of the approximation that the field line is locally straight:

$$v_{\mathrm{ME,perp}}/v_{\mathrm{ME},\phi} = -B_\theta/\sqrt{B_\phi^2 + B_\theta^2}$$

ASDEX Upgrade

In the ASDEX Upgrade example displayed in figure 5.3(a) the line of constant phase (dashed) represents a propagation towards lower toroidal mapping target angle, which corresponds to the electron diamagnetic drift direction when mapped in the perpendicular direction. In a similar way 13 ELMs in the same discharge (AUG25764) with best traceability of phase (i.e. clear dominant magnetic excursions) are investigated. Multiplying the obtained angular velocities of the magnetic perturbations by a radius of 2m leads to an apparent toroidal velocity of the dominant magnetic excursions of 48 ± 11km/s corresponding to an apparent perpendicular velocity of 10 ± 2km/s (LFS). While all of these dominant magnetic excursions propagate in the electron diamagnetic drift direction, there is a small minority of cases moving in the ion diamagnetic drift direction. In section 5.6 the apparent perpendicular velocity of dominant magnetic perturbations is compared to the perpendicular velocity expected for a mode.
The toroidal propagation of the onset location of magnetic activity corresponding to the electron diamagnetic drift direction has been reported earlier for COMPASS-D, JET and ASDEX Upgrade [113, 114, 115, 116]. In [113, 107, 116] single peaks of time integrated components of dB/dt have been followed in this direction.

TCV

In the case of TCV again the algorithm for the identification of peak (dip) trajectories is employed (section 5.4). Tracing the peak trajectory in figure 5.9(a) in time leads to a propagation in the positive toroidal direction. Considering the right-handed helicity of the field lines in this discharge, this can be mapped into the perpendicular direction corresponding to the electron diamagnetic drift direction. Hence the magnetic excursions propagate into the electron diamagnetic drift direction as in the majority of cases at ASDEX Upgrade.
Again in order to obtain more representative information the application of the tracing algorithm is combined with coherent averaging. Figure 5.10(c) shows the coherent average of the toroidal position of the peak trajectory. The individual trajectories have been shifted to start at $\phi = 0$ and unwrapped. The average apparent toroidal velocity is relatively low until

about 50μs before $t_{\mathrm{D}\alpha,\mathrm{ons}}$. Around $t = t_{\mathrm{D}\alpha,\mathrm{ons}}$ it rises to relatively high values and falls to virtually zero about 50μs after $t_{\mathrm{D}\alpha,\mathrm{ons}}$.[5] The linear fit indicated in figure 5.10(c) corresponds to an average apparent toroidal velocity of 148km/s. Regarding the local field line inclination this corresponds to an apparent perpendicular velocity of 32km/s.
For the given time interval this is compared to the electron diamagnetic drift velocity given by

$$v_{*e} = \frac{|B_{\mathrm{pol}}|}{|B_\phi|} \frac{R}{e \cdot n} \frac{dp_e}{d\psi},$$

where n is the density and p_e is the electron pressure. A lower limit of the pressure gradient is calculated from the maximum difference of neighboring channels in the plasma edge. The resulting electron diamagnetic drift velocity of 5.8km/s is clearly lower than the average of the apparent perpendicular velocity of the dominant excursions.
The average apparent perpendicular velocity of the dominant magnetic excursions interpreted as an $\boldsymbol{E} \times \boldsymbol{B}$-drift velocity corresponds to an electrical field of about -40kV/m, which in ASDEX Upgrade H-mode plasmas is close to typical minimum values of the radial electric field [21, 117].[6] Hence the obtained rotation velocities seem to be compatible with the hypothesis applied in section 5.6: $v_{E\times B} - v_{*e} \leq v_{\mathrm{ME,perp}} \leq v_{E\times B} + v_{*e}$.

5.6 Radial location of the associated current perturbation (ASDEX Upgrade)

Information on the radial location of current perturbations causing dominant magnetic perturbations is fundamental in the assessment of the general role of dominant magnetic perturbations in the ELM dynamics. In order to obtain this information the perpendicular rotation velocities of dominant magnetic excursions are compared to the range of perpendicular rotation velocities of a mode (ideal or resistive) expected by theory. In [118] rotation of magnetic islands has been investigated with linear and non-linear calculations. The range of velocities found was well contained within $[v_{E\times B} - v_{*e}; v_{E\times B} + v_{*e}]$. To be cautious all of this interval is used to estimate the possible velocities of a mode. Figure 5.11 illustrates profiles of $v_{E\times B}$, v_{*e}, $v_{E\times B} - v_{*e}$ and $v_{E\times B} + v_{*e}$ for the time interval [2.5s,3.5s] in discharge AUG26324. The displayed radial range ($0.95 \leq \rho_{\mathrm{pol}} \leq 1.0$) corresponds to the overlap of data availability for the main employed diagnostics (charge exchange recombination spectroscopy and Thomson scattering).
Dominant magnetic excursions can be observed on the magnetic signals during many ELMs in the investigated time interval. However for a subset of them a significant signature from core-MHD-activity is superimposed, which hampers the analysis. For the 9 most dominant magnetic excursions, positions of constant phase over all signals are traced (indicated for instance by the black dashed line in figure 5.3(a)). From the slope of this trajectory in combination with major radius and local field line inclination, an apparent perpendicular rotation velocity of the dominant magnetic excursion $v_{\mathrm{ME,perp}} = 11 \pm 3$km/s (section 5.5) is obtained. This velocity is also shown in figure 5.11.
For the entire radial range displayed in figure 5.11, $v_{\mathrm{ME,perp}}$ is inside the range $[v_{E\times B} -$

[5] The significance of the quantity *averaged peak position* is higher, if δB_{traj} is high.

[6] It has to be considered that missing momentum input (i.e. no neutral beam injection) leads to lower minimum values of the electric field.

$v_{*e}; v_{E\times B} + v_{*e}]$. Due to the profile of the pressure gradient the diamagnetic drift velocity v_{*e} approaches zero when leaving this radial interval in either direction. It is also known that $v_{E\times B}$ will rapidly become negative outside the illustrated radial range [21]. In summary, the region where $v_{\mathrm{ME,perp}}$ is contained within the theoretically predicted interval extends from the LCFS to the pedestal top or slightly further inside. This finding is in line with results from an earlier detailed comparison of data from ASDEX Upgrade and forward modeling [119, 86, 116], which came to the conclusion that the magnetic ELM signature is dominated by structures inside the LCFS.

5.7 Toroidal profile and mode structure of magnetic perturbations

The toroidal structure of magnetic perturbations during ELMs is a key feature to compare to linear and non-linear calculations. The work here begins with an analysis of the TCV case, which is much more convenient due to the setup of the magnetic diagnostic. After that an attempt is made to acquire similar information for one ELM at ASDEX Upgrade, which has an extremely toroidally localized perturbation.

TCV

The evolution of δB profiles during the phase the toroidal maximum of $|\delta B|$ is rising to its highest value is investigated. In a first step, employing the algorithm identifying peak/dip trajectories introduced above (section 5.4) the average apparent toroidal velocity of a dominant excursion is evaluated. The toroidal profiles are analyzed in the frame moving with this velocity, where the dominant excursion is at rest.[7]

[7]Form the average apparent toroidal velocity a toroidal angle $\phi_{\mathrm{shift}}(t)$ is calculated, by which the profile at a given time has to be shifted, to be in the frame where the perturbation is at rest. To cope with the

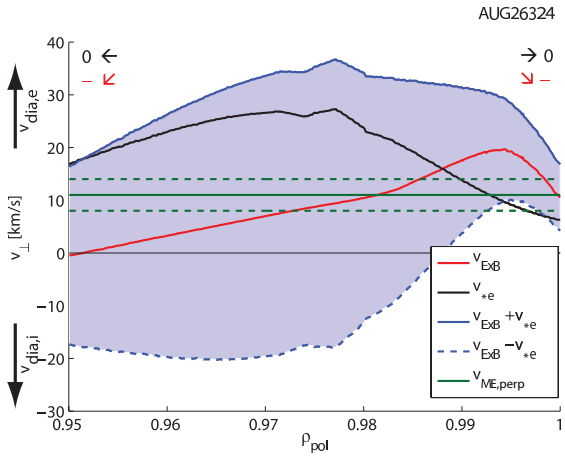

Figure 5.11: Comparison of perpendicular velocities for 2.5s to 3.5s in discharge AUG26324: $v_{E\times B}$ (red), v_{*e} (black), $[v_{E\times B} - v_{*e}; v_{E\times B} + v_{*e}]$ (shaded region) and $v_{\mathrm{ME,perp}}$ (solid green with interval of one standard deviation in dashed green).

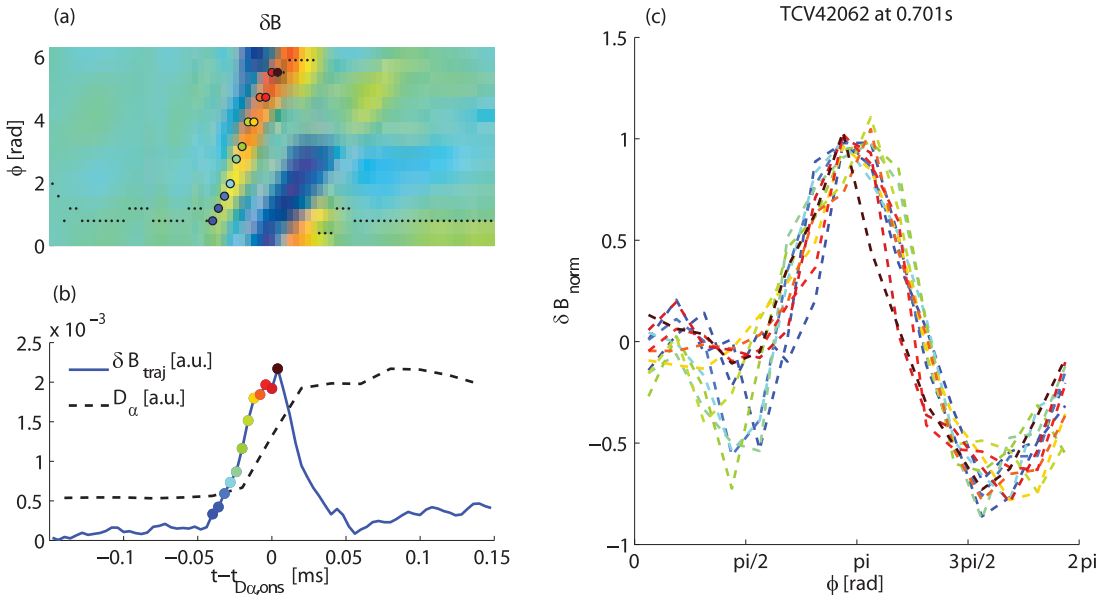

Figure 5.12: Evolution of profiles of δB in the rise phase of an ELM at 0.7011s in discharge TCV42062: (a) δB as function of t and ϕ. The identified trajectory is marked by dots (the larger ones in color indicate time steps shown in (c)). (b) Evolution of δB_{traj} and D_α-radiation. (c) Toroidal profiles of δB normalized by δB_{traj}(t). For the identification of time instances the same color code as for the dots in (a) and (b) is used.

Figure 5.12(a) and (b) shows the evolution of a magnetic perturbation in $t-\phi$-space and the corresponding evolution of δB_{traj} during a phase, in which δB_{traj} is growing more than a factor of 10 up to its maximum value. Figure 5.12(c) shows the associated evolution of the shifted profiles normalized by δB_{traj}. In the early time instances the profiles are clearly influenced by background fluctuations. Also the minimum at $\phi \approx \pi/2$ is evolving in relative depth. However a rigid fundamental shape is maintained throughout the entire time interval displayed. A similar behavior has been observed for the majority of ELMs.
This motivates a semi-analytical approximate description of $\delta B(\phi, t)$ using a separation Ansatz:

$$\delta B(t, \phi) = g(t) f(\phi_R) \text{ with } \phi_R = \phi - \omega t, \tag{5.1}$$

where ϕ_R is the toroidal angle in the system rotating with the perturbation, g is a function describing the overall growth and decay of the perturbation and f represents a fundamental toroidal mode structure.
In order to investigate the fundamental toroidal structures of the perturbations again the frame is chosen, in which the perturbation is at rest. After the toroidal shift the profiles are averaged for each toroidal position over time.[8] The criteria for the selection of time instances t to include are:

problem of discretisation of toroidal positions Fourier representation is chosen and the following identity is used: $FT(B(\phi + \phi_{\text{shift}}(t), t)) = e^{i\phi_{\text{shift}}(t)} FT(B(\phi, t))$, ($FT$:*Fourier transform*). From the obtained Fourier coefficients the shifted profiles in real space are reconstructed.

[8] $FT(\sum_t B(\phi + \phi_{\text{shift}}(t), t)) = \sum_t FT(B(\phi + \phi_{\text{shift}}(t), t)) = \sum_t e^{i\phi_{\text{shift}}(t)} \cdot FT(B(\phi, t))$

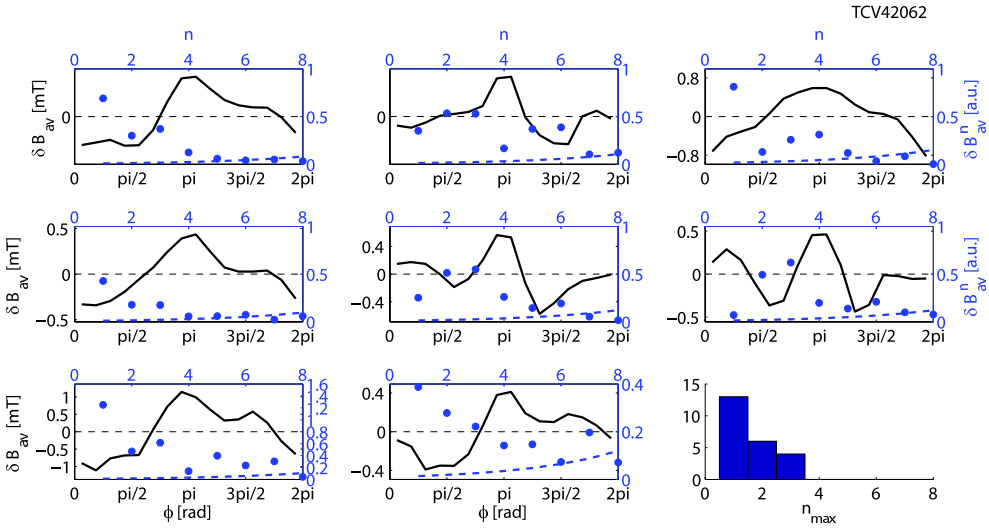

Figure 5.13: Shifted and averaged toroidal profiles of δB during the growth phase of 8 ELMs in discharge 42062: All figures except the bottom right one show for an individual ELM the magnetic perturbation δB_{av} averaged over a number of selected time instances as a function of ϕ (black). In the same plots the amplitudes of the mode components δB^n_{av} (compensated by $(r/r_P)^{0.91n}$) are illustrated (right and top axis, blue). The blue dashed lines represent the Fourier transform of the inter-ELM fluctuation level. The bottom right plot shows the histogram of the mode number $n_{\max}$ corresponding to the maximum compensated amplitude of the mode component over a set of 23 ELMs.

1) $t \leq t(\delta B_{\text{traj}} = \max(\delta B_{\text{traj}}))$,
2) $\delta B_{\text{traj}}(t) > 0.5 \cdot \max(\delta B_{\text{traj}})$,
3) the set of time instances is without gaps and ends at $t = t(\delta B_{\text{traj}} = \max(\delta B_{\text{traj}}))$.

Normalization to the overall growth (function g) is not applied, as the variation in amplitude is limited by the second selection criterion. More than 50% of the ELMs are deselected due to failure of the tracing algorithm or less than 4 time instances fulfilling the criteria.
Figure 5.13 displays the shifted averaged profiles of δB for 8 ELMs in discharge TCV42062. A considerable range of profile shapes can be observed. As seen above these toroidal profiles approximatively grow in a way conserving their fundamental shape. This would not be the case for uncoupled mode components rotating with different velocities due to different radial mode component centers. Hence there is a strong indication of coupling of toroidal mode components, which is an indication of a perturbation of non-linear extent as discussed in subsection 2.2.2.2.
Nevertheless it is instructive to analyze the corresponding Fourier coefficients.[9] The Fourier representation has at least one further advantage. The radial decay of magnetic perturbations depends on the local poloidal mode number, which is determined by the local field line inclination and the toroidal mode number. As the local field line inclination is rather constant close to the LCFS at the LFS it is straight forward to compensate this radial decay in the Fourier representation.
In order to assess this radial decay as a function of toroidal mode numbers a code has been

[9]The sampling rate of 250kHz in combination with the rotation velocity allows for modes up to $n = 25$ to be resolved.

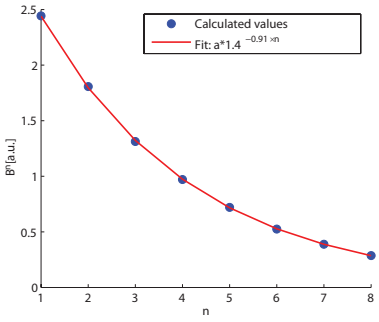

Figure 5.14: Mode number dependent radial decay of perturbations from a model constructing the mode from current filaments: The amplitude of the magnetic field component seen by the probe as a function of toroidal mode number for n=1,2,...,8 is shown as blue dots. The result of a fit ($|FC| = a \cdot 1.4^{-0.91 \cdot n}$) is shown as a red line.

used that is evaluating synthetic probe signals caused by a mode, which is represented as a superposition of current filaments [120]. For toroidal mode numbers $n = 1-8$ perturbations with identical amplitude in current density have been examined. Figure 5.14 illustrates the amplitude of the magnetic field component seen by the probe as a function of toroidal mode number. Corresponding to the cylindrical model derived in section 3.1 the radial decay of the magnetic field perturbations is proportional to $(r/r_P)^{-(m+1)}$. Transferring this to toroidal geometry one has to use the local poloidal mode number yielding as radial decay: $(r/r_P)^{-(m_{\mathrm{loc}}+1)} = (r/r_P)^{-(d\phi/d\theta \cdot n+1)}$. The field line inclination $d\phi/d\theta$ locally at the outboard mid plane takes values of unity or even below. On the basis of these considerations the function $a \cdot (r/r_P)^{-b \cdot n}$ is fitted to the amplitudes in figure 5.14, where for r/r_P the value 1.4 is used, which is obtained from the equilibrium reconstruction for the investigated discharge using for r the LCFS radius in the poloidal position of the probe.
The general trend that can be observed in the set of ELMs displayed in figure 5.13 (circles - right and top axis) is that even with compensation of the radial decay effect described above the absolute values of the Fourier coefficients δB^n_{av} are higher for low toroidal mode numbers than for high toroidal mode numbers. This can be expressed also in another way by counting the number of ELMs, for which $n = 1, 2, 3, ...$ is the mode number with the highest δB^n_{av} (figure 5.13 bottom right plot). For a large majority of ELMs $n = 1$ is dominant.
It is important to assess, whether the Fourier components before the compensation are above the noise level. Therefore the Fourier transform of the inter-ELM fluctuation level[10] is indicated as a dashed line in figure 5.13. Only in some cases the absolute value of the coefficients corresponding to the higher toroidal mode numbers are below this level. However this casts no doubt on the general trend of components with low toroidal mode number dominating.
It is further analyzed, if the dominance of the low toroidal mode numbers is just virtual due to aliasing. For a system with 16 equally spaced probes $n = 8$ is the spatial correspondence of the Nyquist frequency. First, in a basic model ($\delta B(\phi, t) = B_0 \sin(n\phi - \omega t)$) the apparent angular velocity $v_{\mathrm{peak},\phi}$ of the peak in real space is compared to the time derivatives $d/dt(\arg(a_n))$ of the angle of the Fourier coefficients. For $0 < n < 8$ the signs of $v_{\mathrm{peak},\phi}$ and $d/dt(\arg(a_n))$ are opposite, while they are identical for $8 < n < 16$. This can be explained by an aliasing effect in the latter case. Figure 5.15 shows the evolution of δB for an ELM at 0.6533s in discharge TCV42062. Also the evolution of the angles of the Fourier coefficients

[10] Here it is assumed that these fluctuations are distributed uniformly to mode numbers $n = 1, 2, ..., 8$.

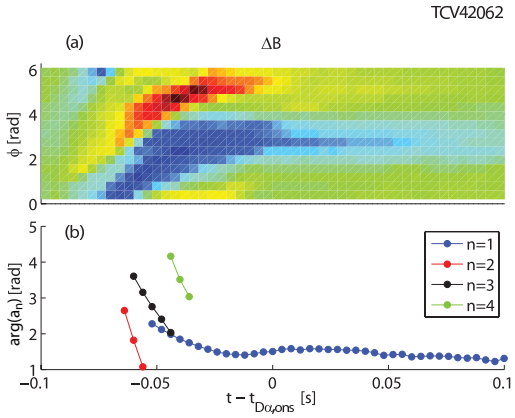

Figure 5.15: Comparison of velocities for an ELM at 0.6533s in discharge TCV42062: (a) δB as function of ϕ and t (b) Phase of the Fourier coefficients for $n = 1-4$. Only time instances are displayed at which the absolute value of the Fourier coefficient is exceeding 10% of the maximum over the time interval displayed and toroidal mode numbers 1 to 8.

$(n = 1 - 8)$ are illustrated for time instances, at which δB^n_{av} is exceeding 10% of the maximum over the time interval displayed and over toroidal mode numbers 1 to 8. The signs of $v_{\mathrm{peak},\phi}$ and $d/dt(\arg(a_n))$ are opposite. This is a clear indication that the mode components for $0 < n < 8$ are stronger as the ones for $8 < n < 16$ and that aliasing is playing no or a minor role.
The finding that the $n = 1$ component is most often dominant is now compared to results from linear stability calculations presented in [64]. For some of these calculations experimental data have been taken from discharge TCV38008, which has similar values as TCV42062 for toroidal magnetic field, plasma current and electron density and temperature at the pedestal top. The discharges have some differences in total heating power (TCV38008: 0.9MW, TCV42062: 1.5MW) and the position of the outer strike point (TCV38008: bottom wall, TCV42062: outside wall). In both discharges ELMs are identified as type-I.
The code KINX [63] evaluates the linear growth rates of coupled peeling-ballooning modes. As input information the geometry of the plasma boundary and profiles of pressure and current density are used. KINX generates a stability map in normalized pressure gradient α and parallel current density $j_\parallel/\langle j\rangle$, where $j_\parallel$ is taken at the position of the maximal pressure gradient and $\langle j\rangle$ is the current density averaged over the full cross section.
Figure 5.16 shows the stability boundaries for $n \in \{3, 5, 10, 15, 20, 40, \infty\}$ (compare figure 2.3). Clockwise along the boundary of the stable region (stable for all n) the toroidal mode number of the first unstable mode changes from low to high values. The operational point C, which represents the time before the ELM crash in its closest temporal vicinity, is in a region, where the first unstable mode has a toroidal mode number of 20 or larger. In summary the dominant toroidal mode numbers observed in the experiment ($n \in \{1, 2, 3\}$) strongly differ from the first linearly unstable toroidal mode numbers in KINX calculations for a comparable discharge.

ASDEX Upgrade

The investigation of the toroidal profile and associated Fourier components of magnetic perturbations during ELMs for ASDEX Upgrade is structured in two parts. In a first step

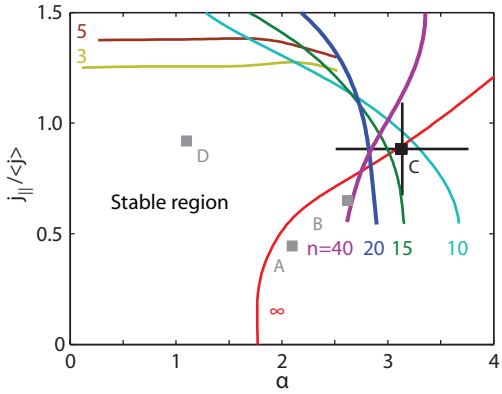

Figure 5.16: Ideal MHD stability map for discharge TCV38008 obtained by calculations with the code KINX [63]. A measured radial displacement of the pedestal has been considered [64]. The stability lines correspond to $\gamma = 0$. Point A represents the profile averaged over the ELM-period. B, C and D correspond to the relative times $t - t_{\mathrm{ELM}} = \{-5.0, -1.0, +1.5\}$ms, where t_{ELM} is the time, when the peak in D_α-radiation is reached. The figure is adapted from [64].

the number N_{dom} of dominant peaks per toroidal turn is investigated. Here the focus is again on discharge AUG25764 (fig. 5.3(a)). After this an attempt at an analysis similar to the one applied in the TCV case above, but on the basis of much more gappy information, is presented.

The resolution limit in terms of N_{dom} is determined by the angle spanned by the toroidal mapping target angles of the coil positions. Using only sensors in one poloidal plane (e.g. red graphs in fig. 5.3(a)) enables to the resolution of $N_{\mathrm{dom}} = 6$ and higher. The mapping technique allows the use of a set of coils with toroidal mapping target angles covering a larger range of the circumference in appropriate density. With this set, $N_{\mathrm{dom}} = 3$ and higher can be resolved.

As stated above, the black dashed line in figure 5.3(a) illustrates the trajectory of the central zero crossing of the dominant magnetic perturbation in the $t - \phi_{\mathrm{map}}$-space. At the time t_1 this trajectory passes the upper end of the interval covered by the ϕ_{map}-values. As for the entire displayed time interval, only one dominant dip or peak can be observed in the entire ϕ_{map}-interval at the time $t = t_1$.[11] However, if there were 3 or more dominant, equally spaced dips or peaks per toroidal turn, a further dip or peak should be observed at time t_1. Hence N_{dom} is equal to 1 or 2 or the dominant peaks are not equally spaced.

More information on the number of dominant peaks per toroidal turn can be obtained by studying the relationship of edge snakes and ELMs. Figure 5.17 shows an ELM and about 1.5ms of the preceding phase in discharge AUG24059. Dominant magnetic perturbations can be observed about 0.2ms before $t_{\mathrm{I,div,ons}}$. The characteristic dips of an edge snake can be observed prior to this. Tracing the dips of the edge snake over several toroidal turns finally leads to the determination of the trajectory of a dominant magnetic excursion. The velocity of the edge snake perturbation is clearly lower than the one of the dominant magnetic excursion during the ELM phase. Similar behavior is observed on a regular basis in the time interval from 3.5s to 3.9s in this discharge. 25 cases are observed where edge snake and

[11] In figure 5.3(a) a weaker structure can be observed in addition to this dominant peak. Comparison with the original data shows that this structure is due to the applied low pass filter in combination with the strong dominant peak.

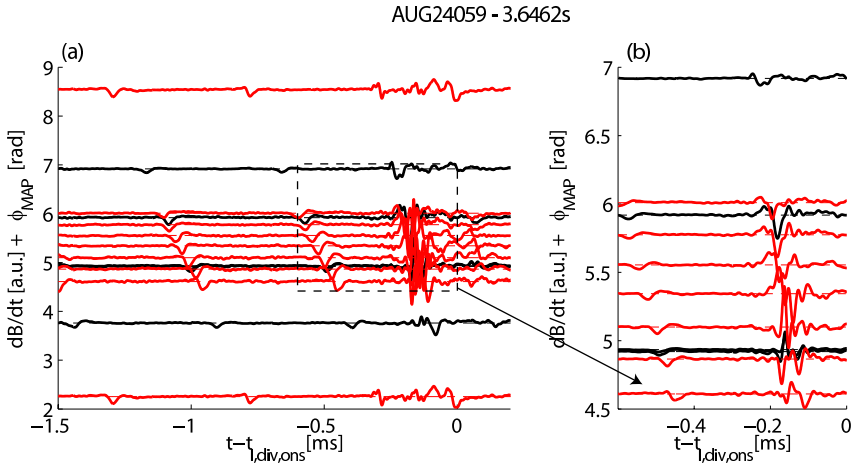

Figure 5.17: (a) Time derivative of the radial magnetic field measured by various pick up coils (color code indicated in figure 4.9) displaced by the toroidal mapping target angle prior to and during an ELM in discharge AUG24059 at 3.6462s. An identical time trace measured by the filament probe is shown on top and bottom with a relative vertical displacement of 2π. (b) Close up of (a) with lower signal amplification.

subsequent dominant magnetic excursion are on virtually the same trajectories, while only one with different trajectories is found.
This observation suggests that the edge snake associated current perturbation develops into the structure causing the dominant magnetic perturbation during the ELM. The edge snake has been reported to have often one peak per toroidal turn [104]. As can be seen this is also the case for the edge snake in figure 5.17. Due to the fast transition into the dominant magnetic perturbation and the relatively short life time of the dominant magnetic perturbation it seems natural to assume that the number of dominant peaks per toroidal turn is identical for the edge snake and the dominant magnetic perturbation during the ELM. This would imply that N_{dom} is equal to 1 for the dominant magnetic perturbation during this ELM.
In both cases (AUG25764 and AUG24059) there is evidence that the number of dominant peaks per toroidal turn N_{dom} for the investigated dominant magnetic perturbations is 1 or 2. Again this result is of special significance when compared to results from linear stability analysis [101]. Here a toroidal mode number n of 1 or 2 is even below mode numbers of the most unstable modes for typical kink/peeling modes ($n \approx 3-6$) and clearly below the ones for typical peeling-ballooning modes ($n \approx 5-20$). However N_{dom} might be different to the linearly most unstable toroidal mode number. Therefore in the remainder of this section the toroidal mode structure of an ASDEX Upgrade ELM with a toroidally very localized magnetic perturbation is obtained and analyzed.

Due to the positioning of the relevant probes extracting a toroidal spectrum of the magnetic perturbation δB is considerably more difficult for ASDEX Upgrade when compared to TCV. Figure 5.18 shows the evolution of dB/dt and δB measured by various pick up coils. The trajectories have been vertically displaced by ϕ_{map}. The integrated signals δB show trends that are dependent on the poloidal position of the probe. For instance the signals of two probes with a similar mapping target angle of about 5rad (marked by a little arrow) show a quite different evolution before the main dip related to the dominant magnetic excursion. In general signals acquired by probes with lower poloidal angle are associated with a rising

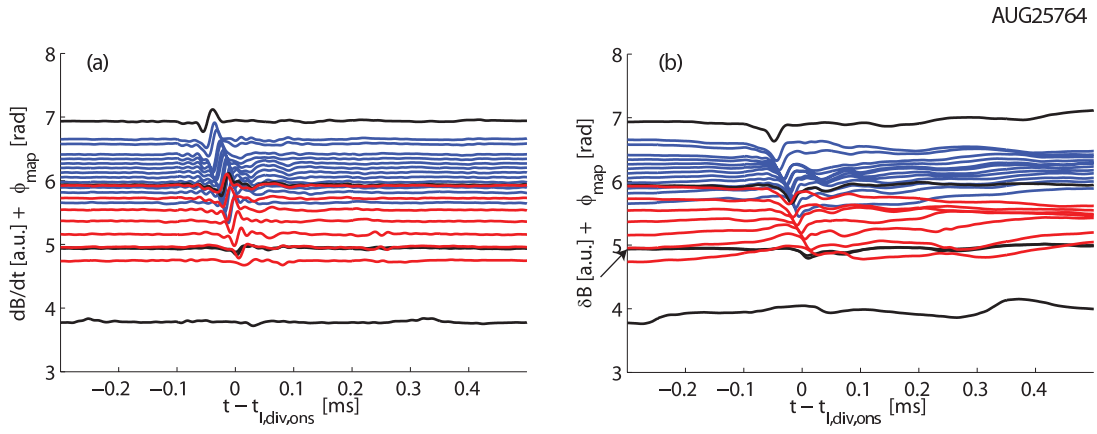

Figure 5.18: ELM in discharge AUG25764 at 1.757s: (a) Time derivative of the radial magnetic field measured by various pick up coils (color code indicated in figure 4.9) and (b) magnetic perturbation δB obtained by integration from a time corresponding to the left boundary of the displayed area. All signals are vertically displaced by the toroidal mapping target angle.

trend, while signals from probes with higher poloidal angle show a falling trend. For dB/dt these trends translate into moderate constant offsets with less distorting consequences for the toroidal profiles at a certain time. Therefore in this analysis a mapped profile of dB/dt shown in figure 5.19(b) is investigated.
Figure 5.19(a) displays for each magnetic probe the maximum of dB/dt during the ELM. In the following a profile of dB/dt (shown in figure 5.19(b)) at the time t_0 (vertical line), at which the peak values shown in figure 5.19(a) are relatively constant, is analyzed. Using the separation Ansatz 5.1 this means $\dot{g}(t) \approx 0$ giving

$$\dot{B}(t,\phi) = \dot{g}(t)f(\phi-\omega t) - g(t)\omega\frac{df}{d\phi_R}(\phi-\omega t) \approx -g(t)\omega\frac{df}{d\phi_R}(\phi-\omega t). \tag{5.2}$$

Therefore it is assumed that the profile of dB/dt has the same shape as the spatial derivative of the fundamental toroidal mode structure f. If the fundamental toroidal mode structure is expressed as a Fourier series $f(\phi_R) = \Re(\sum_n a_n e^{in\phi_R})$ its spatial derivative can be written as $df/d\phi_R = \Re(\sum_n ina_n e^{in\phi_R})$. Thus the absolute values of the toroidal mode components of the profiles of dB/dt are assumed to be up to a constant factor identical to those of $\delta B/n$.
The conversion of the profile of dB/dt into toroidal mode components is complicated in several ways. There are only signals of 5 probes in an identical poloidal position (outer mid plane) available. Therefore probes in various poloidal positions at the LFS are used employing diagnostic mapping.[12] An advanced version of diagnostic mapping (section 4.5) has been applied.[13] Figure 5.20(a) shows the values of dB/dt measured at $t_{\mathrm{I,div,ons}} - 0.02$ms (full circles). The toroidal mapping target angles are not equally spaced. Therefore a standard Fourier technique is not applicable. A generalized linear least square fit (appendix B) is used as an alternative. Finally in about half the toroidal circumference no probe has

[12]The analysis of JOREK data in section 6.2 shows that the level of fluctuation of ψ is a function of the poloidal angle. Therefore diagnostic mapping could lead to errors.
[13]$d\theta_{0,\mathrm{probe}}/d\theta_{\mathrm{mode}}$ is chosen such that the profile smoothness in terms of jumps between profile points based on measurements from different arrays is optimized.

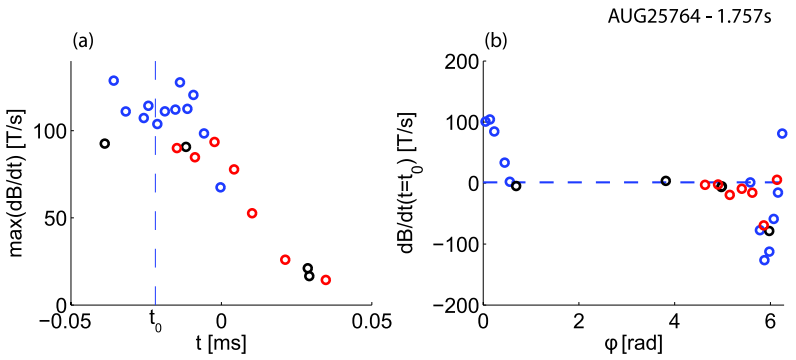

Figure 5.19: Detail analysis of time derivative of the radial magnetic field during an ELM at $t_{\mathrm{I,div,ons}} = 1.757s$ in discharge AUG25764: (a) For each magnetic probe the maximum of dB/dt during the ELM is plotted against the time the maximum is reached. The vertical line indicates the time $t_0 = t_{\mathrm{I,div,ons}} - 0.02\mathrm{ms}$. (b) Mapped profile of dB/dt for the time $t_{\mathrm{I,div,ons}} - 0.02\mathrm{ms}$. The color code corresponds to the one in figure 4.9.

its toroidal mapping target angle.[14] Assuming that the peak in dB/dt around $\phi = 2\pi$ is the only one in the full toroidal circumference, virtual probes measuring $dB/dt = 0$ have been added (figure 5.20(a) open circles). This assumption will be discussed in the last part of this section. Figure 5.20(a) shows as well the reconstructed continuous profile of dB/dt.
Figure 5.20(b) shows the toroidal mode components of dB/dt (black circles). As explained above these have to be divided by n to obtain up to a constant factor the toroidal mode components of δB (red circles). Furthermore in order to obtain the toroidal mode spectrum of δB at the position of the mode, the radial decay of magnetic perturbations as a function of the toroidal mode number has to be considered. To assess this decay for the ASDEX Upgrade case a superposition of two modes ($n = 1$,$m = 4$ and $n = 10$,$m = 40$) on the $q = 4$ surface with identical amplitude in current density has been simulated with the synthetic magnetic module SYNMAG. On the basis of synthetic magnetic fields from this simulation analogously to the TCV case the radial decay has been approximated as $(r/r_P)^{-0.62 \cdot n+1}$. r/r_P, describing the distance of the probe to the magnetic axis relative to the distance of the mode location to the magnetic axis, has a value of about 1.34.
Figure 5.20(b) illustrates the compensated spectrum for δB (blue circles), which is remarkably flat. This is consistent with a strong localization in real space. This flat spectrum is in contrast to the clear dominant low n components in the TCV case. However it is also clearly different than the typical shape of the spectrum in linear stability calculations showing a strong drop of growth rates towards $n = 1$ [68].
Figure 5.20(c) and (d) illustrate profiles and absolute values of corresponding Fourier coefficients for the analytic profiles $\frac{d}{d\phi}(\sin(0.5\phi)^k)$. Comparing the width of the peaks and dips in these profiles with the reconstructed profile in figure 5.20(a), the best fit is obtained for the exponent $k = 50$.

On the basis of the information collected so far for the analyzed ASDEX Upgrade ELM two possible analytical descriptions of the spatio-temporal structure of the magnetic perturbation are discussed. Again the separation Ansatz 5.1 is used. For the growth function a

[14] The level of artificial excursions of a profile reconstructed after calculation of Fourier coefficients by generalized linear least square fit scales with the largest toroidal gap of probe positions.

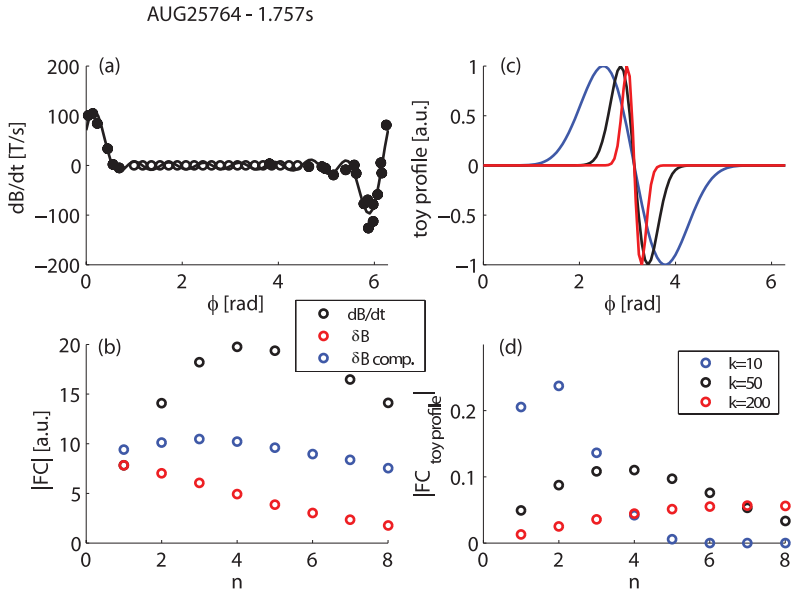

Figure 5.20: (a) Profile reconstruction of dB/dt for an ELM in discharge AUG25764 at 1.757s: Full (open) circles display values measured by real (virtual) probes. The line shows the profile reconstructed from the Fourier components. (b) Absolute values of Fourier coefficients: Values for dB/dt obtained by generalized linear least square fit (black), values for $(dB/dt)/n \approx \delta B$ (red), compensated (see text) values for $(dB/dt)/n \approx \delta B$ (blue). (c) Analytic profiles: $\frac{d}{d\phi}(\sin(0.5\phi)^k) = 0.5k \cdot \cos(0.5\phi)\sin(0.5\phi)^{k-1}$ (normalized). (d) Fourier coefficients corresponding to the analytic profiles.

Gaussian is chosen. From figure 5.19(a) a lower limit for the FWHM of 50μs can be obtained. For the fundamental toroidal mode structure of δB two options are compared:

a) Version with one peak per toroidal rotation: $\sin(0.5\phi)^{50}$
b) Version with two peaks per toroidal rotation on opposite sides: $\sin(\phi)^{10}$

The width of a single peak is similar for the two options. For the toroidal angular frequency 24krad/s, as obtained from the measurement, is used (section 5.5). Figure 5.21 displays dB/dt as function of time and toroidal angle for the two options. For these parameters it is obvious that each probe will not register more than one peak. However in the experiment a set of probes with mapping target angles densely spanning one third of the toroidal circumference ($\Delta\phi$) is employed. Furthermore the FWHM 50μs for the growth function is only a lower limit.
To assess the relevance of option (b) the ratio of two temporal peaks of dB/dt is evaluated:

- Toroidal peak P_1 registered by probe in position ϕ_1
- Toroidal peak P_2 registered by probe in position ϕ_2

This ratio takes its maximum value, if the two probes have the maximum toroidal separation, and, if one probe observes a peak at $t = 0$. In this case the other probe observes the other peak at $t = \pm(\pi - \Delta\phi)/\omega$ and the maximum ratio between the two observed peak heights is $\exp(-0.5(\frac{\pi-\Delta\phi}{\omega})^2)$. Figure 5.22 shows this ratio as a function of the FWHM of the growth function using $\Delta\phi = 2$rad corresponding to the toroidal range densely covered by probes in the experiment. If the FWHM rises towards 0.1ms the ratio increases to an extent, that it would be possible to identify the second peak. Hence for the experimental example displayed

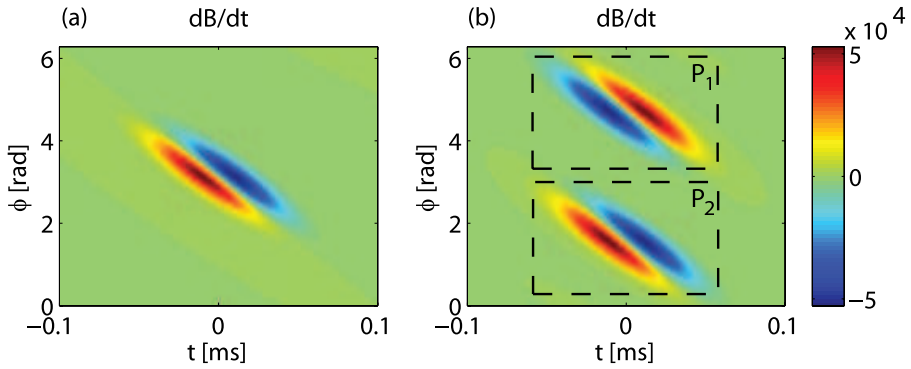

Figure 5.21: Spatio-temporal structure of dB/dt based on analytical models: (a) One peak per toroidal rotation ($\delta B = e^{-0.5(t/\sigma)^2} \sin^{50}[0.5(\phi+\omega t)]$), (b) two opposite peaks P_1 and P_2 per toroidal rotation ($\delta B = e^{-0.5(t/\sigma)^2} \sin^{10}[\phi + \omega t]$). Parameters: $FWHM = 2\sqrt{2\ln 2}\sigma = 50\mu$s, $\omega = 24$krad/s.

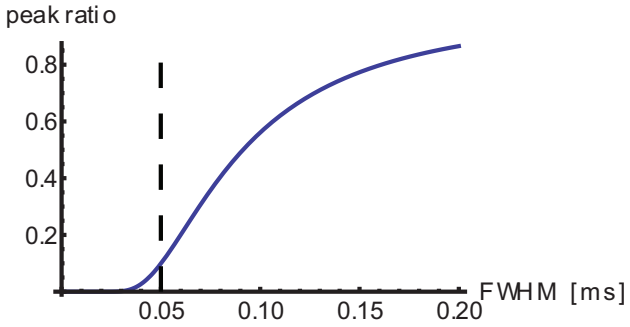

Figure 5.22: Maximum ratio of heights of two peaks (option (b)) observed by two probes toroidally separated by $\Delta\phi = 2$rad as a function of the FWHM of the growth function. The first probe is assumed to observe one peak at $t = 0$. The vertical line marks the minimum FWHM (see text).

in figures 5.19 and 5.20 one can neither prove that there is only one nor that there are two peaks per toroidal rotation. However it is clear that there are less than three peaks per toroidal rotation, if these are toroidally equally spaced.

5.8 Toroidal mode coupling and solitariness of magnetic perturbations

Figure 5.12 shows for an ELM in TCV that apart from a toroidally symmetric growth and rotation the toroidal profile of the perturbation is approximately rigid. It is straight forward to show that under such conditions the phase velocities of the Fourier components have fixed ratios

$$d/dt(\arg(a_n)) = n \cdot \omega_0. \tag{5.3}$$

This is equivalent to a coupling of the toroidal mode components. As discussed in subsection 2.2.2.2 toroidal coupling is not expected in a situation with a linear perturbation. Hence it is an indication that the perturbation has to be regarded as a signature from the non-linear phase of the perturbation.

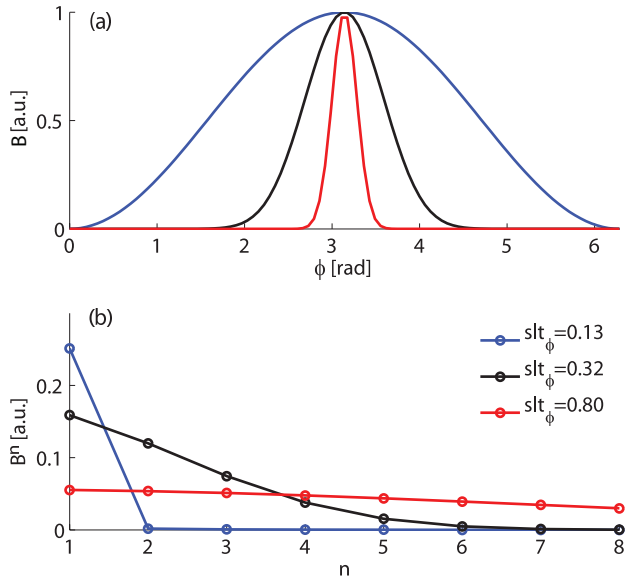

Figure 5.23: (a) Synthetic toroidal profiles: $\sin(0.5\phi)^{\mu}$ ($\mu = 2$: blue, $\mu = 20$: black, $\mu = 200$: red). (b) Absolute values of corresponding Fourier coefficients and values of slt_{ϕ}.

The magnetic perturbation during the ELM in discharge AUG25764 shown in figure 5.3(a) is reminiscent of a soliton. A soliton is often described as a wave that maintains its shape and propagates with constant speed [121]. However there is a fundamental difference between solitons and magnetic perturbations during ELMs, as the earlier ones are waves while the latter ones are a feature of an instability. Correspondingly the existence of magnetic perturbations during ELMs has a restricted duration, as expressed by the growth function g in the separation Ansatz 5.1.
In a situation with one spatial coordinate x the spatio-temporal evolution of the displacement of a soliton can be described as $h(x - ct)$, where c is the group velocity and h is a function representing a rigid propagating profile. At a given time the rigid profile is non-zero only in a limited interval. Transferring this to toroidal geometry would mean to convert the non-periodic coordinate x into the periodic coordinate ϕ. A criterion for *similarity to a soliton* in toroidal geometry is fulfilled, if the displacement is confined to a limited toroidal region. This is equivalent to the existence of toroidal regions with significant extension and negligible displacement. For simplicity the radial and poloidal coordinates are omitted. This is based on the assumption that the radial variation of the displacement can be neglected and that the perturbation is field aligned.
Furthermore a quantification of the level of similarity to a soliton is developed. Figure 5.23 shows synthetic toroidal profiles with clearly different toroidal peak width. The basic idea is that a larger number of Fourier components are necessary for the construction of peaks with a higher level of localization in the toroidal direction. *Toroidal solitariness* is defined as[15]

$$slt_{\phi} = \frac{\text{mean}(|FT_{\phi}(\delta B)|)}{\max(|FT_{\phi}(\delta B)|)}. \tag{5.4}$$

Figure 5.24 shows the histogram of slt_{ϕ} for all ELMs in discharge TCV42062, that met the conditions for an analysis as described in section 5.7. The extreme values of slt_{ϕ} are 0.24 and 0.60. For the ELMs with these two values toroidal profiles of δB and compensated absolute

[15] FT_{ϕ} means *Fourier transform with respect to the coordinate* ϕ.

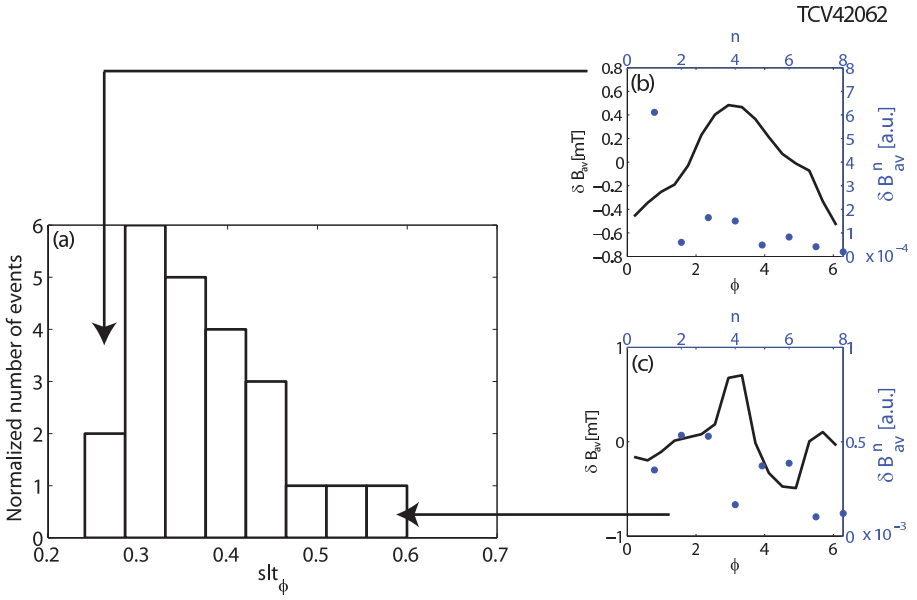

Figure 5.24: (a) Histogram of slt_ϕ for 23 ELMs in discharge TCV42062. For the ELM with (b) minimum and (c) maximum values of slt_ϕ: δB_{av} as a function of ϕ (black) and compensated absolute value of the Fourier coefficients (blue) (see figure 5.13).

values of the corresponding Fourier components are plotted in figure 5.24 as well. The ELM with the highest value of slt_ϕ has peaks with clearly smaller FWHM. However a toroidal region, which is unaffected by the perturbation can not be identified. Therefore a similarity to solitons is not observed for these ELMs.
In contrast to these TCV examples the situation is different for the magnetic perturbations during the ELM in discharge AUG25764 discussed in 5.7. It is recalled that this is one of the examples with the most dominant magnetic excursions. On the basis of the assumption that the perturbation is zero outside the observed toroidal range the reconstructed profile is necessarily confined to a certain toroidal range. However even if there would be more than one peak there is an unperturbed toroidal region (4rad to 5.5rad). Thus there is at least one toroidal region of significant size, which is not affected by the perturbation. The value of slt_ϕ

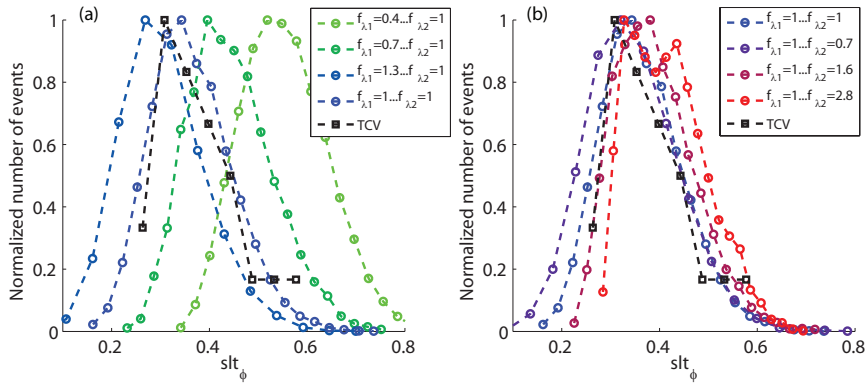

Figure 5.25: Normalized distribution of slt_ϕ for a number of model cases explained in further detail in the text (colors) and type I ELMs in discharge TCV42062 (black, mode number dependent radial decay compensated): (a) Variation of f_{λ_1}, (b) Variation of f_{λ_2}.

for this ELM is 0.89, which is about 50% higher than the highest value in the TCV discharge. In summary the investigated ASDEX Upgrade ELM is in contrast to the investigated TCV ELMs. The magnetic perturbation related to the ASDEX Upgrade ELM can be categorised as similar to a soliton and labeled as *solitary magnetic perturbation* (SMP).[16]

The discussion about similarity to solitons leads to another interesting question: Is there any effect (e.g. coupling) that enhances the number of ELMs with a high level of toroidal peaking or high solitariness compared to a random distribution? This question is connected to the one, is there an inherent tendency in the plasma edge to concentrate current in special locations. These questions are generalized to the one, if there are patterns in the distribution of Fourier components of the magnetic perturbations, which repeat from ELM to ELM, or if this is rather a random process. An attempt to answer these questions is made on the basis of experimental data from the discharge TCV42062.[17]
If the averaged toroidal profiles for two ELMs δB_1 and δB_2 are identical up to rotation by a toroidal angle φ, this is identical to the simultaneous fulfillment of following conditions for the Fourier coefficients a_n:

$$|a_{n,1}| = |a_{n,2}| \qquad \text{for all n} \tag{5.5}$$

$$\arg(a_{n,1}) = \arg(a_{n,2}) + n\varphi \qquad \text{for all n} \tag{5.6}$$

In a first step it is investigated, how random the composition of the absolute values of Fourier components is. The distribution of slt_ϕ in discharge TCV42062 is compared to corresponding distributions of sets of 10000 modeled toroidal profiles of δB. The absolute values of the toroidal Fourier coefficients of these modeled profiles are calculated as

$$|FC(n)| = a_1 e^{-f_{\lambda_1}\lambda_1 n} + 2\sqrt{3}a_2 e^{-f_{\lambda_2}\lambda_2 n} \cdot rnd.$$

The first and second term respectively represents the result of a fit on the distribution (over the ELM set) of the mean and standard deviation respectively of the absolute values of the Fourier coefficients as functions of n (compare figure 5.14 bottom right plot). rnd is a random number out of [-0.5;0.5] and f_{λ_1} and f_{λ_2} are modification factors.
By definition slt_ϕ is not sensitive to one or another n being dominant. It rather assess the ratios of absolute values of Fourier coefficients ignoring to which n they belong. Figure 5.25 shows that variation of the parameters f_{λ_1} and f_{λ_2} both leads to a shift of the distribution of slt_ϕ. The curve for $f_{\lambda_1} = 1$ and $f_{\lambda_2} = 1$ (blue) corresponding the original fit results has a remarkably good agreement with the experimental values. Thus the distribution of slt_ϕ can be explained by an n-dependent average and standard deviation of the absolute value of the Fourier coefficients only. The standard deviation seems to represent the variability in the starting conditions from ELM to ELM.
For the role of phase coupling equation 5.6 is transformed into $\arg(a_n) - \arg(a_1) \cdot n = \text{const}$ (for all $n > 1$ and both ELMs), where the constant is equal for both ELMs. Figure 5.26 illustrates histograms of these differences for the ELMs in discharge TCV42062 analyzed in section 5.7. For low values of n there are dominant peaks in the histograms but not for the

[16] In [122] a definition for *SMP* has been applied, that includes a much larger set of ELM associated perturbations, based on time traces of dB/dt at fixed toroidal positions. Accounting for the findings based on toroidal profiles of dB/dt described in section 5.7 this definition is revised towards a higher level of restrictiveness.

[17] Unfortunately the diagnostic situation does not allow to perform this analysis for ASDEX Upgrade, where in contrast to TCV solitary magnetic perturbations have been observed.

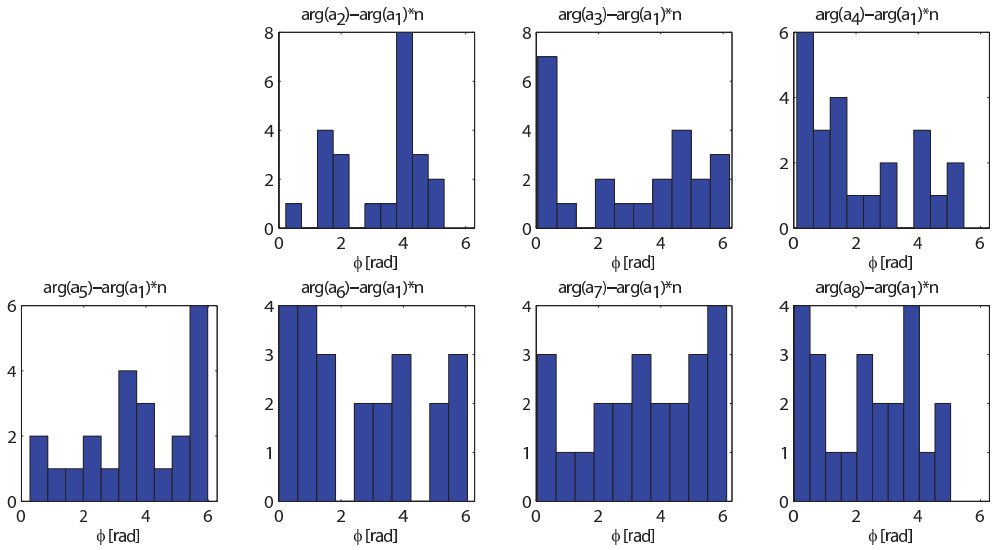

Figure 5.26: Histograms of phase differences $\arg(a_n) - \arg(a_1) \cdot n$ (n=2,...,8) for ELMs in discharge TCV42062 analyzed in section 5.7.

same value of the difference. Consequently phase coupling in the sense introduced above can not be proven.
In summary these investigations based on TCV data are consistent with two possible situations corresponding to intrinsic patterns in the distribution of Fourier components of magnetic perturbations:

a) There are intrinsic patterns, which are different as described by equations 5.5 and 5.6.
b) Apart from fixed mean values and standard deviations of the absolute values the distribution of Fourier coefficients of the magnetic perturbation as a function of n is random.

5.9 Temperature perturbation associated with dominant magnetic perturbations (ASDEX Upgrade)

In this section dominant magnetic perturbations are correlated to (radiation) temperature perturbations observed by ECEI. Figure 5.27 correlates the time derivative of the radial magnetic field and uncalibrated data from ECEI. Due to the application of diagnostic mapping it is possible to compare the propagation of a dominant magnetic excursion with the spatial-temporal evolution of the radiation temperature pattern. In both subplots a dashed line marks the trajectory of the central zero-crossing of a dominant magnetic perturbation with odd symmetry in the $t - \phi_{\mathrm{map}}$-space. Parallel and near to this line in figure 5.27(a), which shows ECEI data from inside the LCFS, a track of decreased radiation temperature can be observed. Assuming optical thickness, this could be interpreted as a temporary electron temperature reduction propagating in $\phi - \theta$-space on the same field line as the dominant magnetic perturbation. However the possibility can not be excluded, that the reduced radiation temperature is caused by a local density enhancement in excess of the critical density for X2-cutoff, located radially outside the probed position.

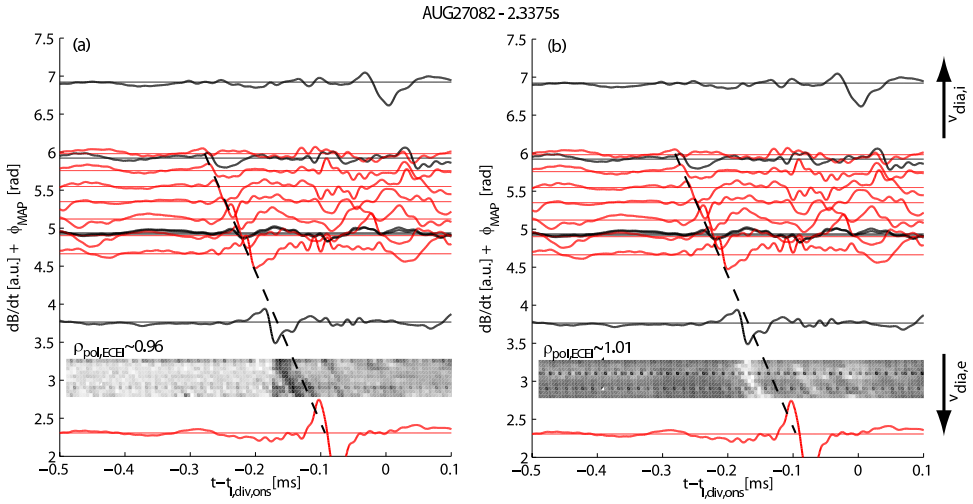

Figure 5.27: Correlation of time derivative of the radial magnetic field measured by two arrays (trajectories: color code indicated in figure 4.9) and uncalibrated data from ECEI (images) in discharge AUG27082: In both plots magnetic data are identical. ECEI data are taken from 11 channels measuring at different vertical but identical radial positions (black to white: cool to hot). These positions correspond roughly to the same poloidal flux: (a) $\rho_{\mathrm{pol}} \approx 0.96$, (b) $\rho_{\mathrm{pol}} \approx 1.01$. Dashed lines represent propagation of the perturbation.

Figure 5.27(b) shows ECEI data from channels with measurement positions just outside or at the LCFS for the same ELM. Here a significant temporary radiation temperature increase parallel and close to the dashed line is observed. It is recalled that the plasma is of marginal optical depth in this region. Thus it is not clear if the observed perturbation of radiation temperature is associated with an equivalent perturbation of electron temperature or if it is caused by a nonlocal effect. The described behavior at and inside the LCFS is not observed for each ELM. In many cases the phenomenology only inside or only outside the LCFS can be seen.
In [87] a coherent mode with around 18 peaks per toroidal turn appearing a few hundreds of μs before $t_{\mathrm{I,div,ons}}$ has been reported. It is important to note that for the ELM shown in figure 5.27 such a mode has not been observed.
In summary dominant magnetic perturbations are often observed to be associated with (radiation) temperature perturbations. In the presented example a decrease of the electron temperature slightly inside the LCFS in combination with an increase of radiation temperature slightly outside or at the LCFS correlated with a dominant magnetic perturbation has been observed. Thus there might be a flattening of the electron temperature profile correlated to the dominant magnetic perturbation. In principle this would be compatible with an island structure of the dominant magnetic perturbation.

5.10 Signatures before and after dominant magnetic perturbations (ASDEX Upgrade)

In order to obtain a maximum of information with respect to the linear and non-linear evolution of ELMs several ELM signatures are analyzed. Clearly dominant or even solitary

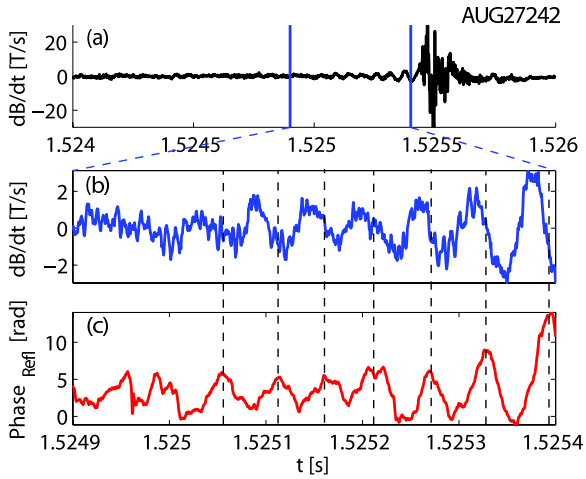

Figure 5.28: Type I ELM with coherent precursor in discharge AUG27242: (a) Trajectory of time derivative of the radial magnetic field acquired by probe B31-14. (b) Close up of a phase shown in (a). (c) Phase from frequency hopping reflectometer for the same time interval.

magnetic perturbations are at the center of the analysis presented in this work. Therefore cases, where these are observed, are used to correlate the magnetic perturbations to ELM signatures before and after.

5.10.1 Coherent ELM precursor activity

Coherent ELM precursors have been observed for type I and type III ELMs at various tokamaks [108, 109]. For many years they were not observed in any ASDEX Upgrade discharge in co-injection with type I ELMs. Recently they have been identified in such ASDEX Upgrade discharges, for cases with very low collisionality and very high core rotation (250-300km/s). Figure 5.28 shows time traces of the time derivative of the radial magnetic field and the phase observed by the frequency hopping reflectometer [123] for an ELM in one of these discharges (AUG27242). In a time interval of about 0.5ms before the dominant magnetic excursion, correlated oscillations at about 20kHz can be observed on these two diagnostics with a growth time of about 0.7ms. Such a growth time is significantly higher than typical ideal MHD growth times.
The frequency hopping reflectometer was used at a frequency corresponding to a density of $2.7 \cdot 10^{19}\mathrm{m}^{-3}$. In the pre-ELM density profile from Thomson scattering, such a density is typical for the steep gradient region with $0.95 < \rho_{\mathrm{pol}} < 1$. By application of a 1D model [123] the maximum displacement is estimated to be 3.8mm.
The detailed structure and location of the current perturbation causing the magnetic precursor activity will be the subject of another study. Here the only focus is on the relation of coherent precursor activity and dominant magnetic perturbations. Figure 5.29 shows magnetic perturbations during an ELM in discharge AUG27242. In the phase before $t_{\mathrm{I,div,ons}} - 0.12$ms the main activity belongs to a coherent precursor. The number of peaks per toroidal rotation of this mode can be extrapolated to $N_{\mathrm{dom}} = 9$. After $t_{\mathrm{I,div,ons}} - 0.12$ms a dominant magnetic perturbation can be observed. The typical oscillation frequency of the dominant magnetic perturbation ($\approx$ 75kHz) is clearly higher than that of the precursor ($\approx$ 20kHz). In contrast to the relation between edge snake and dominant magnetic perturbation shown in figure 5.17

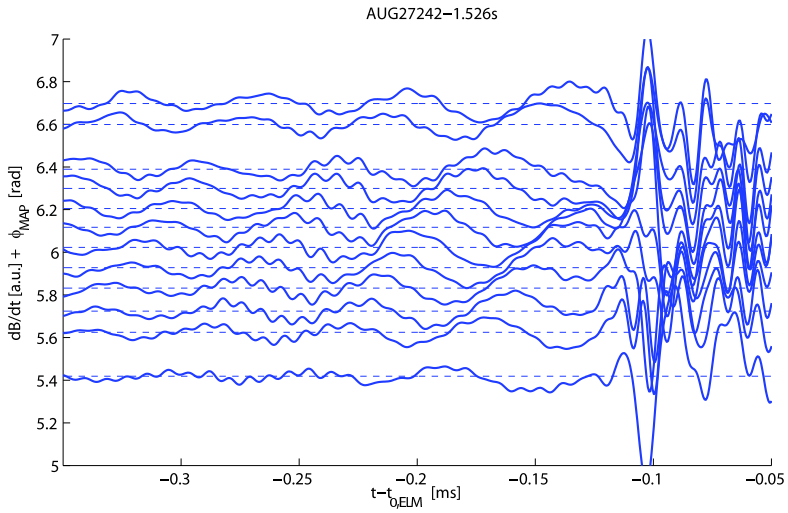

Figure 5.29: Time derivative of the radial magnetic field measured by various pick up coils (color code indicated in figure 4.9) displaced by the toroidal mapping target angle during ELMs in discharge AUG27242. In contrast to other figures of this type a low pass filter allowing to pass higher frequencies has been used: $f_{\text{pass}} = 120\text{kHz}$, $f_{\text{stop}} = 200\text{kHz}$.

the development from the precursor into the dominant magnetic perturbation is less like a smooth transition and more like a prompt onset of the dominant magnetic perturbation irrespective of the precursor activity. It is unclear, if after the onset of the dominant magnetic perturbation the precursor coexists with this for some time.
Taking into account these observations it is assumed that the coherent precursor and the dominant magnetic perturbations are either the signature of two distinct physics processes or that the transition from the first into the second is associated with a non-linear or even explosive process.

5.10.2 ELM filaments

The correlation of dominant magnetic perturbations and signatures of the non-linear evolution of ELMs is of special interest. Filamentary structures in the SOL are a feature of the fully developed non-linear phase of ELMs [37]. They can be observed with fast framing cameras [50], especially if appropriate gas puffing is applied.
In ASDEX Upgrade ELM filaments are less intensely observed if the Deuterium fueling is transferred from the main chamber port that the camera views to a port half a toroidal turn apart or to the divertor. Furthermore no ELM filaments are observed, if the gas puff is applied from the port in the camera view and a filter allowing for virtually no transmission of D_α- or D_β-light is used. This indicates that radiation from the ELM filaments is deuterium line-radiation.
Using view-gas-setting S_1 (table 4.1) ELM filaments in virtually the entire view appear. Figure 5.30 shows a filament with large parallel extension. Projections of field lines with $\rho_{\text{pol}} = 0.95$, 1.03 and 1.11 are shown as well. The filament appears to be well aligned with the magnetic field lines. It passes regions of high neutral density due to a gas puff in the foreground (1) and background (2), where a number of short radiation stripes can be seen above each other. In this view-gas-setting it is possible to trace the filament to the location

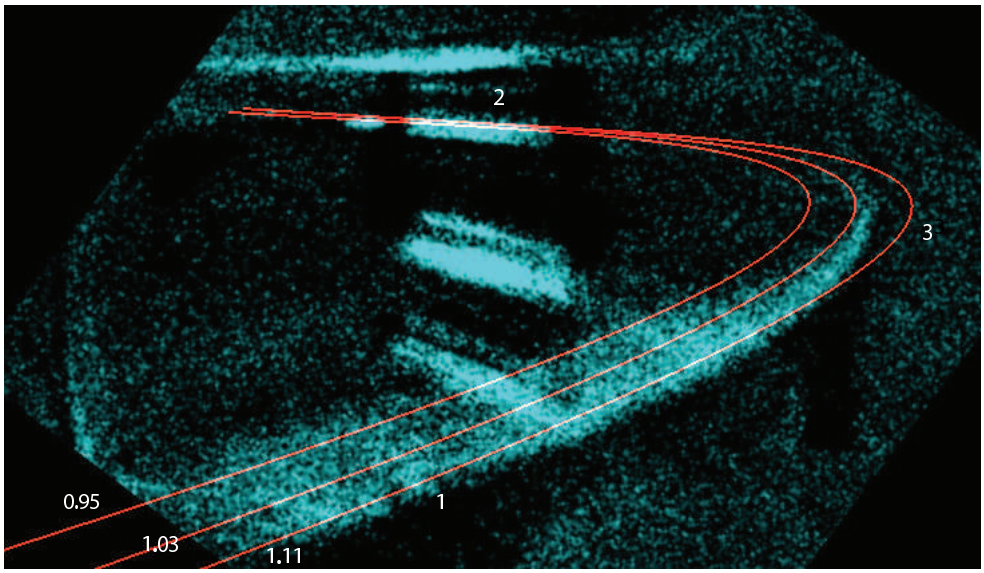

Figure 5.30: ELM radiation filament in discharge AUG26299 observed by fast framing camera. Projections of field lines on flux surfaces with $\rho_{\mathrm{pol}} = 0.95$, 1.03 and 1.11 are displayed in red.

where it has the maximum curvature in the projection (3). Comparison with the field line projections shows that in this region the filament is clearly localized radially outside the LCFS between $\rho_{\mathrm{pol}} = 1.03$ and 1.11. In the foreground (1) the radiation filament broadens. It can not be determined whether the origin of the radiation extends further in the poloidal or radial direction or both. Extension radially inside of the LCFS could be caused by neutrals due to the higher neutral pressure in the vicinity of the gas injection port. This would be also in line with the observation that filaments are sometimes visible in location (2) one or two frames before they appear in other areas (e.g. (3)).
Applying view-gas-setting S_2, the area in which filaments are observed corresponds well to the boundaries of the port (0.5m width, 1.0m height and 1.0m depth), which the gas reaches before entering the main chamber. It is therefore assumed, that in the volume in front of this port, in a fixed radial position, the neutral density is roughly homogeneous. Due to the reduced length of the filaments compared to the view-gas-setting S_1, it is not possible to determine if the filaments are located inside or outside of the LCFS. However, it seems natural to assume that for this view-gas-setting a part of the ELM filament radiation also originates in the SOL.
In discharge AUG26510 (view-gas-setting S_2) at 1.456s ELM filaments can be clearly observed in the area of the port through which the gas puff is made. The maximum relative radiation enhancement due to the filaments is 35%. Typical SOL values for the equilibrium electron density and temperature ($10^{19}\mathrm{m}^{-3}, 10\mathrm{eV}$) in combination with D_α-emission and a spatially homogeneous neutral density in front of the port are assumed. Under these conditions the observed increase in radiation could either be caused by an increase in temperature of about 7eV at constant electron density, a density increase of about $4 \times 10^{18}\mathrm{m}^{-3}$ at constant electron temperature or a combination of density and temperature increase. The latter is probably the case, as simultaneous increase of SOL electron density and temperature have been observed during ELMs before [124].
In order to capture the spatio-temporal evolution of the field aligned radiation structures a

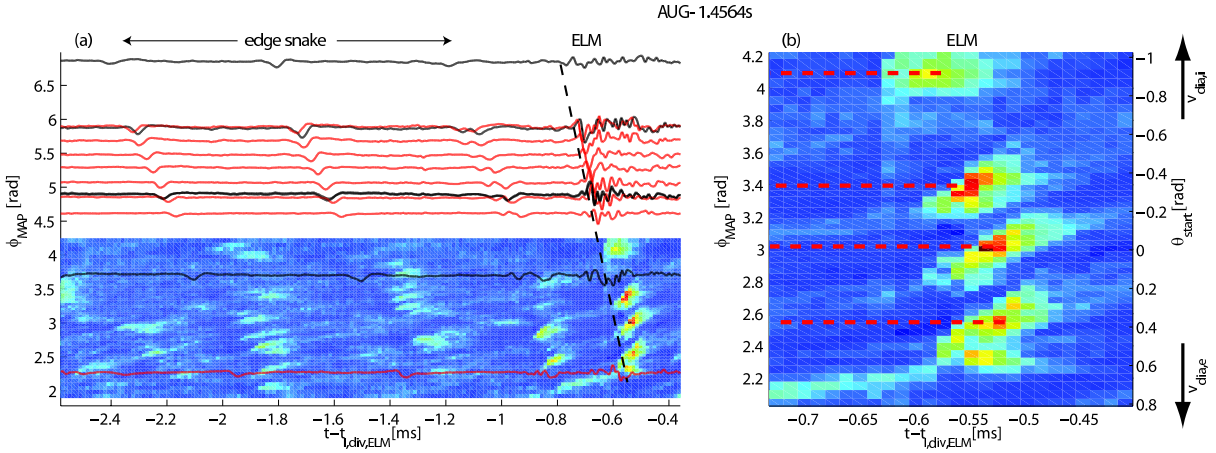

Figure 5.31: Evolution of filaments at 1.456s in discharge AUG26510: (a) Correlation of radial magnetic field (trajectories: color code indicated in figure 4.9) and data from fast framing camera processed as described in the text (image) in $t - \phi_{\text{map}}$-space. Dashed line represents propagation of an dominant magnetic perturbation. (b) Close up on processed data from the fast framing camera. Right axis provides the values of θ_{start}. Dashed lines indicate average mapping target angles at the time of the highest intensity.

special data processing approach has been developed. A 3D viewer [125] has been used to handle the projection from real space to camera chip. In a first step a chain of analysis points with constant values for ρ_{pol} and ϕ and an equidistant set of poloidal angles θ_{start} is defined. For each of the analysis points a field aligned chain of points with constant toroidal distances is also localized. Using the projection module all points are mapped onto the coordinate system of the camera chip. For each poloidal starting position θ_{start} of the analysis chain and each time the average radiation value over the field aligned chain is calculated. Also, for each point on the analysis chain the field line is traced to $\theta = 0$ as described in 4.5 to obtain the toroidal mapping target angle.

Figure 5.31(b) shows the obtained representation of the spatio-temporal evolution of the filaments during the ELM quoted above. Four propagating filaments can be identified. Detailed analysis of examples shows that the growth time of the peaks is clearly lower than their decay times. The radiation peaks propagate towards lower θ_{start} (i.e. downwards on the magnetic low field side). This means, that the filaments are moving in the ion diamagnetic drift direction, which is consistently observed at ASDEX Upgrade for ELMs with low to medium ELM frequencies.

The main trajectories for the three filaments observed in the area $-0.6 < \theta_{\text{start}} < 0.8$ are identified. The corresponding apparent poloidal angular velocity is on average 2.9krad/s. Multiplying these values by the minor radius gives an apparent poloidal rotation velocity of 1.4km/s.[18]

Sets of filaments as shown in figure 5.31(b) regularly appear within a short time interval. Here, the average mapping target angles at the time of the highest intensity for the four most intense structures are highlighted by dashed lines. The distance between the two uppermost filaments is nearly twice as high as for other neighbors. If the filament structure is transferred from a pedestal mode structure, one could speculate that one filament between the two top ones did not accelerate radially. Extrapolating the average distance in ϕ_{map} for

[18]The apparent perpendicular rotation velocity differs from this value by up to 3%.

the lower three filaments leads to 15 radiation peaks per full toroidal turn on the outer mid plane.
Due to the parametrization with the toroidal mapping target angle the evolution of dominant magnetic perturbations can be compared to that of the filaments, as shown in figure 5.31(a).[19] The radiation peaks are clustered in time in several sets. On the magnetic signals an edge snake can be traced from the start of the displayed time window propagating about 3 turns in the toroidal direction. At about -0.6ms this edge snake also leads into a dominant magnetic excursion, which propagates with clearly higher velocity. The propagation direction of the edge snake and the dominant magnetic perturbation is the electron diamagnetic drift direction, thus counter to the propagation direction of the radiation peaks.
The timing of the onset of the radiation peaks is clearly linked to the trajectory of the edge snake and dominant magnetic perturbation. During the dominant magnetic perturbation phase a tendency of filaments at lower ϕ_{map} to begin later can be clearly observed in figure 5.31(b). In figure 5.31(a) a dashed line following the onset of the dominant magnetic perturbation has been added. Except for the bottom filament the onset time of the radiation peak is well described by the passing time of this trajectory at a given location. Numerous ELMs are found with sets of filaments onsetting one after the other when, or shortly ($<$0.02ms) after, the same dominant magnetic excursion passes their location. During the edge snake phase the radiation features have lower distance in ϕ_{map} and lower velocities than during the ELM phase. There is a lag of the order of 0.1ms between the passing of the magnetic perturbation associated with the edge snake and the first observation of enhanced radiation in this position.
In a discharge pair (AUG26703, AUG26704) in upper single null configuration with an inversion of the toroidal magnetic field direction dominant magnetic perturbations still propagate in the electron diamagnetic drift direction and radiating filaments still move in the ion diamagnetic drift direction as in discharges with a magnetic field direction, which is standard at ASDEX Upgrade. In both discharges a number of examples are observed where a link between passing of a certain location by a dominant magnetic excursion and onset of a filament as described above can be identified.

[19] The evolution of $|I_{\mathrm{pol,sol,out}}|$ for this ELM consists in two rise phases separated by a short plateau phase. The automatic recognition of $t_{\mathrm{I,div,ons}}$ for this ELM has yielded the onset in the second rise phase. The onset in the first rise phase is about 0.55ms earlier.

Chapter 6

JOREK ELM simulation results

Understanding of the non-linear evolution of ELMs is highly desirable. Non-linear simulations with the code JOREK in combination with experimental observations can help in the development of such understanding. In this chapter an ELM simulation with the code JOREK is reviewed with respect to several aspects. In the first section the evolution of the magnetic perturbation energy will be presented. After that the evolution of the perturbation of poloidal magnetic flux and current in real space and Fourier space is reviewed in detail. In the fourth section synthetic magnetic signals are analyzed. In the last section the structure of the non-linear pressure perturbation and its relation to the perturbation of poloidal magnetic flux is discussed.

6.1 Evolution of perturbation energies

The overall evolution of the ELM simulation is captured by figure 6.1(a), which shows the evolution of volume integrated magnetic energies for several toroidal mode components.[1] After an initialization phase a period begins, in which each mode component is growing with a constant growth rate. Figure 6.1(b) (blue circles) shows that in this phase the $n = 10$ component is growing fastest with $\gamma \approx 2.0 \times 10^5 \mathrm{s}^{-1}$. During this phase the growth of the $n = 1$ component is at a very low level comparable to the $n = 0$ component.[2] At $t \approx 245\mu s$ the growth rate of the $n = 1$ component is increasing significantly making it the strongest growing component with $\gamma \approx 4.0 \times 10^5 \mathrm{s}^{-1}$ (figure 6.1(b) (red circles)), while the $n = 10$ component still has a growth rate as in the linear phase. The reason for this is seen in non-linear mode coupling [78, 126].
For numerical reasons it is not possible to simulate an entire ELM until the perturbation energies have decayed regarding components $n = 0, 1, 2, ..., 16$. The end of the time interval displayed in figure 6.1(a) is identical to the last time instance simulated. At this time there is an indication of saturation related decrease of growth rates in all mode components except $n = 0$. This saturation behavior is confirmed in other simulations. In the following sections the linear and the non-linear phase will be compared with respect to a number of aspects. For this the two times marked by vertical arrows in figure 6.1(a) will serve as representatives.

[1] The evolution of the kinetic energies largely corresponds to that of the magnetic energies.
[2] All growth rates quoted are growth rates of mode amplitudes.

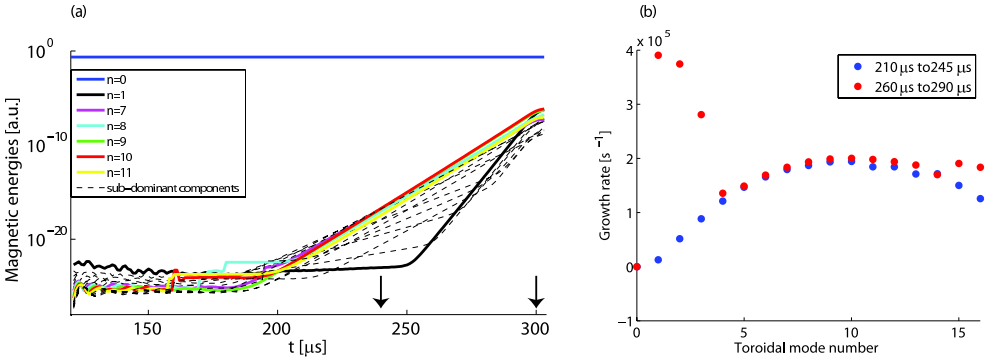

Figure 6.1: (a) Evolution of volume integrated magnetic energies for several toroidal mode components. The vertical arrows indicate times representing the linear and non-linear phases. (b) Growth rates of the mode components for two time intervals in the linear and non-linear phase.

6.2 Structure of the perturbations of poloidal flux and current density

The result of a JOREK simulation consists of a number of parameters (section 2.4) in three dimensional space, which have been evolved in time. In order to understand the main features of the evolution of the perturbations of poloidal flux and current during a JOREK simulation several projections of this result are presented.

Figure 6.2(a) displays the distribution of the poloidal perturbation flux $\psi^{\sim}$ on a surface of constant pre-ELM poloidal flux ($\rho_{\mathrm{pol}} = 0.97$). Peak trajectories can be observed, which extend about one toroidal turn. These trajectories in $\phi - \theta^*$-space are identified by a dedicated algorithm similar to the one used in chapter 5 for the identification of peak trajectories in TCV magnetic data. The algorithm starts at the position of the absolute maximum of $\psi^{\sim}$ on the flux surface. After this alternately a step in the toroidal direction and the search for the local maximum on the $\theta^* - \psi^{\sim}$-profile for this toroidal position is performed. The dots in figure 6.2 mark such a peak trajectory.

A structure, that is straight in $\phi - \theta^*$-space with an inverse inclination $d\phi/d\theta^*$ equal to the safety factor q on the flux surface can be interpreted to be aligned with the equilibrium magnetic field on the flux surface. The peak trajectory plotted as dots in figure 6.2(a) is not fully straight in $\phi - \theta^*$-space, but close to that. A linear regression on the positions found by the algorithm described above gives a fit quality[3] of 0.997. The inclination of the peak trajectory slightly diverges from the inclination of the equilibrium magnetic field (figure 6.2). From the outer mid plane ($\theta = 0$) to the bottom position ($\theta = \pi/2$) the relative phase within a structure of $n \approx 10$ of $\psi^{\sim}$ between these two trajectories changes by about 0.35π.

Figure 6.2(b) compares the distribution of poloidal flux along a peak trajectory with the surface average of $\psi^{\sim}$. The region, where the poloidal flux on the peak feature is higher than the surface averaged poloidal flux, corresponds to a bit more than one toroidal turn.

Figure 6.3 shows a horizontal section through a plane containing the magnetic axis. Here the poloidal perturbation flux in the outer mid plane dependent on toroidal and radial position is illustrated. $\psi^{\sim}$ has local maxima around $\rho_{\mathrm{pol}} \approx 0.95$. Corresponding to the profiles shown in figure 6.5 only in a restricted toroidal range there is a set of dominant peaks with toroidal

[3] Defined as $1 - \frac{\sum(\theta^* - \widehat{\theta^*})^2}{\sum(\theta^* - \overline{\theta^*})^2}$

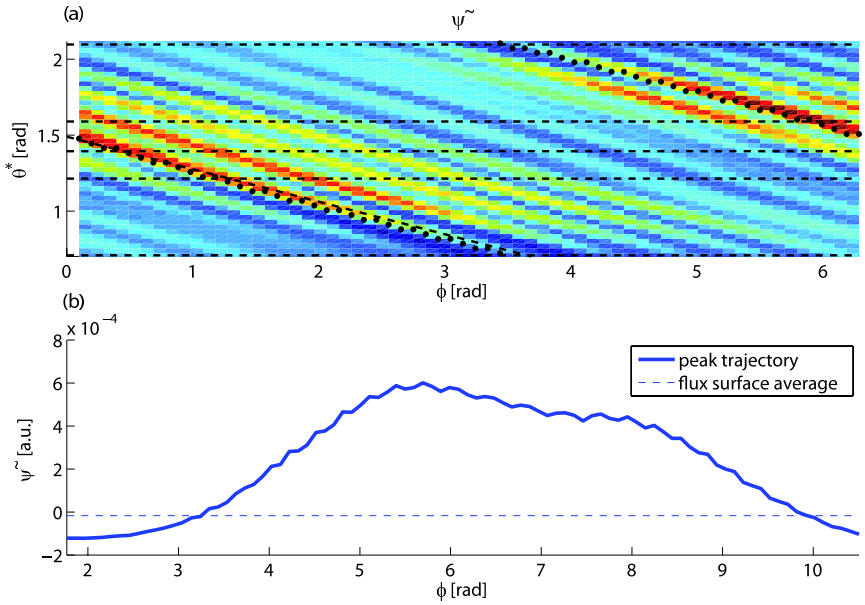

Figure 6.2: (a) Distribution of poloidal perturbation flux on flux surface with $\rho_{\mathrm{pol}} = 0.97$: Horizontal dashed lines indicate $\theta = -\pi/2, -\pi/4, 0, \pi/4, \pi/2$. The dots indicate the trajectory of a peak structure identified by the algorithm described in the text. The diagonal dashed line indicates the field line inclination on this flux surface. (b) Distribution of poloidal flux perturbation along a peak trajectory compared to the surface averaged poloidal flux perturbation. As parametrization for the direction along the peak feature the toroidal angle is used. For both plots the time $t = 300\mu$s in the non-linear phase of the JOREK simulation has been used.

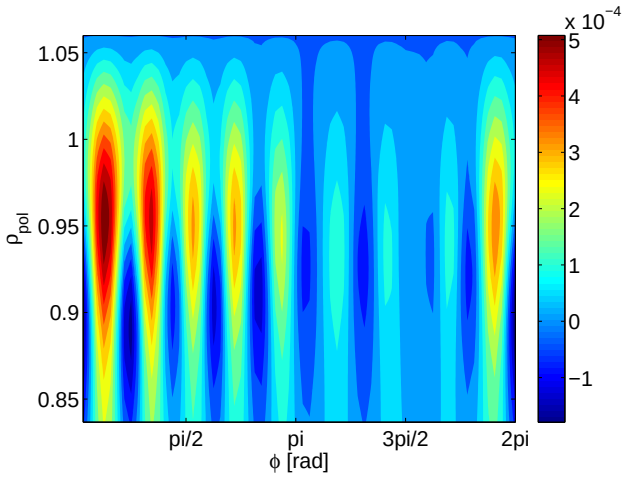

Figure 6.3: Poloidal perturbation flux $\psi^{\sim}$ as function of ϕ and ρ_{pol} for positions with $\theta = 0$ (outer mid plane) in the non-linear phase.

distance of neighbors equivalent to $n \approx 10$.
Another aspect to investigate is the variation of the perturbation with poloidal angle. This intensity is qualified by the standard deviation taken over a set of points with identical poloidal positions extending over a full toroidal turn. The variation of the standard deviation of ψ and j with θ is shown in figure 6.4. In all cases the highest amplitudes are reached at

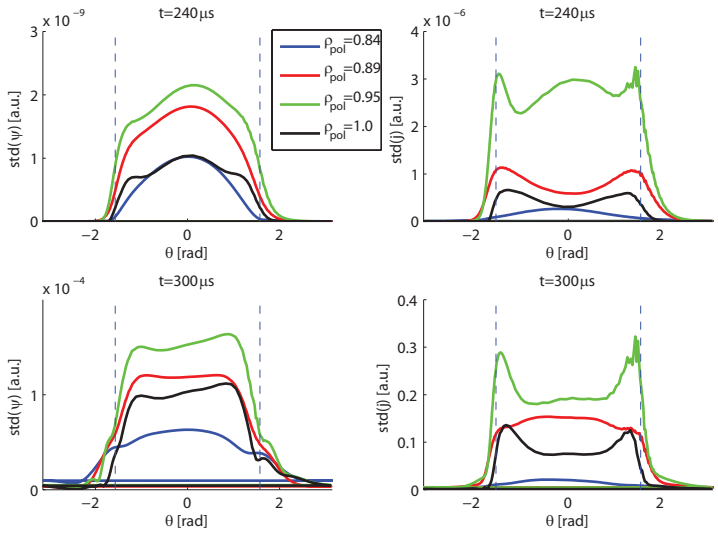

Figure 6.4: Variation of the standard deviation (taken over a set of points with identical poloidal positions extending over a full toroidal turn) of ψ (left) and j (right) with poloidal angle θ. Shown are plots for various radial positions (colors) and two times: $t = 240\mu$s (linear phase, upper row), $t = 300\mu$s (non-linear phase, lower row). The vertical dashed lines indicate $\theta = \pm\pi/2$.

$\rho_{\mathrm{pol}} = 0.95$. The poloidal extent of significant perturbations coincides well with the interval $[-\pi/2; \pi/2]$. For ψ in the non-linear phase the extent is increasing with decreasing radial position.
It is striking, that the largest values of std(j) are reached in the vicinity of $\theta = \pm\pi/2$. This feature is stronger pronounced in the non-linear phase. In the same phase ψ exhibits poloidal perturbation intensity profiles, which are flattened when compared to the ones in the linear phase. A simplified analytical model shows that strong peaks at $\theta = \pm\pi/2$ for j are consistent with flat profiles and no peaks at $\theta = \pm\pi/2$ for ψ as observed.

6.3 Toroidal perturbation spectrum of poloidal flux

Toroidal profiles of the poloidal magnetic flux perturbation and absolute values of the corresponding Fourier coefficients are illustrated in figure 6.5 for time instances in the linear and non-linear phase for two radial positions at the outer mid plane ($\theta = 0$). The profiles for both radial positions in the linear phase are virtually identical. In these profiles oscillation with $n \approx 5 - 10$ are dominant. In real space the perturbation extends over the full toroidal circumference with dominant peaks/dips around $\phi = 0$.
In the non-linear phase in the inner position the dominant mode numbers are $n \approx 9 - 10$. In contrast to that at the same time in the outer position, $n = 1$ becomes dominant with absolute values of the Fourier coefficients more than twice as high as all other components. Here also the components for $n = 2$ and $n = 3$ have clearly enhanced values. The corresponding toroidal profile has a number of dominant peaks in about half the toroidal circumference and only minor perturbations on the toroidally opposite side.
Information on the distribution of dominant mode components of ψ over the outer part ($0.7 \leq \rho_{\mathrm{pol}} \leq 1$) of the poloidal crossection is provided by figure 6.6. Figure 6.6(a) and (c)

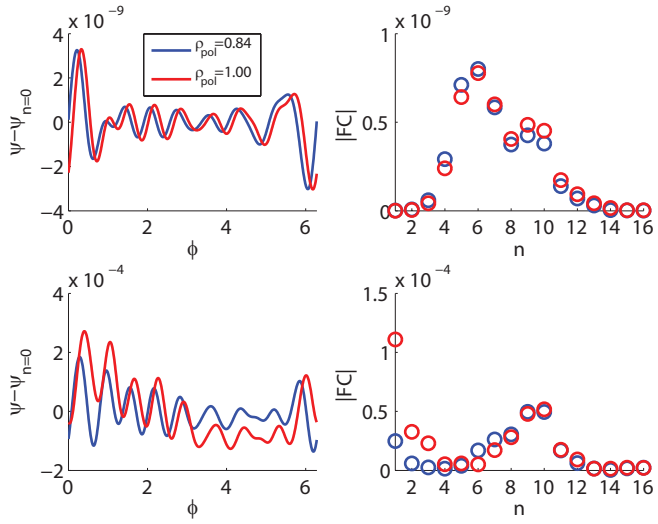

Figure 6.5: Toroidal profiles of the poloidal magnetic flux perturbation ($n = 0$-component subtracted) at $\theta = 0$ (left) and absolute values of the corresponding Fourier coefficients (right) for two radial positions ($\rho_{\mathrm{pol}} = 0.84$: blue and $\rho_{\mathrm{pol}} = 1.0$: red) and two times ($t = 240\mu$s: upper row and $t = 300\mu$s: lower row).

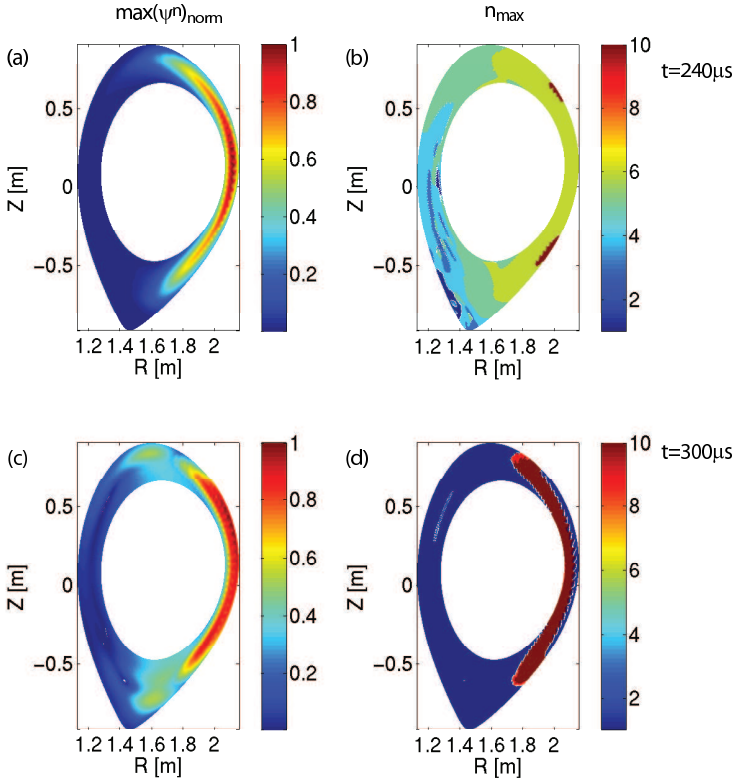

Figure 6.6: Distribution of normalized maximum absolute value of Fourier coefficient (left) and corresponding toroidal mode number (right) for $t = 240\mu$s (upper row) and $t = 300\mu$s (lower row). Data are shown for an annular region with $0.7 \leq \rho_{\mathrm{pol}} \leq 1$.

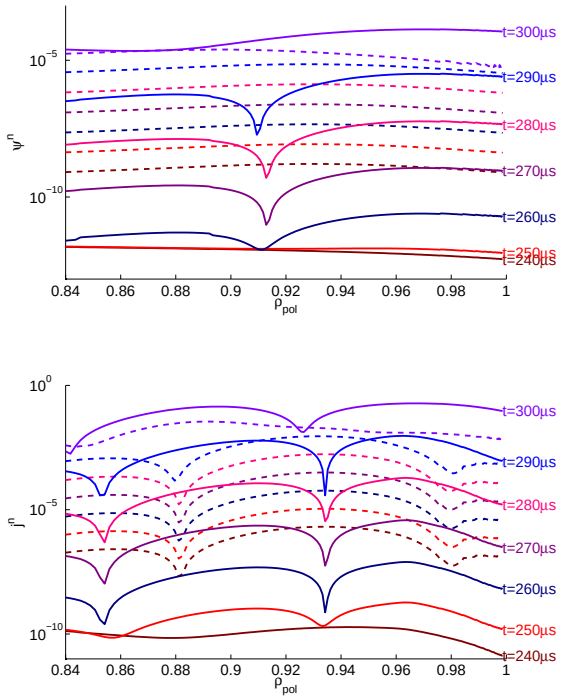

Figure 6.7: Radial profiles of absolute value of Fourier coefficient of (a) ψ and (b) j for positions corresponding to $\theta = 0$. Profiles are shown in each plot for a sequence of equally spaced time steps (colors) and for two toroidal mode numbers: $n = 1$ (solid line) and $n = 6$ (dashed line).

show the distribution of the normalized maximum absolute value of the Fourier coefficients for each position. The main perturbation in both phases is concentrated on the LFS. In the non-linear phase there is a moderate perturbation extending towards the top and bottom regions. The toroidal mode number $n_{\max}$ corresponding to the strongest component (figure 6.6(b) and (d)) is in the linear phase mainly 6 on the LFS and lower on the HFS. In contrast to that in the non-linear phase $n_{\max}$ is 10 in a region on the LFS, which is mostly not extending to the plasma edge. In the complementary region in this phase $n_{\max}$ is 1. Hence in the non-linear phase the local differences in $n_{\max}$ are more extreme.
Figure 6.7 shows radial profiles of the absolute value of Fourier coefficient of ψ and j for positions corresponding to $\theta = 0$. The sequence of times illustrated is equally spaced. Consequently the dominant development between subsequent points in time appears as an upward shift by a constant distance. Any deviation from this can interpreted as a change in the growth rate. Non-linear interaction is a possible reason for such a change. For the $n = 1$ component the most striking deviation from a constant upward shift is observed at the start and end of the displayed time sequence. These events can be correlated to kinks in the graph of the $n = 1$ magnetic energy (figure 6.1) at $t \approx 250\mu$s and $t \approx 300\mu$s.
In both plot dips can be observed at certain radial locations and certain times. The dips in the ψ^n-plot are in radial positions where the corresponding component has a phase jump of π when passing them radially. They only occur when $n = 1$ is still sub-dominant. For instance in the Poincaré plot corresponding to $t = 290\mu$s there is a modest stochastisation

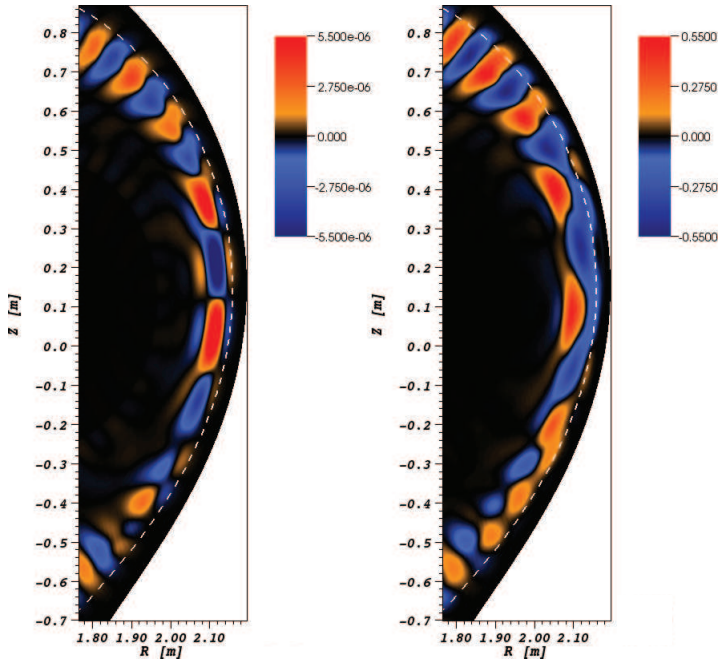

Figure 6.8: Distribution of toroidal perturbation current density for $t = 240\mu$s (linear phase - left) and $t = 300\mu$s (non-linear phase - right). The $n = 0$ components have been subtracted. The dashed line corresponds to the location of the pre-ELM LCFS. The figure has been adapted from [78].

in the entire range outside $\rho_{\text{pol}} \geq 0.85$, however at the position of the dips in the ψ^n-plot a dominant island can not be identified. Hence these features are interpreted as radial zero crossings of the individual mode components.
For both ψ and j at early times the $n = 6$ component is stronger, but the growth of the $n = 1$ component is faster. At $t = 300\mu$s (non-linear phase) the $n = 1$ component becomes stronger for both ψ and j over large radial ranges, especially at the plasma edge.
Figure 6.8 provides an impression of the influence of low toroidal mode numbers on the mode structure in real space. It displays the distribution of the toroidal perturbation current density for times in the linear phase and in the non-linear phase. In the linear ELM phase for $0.85 < \rho_{\text{pol}} < 1$ the toroidal perturbation current shows a poloidal chain of current tubes in alternating directions corresponding to a toroidal mode number of about 10. In the non-linear phase just inside the LCFS connections ('bridges') between three tubes with negative values of current density are observed. This new structure corresponds to a lower toroidal mode number. At the same time in the same poloidal range but closer to the plasma center a tendency of merging current tubes with positive direction can be observed.[4]

The evolution towards a dominant $n = 1$ structure in the non-linear phase might have also implications related to the saturation of the perturbation. In section 3.1.2 it has been shown that in the cylindrical case with an ideal conducting wall at $r = r_J$ and one poloidal mode component only the perturbation at the plasma edge ($r = r_P$) is damped by a factor $1-(r_P/r_J)^{2m}$. Taking dimensions comparable to ASDEX Upgrade leads to a damping factor of 56% for $m = 1$. In comparison damping of ELM associated perturbations by the ASDEX Upgrade vessel should be less intense, as the perturbation is considered to be concentrated

[4] An adapted colorbar is chosen to illustrate this.

to the outboard side due to its ballooning character. However in this location there is no big difference between toroidal and (local) poloidal mode number, as the local field line inclination $d\phi/d\theta$ is close to 1.
On the other side for JOREK it has been shown that the stabilising effect by the virtual ideal conducting wall (corresponding to the boundary condition on ψ) increases, if the distance between the LCFS and the domain boundary decreases [126]. The wall clearances in these simulations and in the one analyzed in the thesis at hand are clearly lower than in ASDEX Upgrade, which suggests that the stabilization effect is exaggerated in the JOREK calculation. It is also striking that in the JOREK simulation saturation happens very close to the time, when $n = 1$ becomes the dominant component, which is in line with the cylindrical model. Hence there might be a causal link in simulation and experiment between the $n = 1$ component becoming dominant and a temporary saturation of the perturbation.

6.4 Synthetic magnetic signals

As discussed in chapter 3 perturbations observed by magnetic probes in the experiment can be compared in the best way to JOREK results by employing a synthetic magnetic diagnostic as post processor. Figure 6.9 shows toroidal profiles of the normalized radial magnetic field evaluated by the post processing module SYNMAG and corresponding Fourier coefficients for a number of time steps. As in the case of the toroidal profile of ψ for the outer position displayed in figure 6.5 the $n = 1$ component becomes dominant in the non-linear phase. In the last time step displayed $n = 2$ and $n = 3$ are also among the strongest components.
The toroidal profiles do not show a similarity to solitons according to the criterion introduced in section 5.8. This is also the case for the poloidal magnetic flux before post processing (figure 6.5).
The synthetic diagnostic module SYNMAG described in chapter 3 has also a mode describing probes with realistic extension. Post-processing the same data in this mode does not change in a significant way the shapes of the graphs in figure 6.9.
Figure 6.10 shows the evolution of the synthetic radial magnetic field and its derivative during the time interval $270\mu\text{s} < t < 300\mu\text{s}$. It has to be noted that the flows in this JOREK simulation have significant deviations from typical experimental ones (section 5.6).[5] In figure 6.10(a) and (b) the perturbation structure coming up first has a toroidal mode number of about 8 to 10 (e.g. from $t = 280\mu\text{s}$ for dB/dt). Close to the end of the displayed time interval the perturbation gets a clear $n = 1$ component.
It is interesting to compare the earlier structure with the signature of precursors of type I ELMs observed in ASDEX Upgrade (subsection 5.10.1). The toroidal mode number in this phase in the JOREK calculation ($n \approx 8 - 10$) is similar to the number of peaks per toroidal turn observed in the experiment ($N_{\text{dom}} \approx 9$) . However in the time traces displayed in figure 6.10(c) the precursor oscillation is not visible, as is the case for the majority of experiments. In order to obtain synthetic signals exhibiting features comparable to the experimental precursors the ratio of growth rate and rotation frequency during this phase needs to be reduced.[6]

[5] In particular the radial shear of the perpendicular flow is considered to be not in good agreement with the experiment. This has several reasons. For instance, due to the MHD model diamagnetic drift is not featured.

[6] In another JOREK simulation with more realistic toroidal rotation the $n = 15$ component is dominant in the beginning of the saturation phase. Here the synthetic signals exhibit oscillations similar to the precursor

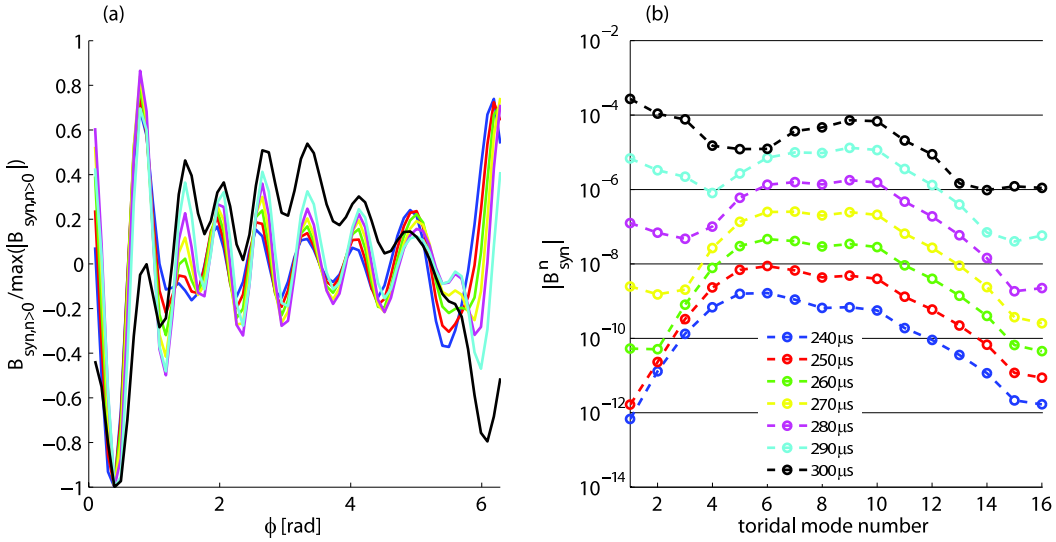

Figure 6.9: (a) Toroidal profiles of the normalized radial magnetic field ($n > 0$) evaluated by the post processing module SYNMAG for a number of time steps. (b) Absolute values of the corresponding Fourier coefficients. The magnetic field has been evaluated at the position of a probe from the high resolution poloidal array close to the outer mid plane. The legend provides the color code for the individual time steps. The synthetic diagnostic module has been run in the mode describing the probes as without extension.

In figure 6.10(c) after 290μs the perturbations reach their maximum (minimum) values. As indicated by the circles the peak values are reached later for higher toroidal angles (i.e. propagation in the ion diamagnetic drift direction). This phase is reminiscent of the growth of dominant magnetic perturbations observed in the experiment.

6.5 Relation of the perturbation of pressure and poloidal magnetic flux

The perturbation of the pressure is of special interest as it is regarded to be closely linked to the ELM size. On the other side the magnetic perturbation is in the focus of this work, as it is easier to be probed in various poloidal/toroidal locations. Therefore the relation of these two perturbations is important.
Figure 6.11 illustrates the distribution of pressure, poloidal flux and toroidal current density in dependence of ϕ and ρ_{pol} at fixed $\theta = 0$ (outboard mid plane) for times in the linear and non-linear ELM phase. In the linear phase the amplitude of the pressure perturbation is minor compared to the variation associated with the equilibrium pressure profile.[7] Hence no toroidal asymmetry of the pressure may be observed in figure 6.11. In contrast in the non-linear phase the radial pressure profiles strongly depend on the toroidal position. The structure of this perturbation may be described by the deformation of a line of constant pressure (black). In the unperturbed case this pressure corresponds to a location in the steep gradient region ($\rho_{\mathrm{pol}} \approx 0.97$). In the non-linear phase the radial position of this line

observed in the ASDEX Upgrade discharges with very high rotation and low collisionality.

[7] The pressure perturbation has a similar structure as the perturbation of poloidal flux (figure 6.5).

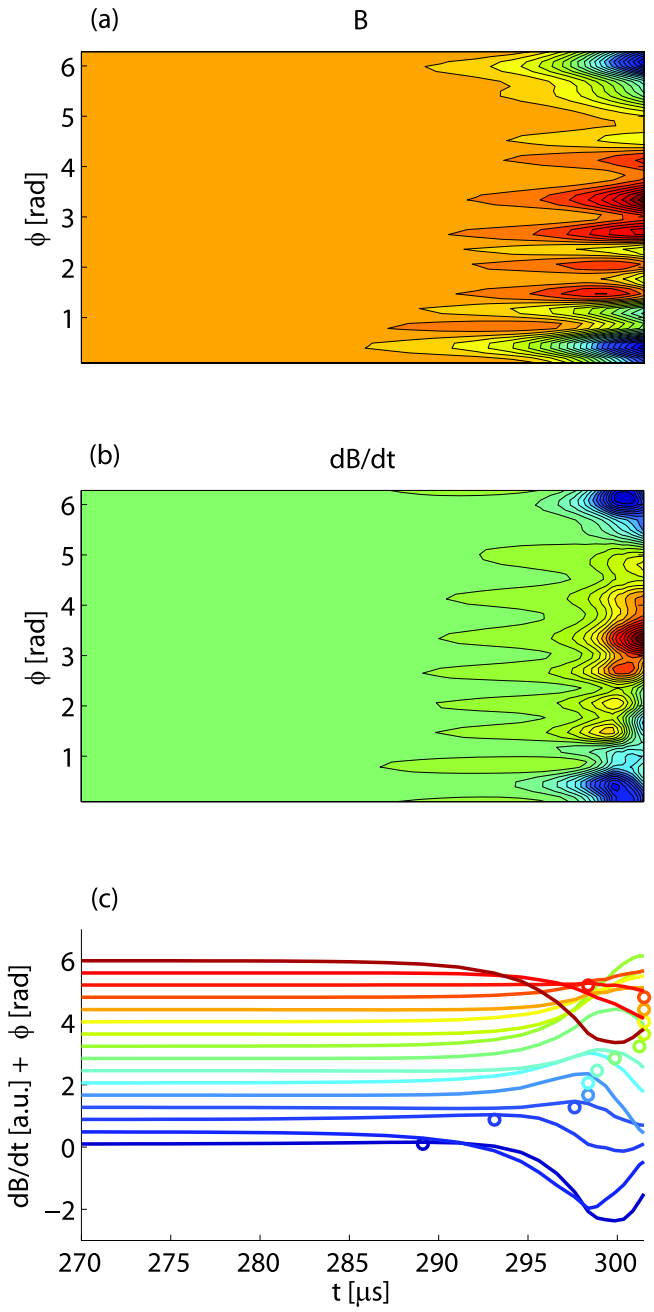

Figure 6.10: Evolution of synthetic signals: (a) Synthetic radial magnetic field as function of time and toroidal angle. (b) Synthetic time derivative of the radial magnetic field as function of time and toroidal angle. (c) Synthetic time derivative of the radial magnetic field vertically displaced by the toroidal angle as function of time. For each toroidal angle the time when the maximum values is reached is indicated by a circle. The synthetic diagnostic module has been run in the mode describing the probes as without extension.

shows oscillations with a toroidal distance of neighbors corresponding to $n \approx 10$. A structure corresponding to a single period of these oscillations could be labeled as a *finger*. The radial positions of both the inner and outer turning points of these oscillations have an $n = 1$ structure. The ranges of these are $0.90 \leq \rho_{\mathrm{pol}} \leq 0.96$ for the inner and $0.97 \leq \rho_{\mathrm{pol}} \leq 1.03$ for the outer radial turning point position. The level of pedestal pressure perturbation in the range $0 \leq \phi < \pi$ is significantly higher compared to $\pi \leq \phi < 2\pi$. The perturbation of poloidal flux is well correlated with the perturbation of the pressure.
There are several indications that the radial extent of the fingers in the experiment is smaller than in the JOREK calculation. This may be caused by the following aspects of the simulations: The plasma resistivity is taken larger than in the experiment due to computational limitations, which tends to increase structure sizes and suppresses turbulence. The plasma equilibrium used as an initial condition might be more unstable than in the experimental situation as, for instance, the pressure gradient profile required for the equilibrium reconstruction cannot be measured precisely. Stabilizing effects like diamagnetic drift or sheared plasma rotation are not taken into account in the simulations, which may increase the size of the structures formed by the instability.
However the pressure perturbation is in qualitative agreement to experimental results. In [127] electron density and temperature profiles have been analyzed at JET employing a high resolution Thomson scattering system. Four density profiles recorded during different phases of subsequent ELMs are shown. The position of the outermost channel measuring a density, which is significantly above zero, can vary by $\Delta\rho_{\mathrm{pol}} \approx 0.05$.
Figure 6.11 also shows the perturbation current density. In the non-linear phase there is virtually no current perturbation outside the LCFS. In particular there is no current perturbation associated with the pressure fingers extending beyond the LCFS. This again supports the hypothesis that the current perturbations associated with dominant magnetic perturbations are located inside the LCFS and that they are not due to filaments carrying current in the SOL (subsection 5.10.2).

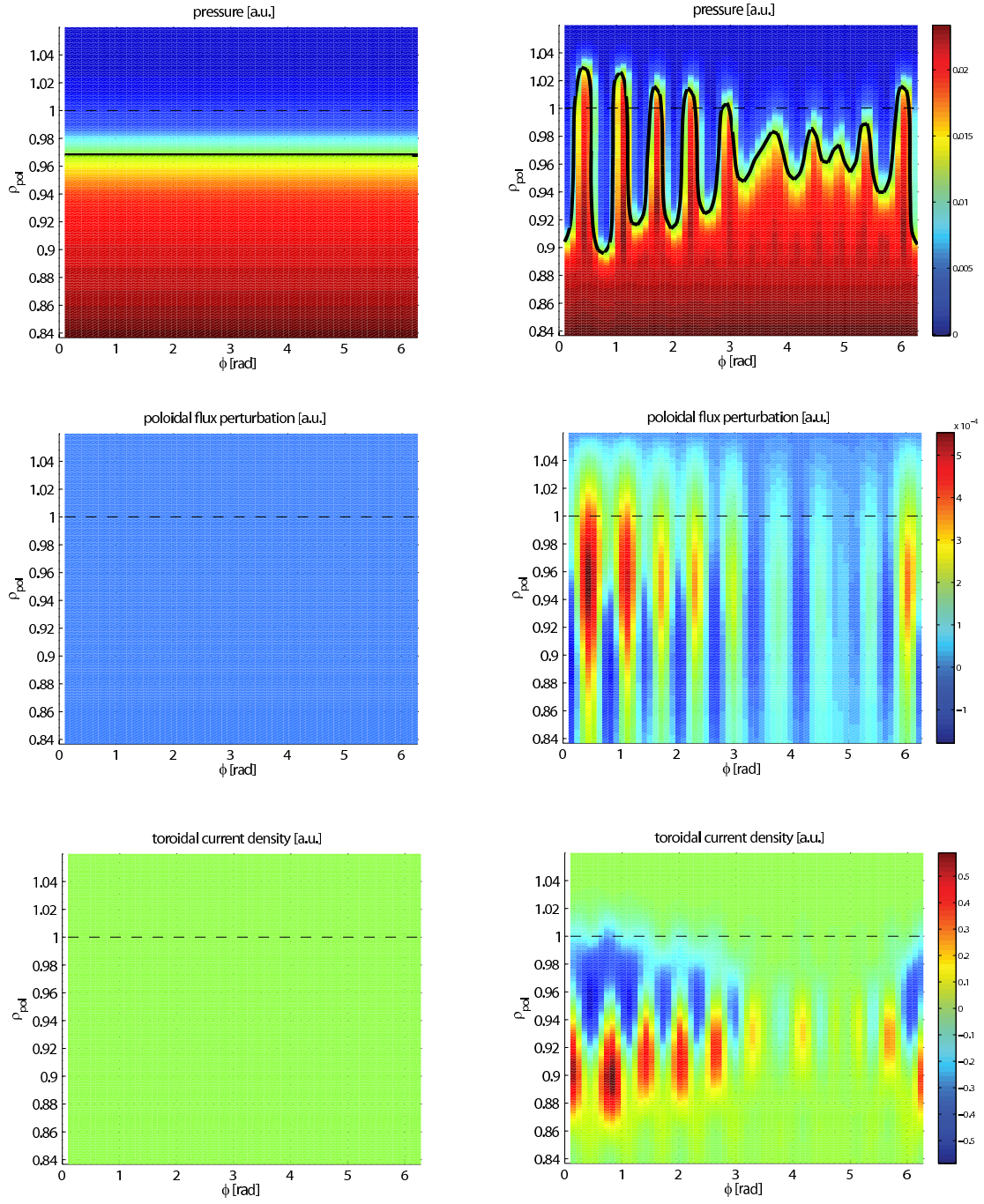

Figure 6.11: Distribution of quantities in dependence of ϕ and ρ_{pol} at fixed $\theta = 0$: pressure (upper row), poloidal flux perturbation (middle row) and toroidal current density perturbation (bottom row) in the linear phase (left: $t = 240\mu$s) and in the non-linear phase (right: $t = 300\mu$s). The location of the LCFS is indicated by a dashed line. In the pressure plots a contour line for $p = 0.014$ is superimposed in black.

Chapter 7

Summary and discussion

In this thesis perturbations associated with type I ELMs and in particular the non-linear phase of this instability have been investigated in detail. This has been done predominantly on the basis of data from experiments in ASDEX Upgrade and TCV and also JOREK simulations designed for ASDEX Upgrade. This chapter summarizes the main experimental results and central findings in the JOREK simulation. Subsequently on the basis of this various features and aspects of ELMs are discussed.[1]
In both experiments, dominant magnetic perturbations are observed by magnetic measurements temporally close to the onset of ELM associated divertor effects. Furthermore these perturbations are correlated to preceding and subsequent ELM signatures. Special attention is given to the relation of dominant magnetic perturbations and ELM filaments, as this provides information related to the process of crossing the LCFS by the perturbation. A number of selected experimental observations and results are listed here:

- In ASDEX Upgrade dominant magnetic perturbations appear in the last 0.2ms before the onset of divertor current and divertor D_α-radiation. Consistent with this they appear in TCV at the onset of D_α-radiation from main plasma and divertor. → section 5.2

- Comparison of dominant magnetic perturbations to magnetic fluctuations caused by passing current filaments lead to a heterogeneous result. During an ELM in ASDEX Upgrade the dominant magnetic perturbation can be either most consistent to the passing of a mono-polar current filament or of a bi-polar current filament or even of a multi-polar current filament. → section 5.3

- Dominant magnetic perturbations in both ASDEX Upgrade and TCV are going into saturation some hundreds of μs after exceeding the level of the background fluctuations. This is in clear contrast to a pure linear growth. → section 5.4

- The large majority of dominant magnetic perturbations in ASDEX Upgrade and all examples investigated for TCV propagate in the electron diamagnetic drift direction. → section 5.5

- The radial location of current perturbations leading to dominant magnetic perturbations in ASDEX Upgrade is investigated by a comparison of perpendicular velocities.

[1] As far as possible this discussion is ordered by the temporal order of appearance during the ELM.

The current perturbation is localized between the pedestal top or a bit further inside the plasma and the LCFS. → section 5.6

- Once the dominant magnetic perturbations in TCV have exceeded the background fluctuation level until reaching the maximum perturbation level, the toroidal shapes at all time instance are similar to each other (rigid mode-structure). This can only be explained by non-linear coupling of toroidal mode components. Hence linear magnetic perturbations can not be observed in TCV. It is natural to assume a similar situation for ASDEX Upgrade.[2] → section 5.7

- In TCV most frequently the dominant toroidal mode component of dominant magnetic perturbations is found to be $n = 1$. In the corresponding analysis the radial decay of perturbations, which depends on the local poloidal mode number, has been compensated in a way that the mode components at the LCFS position can be compared. As a dominant aliasing effect has been excluded the statement is valid for the range $1 \leq n \leq 15$. → section 5.7

- In the case of ASDEX Upgrade examples of perturbations with similarity to a soliton are found. In particular the toroidal perturbation structure shows regions of significant toroidal extent with negligible perturbation. The investigated TCV ELMs did not show such a similarity to a soliton. → sections 5.7 and 5.8

- Dominant magnetic perturbations are often observed to be associated with perturbations of the (radiation) temperature in a fixed position in the plasma. Both magnetic and temperature perturbations are propagating with a similar velocity in the same perpendicular direction. As the temperature is a flux surface quantity with an equilibration along field lines happening with the thermal velocity, such a behavior is expected to be associated with a deformation of a flux surface by a magnetic perturbation, which is observed by magnetic probes. → section 5.9

- Coherent ELM precursor activity has been observed for type I ELMs in a discharge with very high rotation and very low collisionality. In a certain time interval of the discharge they are observed prior to most dominant magnetic perturbations. For a special example a number of 9 peaks per toroidal rotation and a growth times of the order 1ms has been observed. Furthermore several observations lead to the assumption that coherent precursor activity and dominant magnetic perturbations are either the signature of two distinct physics processes or that the transition between them is associated with a non-linear or even explosive event. → subsection 5.10.1

- Application of diagnostic mapping enables the correlation of the evolution of dominant magnetic perturbations and ELM filaments, which are located at least partly in the SOL. In the lab frame both features propagate in opposite perpendicular directions, namely the electron (dominant magnetic perturbations) and the ion (ELM filaments) diamagnetic drift direction.

[2]Compared to TCV a significant diagnostic limitation is posed by the set of printed circuit probes at ASDEX Upgrade. Hence it is currently not possible to carry out a similar analysis for ASDEX Upgrade. However it seems possible to extend the toroidal array of printed circuit probes in ASDEX Upgrade to a level, which enables to investigate also the toroidal structure of dominant magnetic perturbations during ELMs.

It is also remarkable that the onset time of the radiation filaments is often well described by the time when a dominant magnetic perturbation passes the respective location.[3] One or few dominant magnetic excursions usually passes a number of locations from which filaments are observed to start. → subsection 5.10.2

Simulation data based on ASDEX Upgrade and obtained by the non-linear, reduced MHD code JOREK have been analyzed in detail. Particular attention has been given to the transition from the linear to the non-linear phase. To ensure an advanced level in comparability of data from experiment and JOREK simulations a post processing module (SYNMAG) is developed producing synthetic magnetic probe signals on the basis of JOREK simulations (chapter 3). SYNMAG compensates the JOREK boundary condition on the poloidal flux and introduces the effect of the main conducting structures in ASDEX Upgrade. In particular the ELM evolution in the simulation exhibits the following interesting features:

- The perturbation of the poloidal flux is poloidally confined to the outboard side ($-\pi \leq \theta \leq \pi$). In straight field line coordinates the peak trajectories of this perturbation are virtually straight. For a structure with $n \approx 10$ this peak trajectory accumulates from the outer mid plane to the bottom position a phase deviation relative to a field line of about 0.35π. → section 6.2

- The toroidal structure of the synthetic signals is in all phases clearly non-harmonic. However a similarity to a soliton (i.e. a toroidal region with negligible excursions) is not observed. → section 6.4

- The toroidal structures of the poloidal flux perturbation and of the synthetic magnetic signals have been analyzed with respect to dominant mode components. The synthetic magnetic signals show a qualitatively identical behavior as the poloidal flux at the plasma edge: While in the linear phase $n = 6$ is dominant, in the non-linear phase this is the case for $n = 1$.
  In the non-linear phase shortly before $n = 1$ becomes dominant the synthetic magnetic field is still dominated by a component with a higher toroidal mode number ($n \approx 8 - 10$). → sections 6.3 and 6.4

- In the non-linear phase correlated to the perturbation of poloidal magnetic flux a strong edge pressure perturbation consisting of radially extending fingers ($n \approx 10$) is observed. Around the outer mid plane these fingers extend both deeper inward into the pedestal region and outward into the SOL region in a given toroidal position when compared to the toroidally opposite position ($n = 1$ modulation). Thus there is a 3D-asymmetric pedestal erosion during the non-linear phase that differs significantly from the classical linear ballooning picture. → section 6.5

- Also in the non-linear phase the current perturbation outside the LCFS is negligible. → section 6.5

Under certain conditions in ASDEX Upgrade **coherent ELM precursors** are observed before dominant magnetic perturbations. Their growth times are significantly longer than

[3]The dominant magnetic perturbation and the filament are field aligned structures. In this context 'passing' means that the corresponding field lines are passing each other at this time in $\phi - \theta$-space.

typical ideal MHD growth times, which suggests non-linearity or resistive effect being involved.[4] In JOREK the synthetic radial magnetic field shows in the non-linear phase before $n = 1$ becomes dominant a dominant toroidal mode number ($n \approx 8-10$) similar to the number of peaks per toroidal turn for precursors of type I ELMs ($N_{\mathrm{dom}} \approx 9$). In combination this motivates the hypothesis that coherent ELM precursor activity is observed during a phase when the perturbation (a) has grown to an observable amplitude, (b) still has dominant large toroidal mode numbers ($n \geq 6$) and (c) has a high perpendicular rotation frequency.

Dominant magnetic perturbations with a **similarity to solitons** are observed in ASDEX Upgrade but not in TCV.[5] Furthermore there is no similarity to solitons in the toroidal structure of perturbation in the JOREK simulation. This might be explained by the fact that solitary magnetic perturbations at ASDEX Upgrade are not observed under all conditions, but they are observed more frequently with decreasing collisionality [122]. The relevant low collisionality range is not accessible for TCV and it is lower than the collisionality in the analyzed JOREK simulation.
As well as these solitary magnetic perturbations during ELMs in ASDEX Upgrade there are other H-mode edge instabilities featuring magnetic perturbations with similarities to solitons. Among these are the edge snake (subsection 5.3.1), the palm tree mode [105] and the outer mode [106]. This motivates the hypothesis that under certain circumstances there is an inherent tendency to concentrate current density in the plasma edge around single field lines. A first investigation for TCV does not find a clear indication supporting this hypothesis (section 5.8). However this might be different, when repeating such an analysis with solitary magnetic perturbations (e.g. measured at ASDEX Upgrade with an upgraded magnetic diagnostics) and/or with another criterion to uncover such a tendency.

In the JOREK simulation a **transition towards low dominant toroidal mode numbers** ($n = 6 \rightarrow n = 1$) from the linear to the non-linear phase has been observed in the plasma edge perturbation and synthetic probe signals. This is consistent with the observation that at TCV the dominant toroidal mode number of dominant magnetic perturbations is most frequently $n = 1$. Furthermore this is in line with a KINX calculation for another but comparable TCV discharge, which close to the operational point shows highest growth rates for $n > 10$. In summary there are various indications that for type I ELMs higher toroidal mode numbers are dominant in the linear phase compared to stages in the non-linear phase, when the low n components have grown sufficiently (table 7.1). The question was raised, whether the interaction between this low n perturbation and the conducting wall leads to a temporary saturation of the perturbation.
The JOREK simulation results may also be compared to observations of the ELM structure in ASDEX Upgrade after transition across the equilibrium LCFS by significant amounts of plasma. Investigations by Thomson scattering [100] have been extrapolated to 10 to 20 blobs per toroidal rotation. Measurements from divertor infrared thermography [49] show 8 to 20 peaks per toroidal rotation. As both of these techniques are based on the toroidal distance of neighboring peaks, they are not suitable to capture components associated with lower toroidal mode numbers, even if these are dominant. For instance an enhancement of the magnetic diagnostic in ASDEX Upgrade would enable to resolve an $n = 1$ structure. On the other hand sub-dominant structures corresponding to about 10 peaks per toroidal rotation

[4] The large growth times of ELM precursors remain to be explained.
[5] For ASDEX Upgrade a much larger set of discharges has been analyzed compared to TCV.

Table 7.1: Overview of dominant toroidal mode components from several investigations

		linear phase	non-linear phase
Experiment	TCV	-	most often $n = 1$
Simulations	KINX for TCV	$n > 10$	-
	JOREK for ASDEX Upgrade (plasma edge and probes)	$n = 6$ (240μs)	$n = 1$ (300μs)

are observed in the non-linear phase in the JOREK simulation (section 6.5). Furthermore it is important to have in mind that JOREK's limits of reproducing the experiment are clearly reached (e.g. due to an inadequate representation of the edge rotation shear), when it comes to the ejection of material outside the LCFS.
A basic 0D-model to explain the $n = 1$ component to catch up and finally dominate as observed in the JOREK simulation is provided in [126]. Here the evolution of energies in the mode components is described by a superposition of exponential growth (i.e. energy transfer from the $n = 0$ component) and non-linear interaction (i.e. energy transfer from components with $n > 0$). The evolution of the energies of the mode components in the basic model and in JOREK shows good agreement.
The evolution of toroidal mode numbers might even explain the relatively large losses of energy routinely observed during type I ELMs, which are almost comparable to little disruptions. Linear calculations clearly show that modes with low toroidal mode numbers are more global. They extend more towards the plasma center when compared to modes with higher toroidal mode numbers (subsubsection 2.2.2.3).[6] If there is also such a structural difference in a non-linear situation, the low n components could lead to erosion of temperature and density from areas further inside.

Diagnostic mapping enables the **dominant magnetic perturbations and ELM filaments** observed in ASDEX Upgrade to be placed on the same coordinate system. The finding that both features propagate in different perpendicular directions can be understood with regard to the radial location and type of the perturbations. Dominant magnetic perturbations, which originate from between LCFS and pedestal top, rotate with the local $\boldsymbol{E} \times \boldsymbol{B}$-velocity (in the electron diamagnetic drift direction) plus a certain phase velocity (section 5.6). In contrast, ELM filaments rotate with the local $\boldsymbol{E} \times \boldsymbol{B}$-velocity in the SOL, which is directed in the ion diamagnetic drift direction. This difference in propagation directions may also be compared to the finding of an abrupt reversal of perpendicular velocity of coherent structures observed by Langmuir probes close to the LCFS [128].
Furthermore the difference in the propagation direction clearly shows that the dominant magnetic perturbations can not be explained by a current carried by the observed filaments. This is consistent with the observation of virtually no current perturbation outside the LCFS in the JOREK simulation.
The frequent observation of the onset of radiation filaments where and when a dominant magnetic excursion passes is of high interest. It suggests that the perturbation flux corresponding to dominant magnetic excursion, alone or in combination with another deviation from the equilibrium, provides conditions under which radiation filaments can propagate radially. This is fully consistent with the fingers observed in the JOREK predictions. They have the maximum extension into the SOL in the toroidal position, where the perturbation

[6] Low n modes also have a larger poloidal extension compared to high n modes.

of poloidal flux is highest (figure 6.11).

A central element of the work presented in this thesis is the detailed characterization of dominant magnetic perturbations during ELMs. In particular the non-linear evolution and the 3D structure of these events, which on ASDEX Upgrade sometimes show similarities to solitons, have been investigated. Starting from dominant magnetic perturbations their relations to earlier and later ELM features like coherent ELM precursors and ELM filaments respectively are analyzed. The results gathered in the framework of this thesis enable the development of a picture of the processes during ELMs, which is more complete than any before. It is expected that this will contribute to an extended understanding of ELMs and methods to mitigate them and to an ELM model, which is capable of reliably predicting ELM sizes and evolution.

Appendix A

Background information on the synthetic magnetic diagnostics

A.1 Derivation of a modified version of Green's second identity

The operator $\triangle^*$ and the Laplace Operator can be written in cylinder coordinates (R, Z, ϕ)

$$\begin{aligned} \triangle^* &= -\frac{1}{R}\frac{\partial}{\partial R} + \frac{\partial^2}{\partial R^2} + \frac{\partial^2}{\partial Z^2} \\ \triangle &= \frac{1}{R}\frac{\partial}{\partial R} + \frac{\partial^2}{\partial R^2} + \frac{\partial^2}{\partial Z^2}. \end{aligned} \tag{A.1}$$

It can be shown that

$$\triangle^* f = R\left(\triangle - \frac{1}{R^2}\right)\left(\frac{f}{R}\right). \tag{A.2}$$

Applying this identity and Green's second identity gives

$$\begin{aligned} &\int_\Omega \frac{1}{R^2}(u\triangle^* v - v\triangle^* u)d\Omega = \int_\Omega \frac{1}{R}\left[u\left(\triangle - \frac{1}{R^2}\right)\frac{v}{R} - v\left(\triangle - \frac{1}{R^2}\right)\frac{u}{R}\right]d\Omega = \\ &\int_\Omega \frac{u}{R}\triangle\frac{v}{R} - \frac{v}{R}\triangle\frac{u}{R}d\Omega = \int_\Gamma \frac{u}{R}\frac{\partial}{\partial n}\left(\frac{v}{R}\right) - \frac{v}{R}\frac{\partial}{\partial n}\left(\frac{u}{R}\right)d\Gamma = \int_\Gamma \frac{1}{R^2}\left[u\frac{\partial v}{\partial n} - v\frac{\partial u}{\partial n}\right]d\Gamma. \end{aligned} \tag{A.3}$$

Inserting $d\Omega = 2\pi dRdZ$ and $d\Gamma = 2\pi\sqrt{dR^2 + dZ^2} = 2\pi Rds$ leads to the modified version of Green's second identity:

$$\int_\Omega \frac{1}{R}(u\triangle^* v - v\triangle^* u)dRdZ = \int_\Gamma \frac{1}{R}\left[u\frac{\partial v}{\partial n} - v\frac{\partial u}{\partial n}\right]ds \tag{A.4}$$

A.2 Alternative derivation of the no-wall solution

Equation 3.33 can be derived in more formal terms using the version of Green's second identity adapted for the operator $\triangle^*$ (appendix A.1). Set u equal to ψ_{JE} on Ω_J

$$\begin{aligned} \triangle^*\psi_{JE} &= -g(R, Z), \\ \psi_{JE} &= 0 \; on \; \partial\Omega_J \; . \end{aligned} \tag{A.5}$$

Set v equal to Green's function $G(\boldsymbol{r}, \boldsymbol{r}^*)$ as introduced above

$$\triangle^* G(\boldsymbol{r}, \boldsymbol{r}^*) = -R\delta(R - R^*)\delta(Z - Z^*). \tag{A.6}$$

Now the identity turns into

$$\begin{aligned} &\oint_{\Omega_J} \frac{1}{R^*} \left[\psi_{JE}(\boldsymbol{r}^*)(-R\delta(R - R^*)\delta(Z - Z^*)) - G(\boldsymbol{r}, \boldsymbol{r}^*)(-g(R^*, Z^*))\right] dR^* dZ^* = \\ &\oint_{\partial\Omega_J} \frac{1}{R^*} \left[\psi_{JE}(\boldsymbol{r}^*) \frac{\partial G(\boldsymbol{r}, \boldsymbol{r}^*)}{\partial n^*} - G(\boldsymbol{r}, \boldsymbol{r}^*) \frac{\partial \psi_{JE}(\boldsymbol{r}^*)}{\partial n^*}\right] ds^*. \end{aligned} \tag{A.7}$$

With equations 3.31 and A.5 this turns into

$$-\psi_{JE}(\boldsymbol{r}) + \psi_V(\boldsymbol{r}) = 0 - \oint_{\partial\Omega_J} \frac{1}{R^*} G(\boldsymbol{r}, \boldsymbol{r}^*) \frac{\partial \psi_{JE}}{\partial n} ds^*. \tag{A.8}$$

This identity is still valid, if $\boldsymbol{r}$ is in $\Omega_A \setminus \Omega_J$ ψ_{JE}. Therefore the last equation is equivalent to equation 3.33.

A.3 Test of of the no-wall solution with the analytical model

Although the validity of the no-wall solution has been demonstrated from first principles, it is helpful to reconstruct this solution in the framework of the analytical model developed in section 3.1. To do this a first look at the differential equation (operator Δ) for this system is taken. As mentioned in section 3.1 Ampère's law has the z-component:

$$-\triangle\psi = \frac{1}{r}\left[\frac{\partial}{\partial r}(-r\frac{\partial \psi}{\partial r}) - \frac{\partial}{\partial \theta}(\frac{1}{r}\frac{\partial \psi}{\partial \theta})\right] = \mu_0 j_z. \tag{A.9}$$

For this case a similar formula to equation 3.33 has to be derived. Inserting the two functions ψ_{JE} defined on $R = \{(r, z) | r \leq r_J\}$

$$\begin{aligned} \triangle\psi_{JE} &= -g(r, z), \\ g(r, z) &= \mu_0 j_z, \\ \psi_{JE} &= 0 \ on \ \partial R \end{aligned} \tag{A.10}$$

and Green's Function G defined on R

$$\begin{aligned} \triangle G(\boldsymbol{r}, \boldsymbol{r}^*) &= -\delta(|\boldsymbol{r} - \boldsymbol{r}^*|), \\ \psi_V(\boldsymbol{r}) &= \int_R G(\boldsymbol{r}, \boldsymbol{r}^*) g(\boldsymbol{r}^*) dR \end{aligned} \tag{A.11}$$

into Green's second identity and using some known properties of the functions yields[1]

$$\begin{aligned} \int_{R\times L} \psi_{JE}\triangle G - G\triangle\psi_{JE} dV &= \oint_{\partial R\times L} \psi_{JE}\frac{\partial G}{\partial n} - G\frac{\partial \psi_{JE}}{\partial n} dS, \\ \int_{R\times L} \psi_{JE}(-\delta) - G(-g) dl dr dz &= \oint_{\partial R\times L} 0 - G\frac{\partial \psi_{JE}}{\partial n} dl ds, \\ \psi_V &= \psi_{JE} - \oint_{\partial R} G\frac{\partial \psi_{JE}}{\partial n} ds. \end{aligned} \tag{A.12}$$

[1] L is the length of the cylinder.

This equation for flux functions can be turned into a corresponding equation for magnetic fields. Applying the operators $-1/r\ \partial/\partial\theta$ and $\partial/\partial r$ together with the commutativity of derivation and integral turns ψ_V and ψ_{JE} into the related poloidal magnetic field and consequently Green's function G expressing the poloidal flux into a Green's function expressing poloidal magnetic field

$$\boldsymbol{B}_V = \boldsymbol{B}_{JE} - \oint_{\partial R} \boldsymbol{G} \frac{\partial \psi_{JE}}{\partial n} ds. \tag{A.13}$$

Note that for the description of the surface current in the integral still the flux function is used. $\boldsymbol{G}$ is the magnetic field of a straight unit[2] current filament in the z-direction through the point (x^*, y^*) at a position (x, y), which can be expressed in Cartesian coordinates as

$$\boldsymbol{G}(x, y, x^*, y^*) = \frac{1}{2\pi R} \frac{1}{R} \begin{pmatrix} y - y^* \\ x^* - x \\ 0 \end{pmatrix} \text{ with } R = \sqrt{(x - x^*)^2 + (y - y^*)^2}. \tag{A.14}$$

For the evaluation of the surface current term the normal derivative of ψ_{JE} from inside at $r = r_J$ has to be taken. ψ_{JE} is given in subsection 3.1.2 by

$$\begin{aligned} \psi_{JE} &= (f_V(r) + f_{WJ}(r)) \cos(m\theta), \text{ where} \\ f_{JE}(r) &= \begin{cases} c r_P^{2+m} (r^{-m} - r_J^{-2m} r^m) & \text{for } r_P \le r \le r_J \\ 0 & \text{for } r > r_J \end{cases} \\ c &= \frac{\mu_0}{(2+m)2m}. \end{aligned} \tag{A.15}$$

This gives for the normal derivative

$$\begin{aligned} &\frac{\partial \psi_{JE}}{\partial n}|_{r=r_J} = \nabla \psi_{JE} \cdot \boldsymbol{n}|_{r=r_J} = \frac{\partial \psi_{JE}}{\partial r}|_{r=r_J} = \\ &\frac{\partial f_{JE}}{\partial r}|_{r=r_J} \cos(m\theta) = -2cmr_P^{2+m} r_J^{-m-1} \cos(m\theta). \end{aligned} \tag{A.16}$$

Now the magnetic field $\boldsymbol{B}_{WJ} = \boldsymbol{B}_J - \boldsymbol{B}_V$ produced by the surface currents can be expressed as

$$\begin{aligned} &\boldsymbol{B}_{WJ} = \oint_{\partial R} \boldsymbol{G}(x, y, r^* = r_J, \theta^*) \frac{\partial \psi_{JE}}{\partial n} ds = \\ &\int_0^{2\pi} \frac{1}{2\pi R} \frac{1}{R} \begin{pmatrix} y - r_J \sin\theta^* \\ r_J \cos\theta^* - x \end{pmatrix} (-2cmr_P^{2+m} r_J^{-m-1} \cos(m\theta)) r_J d\theta^* = \\ &- \frac{cmr_P^{2+m} r_J^{-m}}{\pi} \int_0^{2\pi} \frac{\cos(m\theta)}{(x - r_J\cos\theta^*)^2 + (y - r_J \sin\theta^*)^2} \begin{pmatrix} y - r_J \sin\theta^* \\ r_J \cos\theta^* - x \end{pmatrix} d\theta^*. \end{aligned} \tag{A.17}$$

It is possible to evaluate the integral separately for each component for a given m employing the Residue theorem. This was carried out for $m = 1, 2$ and 3 giving

$$\begin{aligned} \boldsymbol{B}_{WJ} = &- \frac{cmr_P^{2+m} r_J^{-m}}{\pi} 2\pi \left[\frac{r^{m-1}}{2r_J^m} \begin{pmatrix} \sin((m-1)\theta^*) \\ \cos((m-1)\theta^*) \end{pmatrix} \right] \\ &- cmr_P^{2+m} r_J^{-2m} r^{m-1} \begin{pmatrix} \sin((m-1)\theta^*) \\ \cos((m-1)\theta^*) \end{pmatrix}. \end{aligned} \tag{A.18}$$

[2] In the sense of $\mu_0 I = 1$

On the other side in the cylinder model the flux function corresponding to the field (e.g. for $r < r_J$) from the surface currents is known from 3.1.2 and can be turn into a magnetic field:

$$\boldsymbol{B}_{WJ} = -cmr_P^{2+m} r_J^{-2m} r^{m-1} \begin{pmatrix} \sin((m-1)\theta^*) \\ \cos((m-1)\theta^*) \end{pmatrix}. \tag{A.19}$$

This is the identical term as the one derived for the magnetic field from the surface currents with the developed approach. Thus the no-wall solution (equation 3.33) is validated in the cylindrical model.

A.4 Software implementation of the synthetic magnetics

The synthetic magnetics module SYNMAG is developed to run in three different operation modes as detailed in table A.1. The main steps in operation mode JOREK-ψ are listed in figure A.1.
Operation mode JOREK-ψ has some properties, which make it highly efficient. Most important, the chosen approach employs homogeneous PDEs only. Thus there is no necessity to carry out time consuming evaluations of the source term in every solver step. The domain, on which the partial differential equation is solved, is confined to the outer area $\Omega_A \setminus \Omega_J$. This is the main region of interest for the comparison with the experiment. Furthermore the complete extraction of JOREK data is happening in the initialization stage limiting these processes to the absolute minimum extent.
The operation mode JOREK-ψ is compared with respect to efficiency with operation mode JOREK-j. The latter mode is associated with calculation times, which are higher by a factor of about 6 compared to the operation mode JOREK-ψ.
The algorithm for Green's function has been adapted from the equilibrium solver CLISTE [81]. For the case, that the source point is in the absolute vicinity of the observation point, a special singularity treatment has been implemented.
Another problem was posed by the fact, that the chosen approach works on the basis of two different domains (Ω_A and $\Omega_A \setminus \Omega_J$). Hence it was necessary to develop an approach to superimpose entire flux functions evaluated by the used PED-solver. The line integral (figure A.1 - 3.1.3.) is evaluated in a discretized way. The density of the boundary points used for this discretisation is a crucial factor for the quality of the handover of the poloidal flux function from the domain from Ω_A to $\Omega_A \setminus \Omega_J$. Due to this the possibility of using several levels of boundary dicretisation have been implemented.
Figure A.2 shows the stages in the evaluation of ψ (operation mode: JOREK-ψ) as they are detailed in figure A.1. It can be seen that different calculation domains are used in different steps. As well the figure illustrates that ψ_V and ψ_{WA} vary on $\partial\Omega_A$, while the final solution ψ has a constant value on this boundary.

Table A.1: Operation modes of the synthetic magnetics module SYNMAG

Operation mode	Domain	Input data
JOREK-ψ	$\Omega_A \setminus \Omega_J$	$\partial\psi_J/\partial n$ on $\partial\Omega_J$
JOREK-j	Ω_A	j_J on Ω_J
Play	Ω_A	j as analytic input

1. Initialization
1.1. Initialize JOREK data structure
1.2. Derive geometry of Ω_J
1.3. Calculate for each boundary point $1/r\partial\psi_J/\partial n$
2. ψ_{hom} (PSL)
2.1. Create skeleton for Ω_A
2.2. Triangularization
2.3. Solve PDE:

$$\triangle^*\psi_{\mathrm{hom}} = 0$$
$$\psi_{\mathrm{hom}} = 0$$
$$\psi_{\mathrm{hom}} = 1$$

2.4. Evaluate PSL current
3. Loop over all time points
3.1. ψ_V
3.1.1. Create skeleton for $\Omega_A \setminus \Omega_J$
3.1.2. Triangularization
3.1.3. Solve PDE:

$$\triangle^*\psi_V = 0$$
$$\psi_V(\boldsymbol{r}) = \oint_{\partial\Omega_J} \frac{1}{r^*} G(\boldsymbol{r}, \boldsymbol{r}^*) \frac{\partial\psi_J}{\partial n} ds^* \text{ for } \boldsymbol{r} \in \partial\Omega_J \cup \partial\Omega_A$$

3.1.4. Calculate ψ_V at $\partial\Omega_A$
3.1.5. Evaluate PSL current
3.2. ψ_{WA}
3.2.1. Create skeleton
3.2.2. Triangularization
3.2.3. Solve PDE:

$$\triangle^*\psi_{WA} = 0$$
$$\psi_{WA} = -\psi_V \textit{ on } \partial\Omega_A$$

3.2.4. Evaluate PSL current
3.3. ψ
3.3.1. Evaluate coefficient c_{hom}
3.3.2. Carry out superposition: $\psi = \psi_V + \psi_{WA} + c_{\mathrm{hom}}\psi_{\mathrm{hom}}$
3.3.3. Evaluate synthetic signals
4. Finalization

Figure A.1: The main program steps of SYNMAG in the operation mode JOREK-ψ

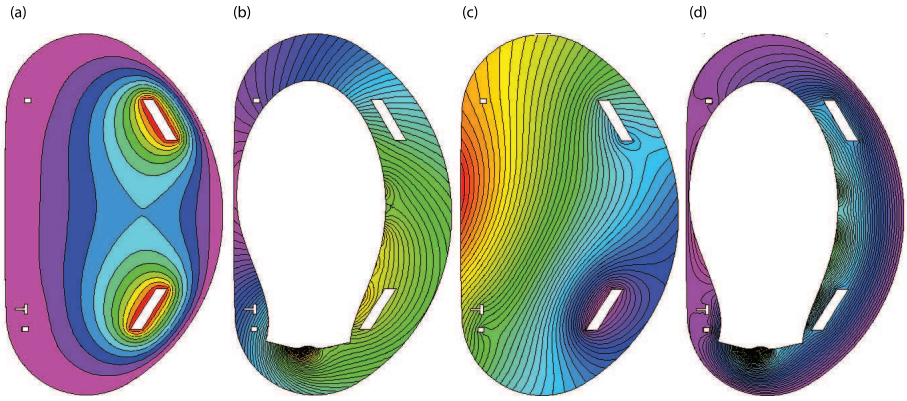

Figure A.2: Stages in the evaluation of ψ in operation mode JOREK-ψ ($c = 0.41 \times 10^{-3}$): (a) ψ_{hom}, (b) ψ_V, (c) ψ_{WA} and (d) ψ. The color code is not the same in all pictures.

Appendix B

Generalized linear least square fit

The toroidal components of a perturbation structure can be evaluated by Fourier analysis, if a number of equally spaced probes in identical poloidal positions are available. In case a set of not equally spaced probes in identical poloidal positions is available, it is possible to extract similar information by the application of a general least square fit [129].
The task is to fit a set of M data points (ϕ_i, B_i) to a linear combination of basis functions:

$$\begin{aligned} B(\phi) &= \sum_{k=1}^{M} a_k f_k(\phi), \\ f_{2l-1} &= \cos(l\phi) \text{ and } f_{2l} = \sin(l\phi) \ (l = 1, ..., M/2) \end{aligned} \tag{B.1}$$

The a_k are chosen to minimize the merit function

$$\chi^2 = \sum_{i=1}^{N} \left[\frac{B_i - \sum_{k=1}^{M} a_k f_k(\phi_i)}{\sigma_i} \right]^2, \tag{B.2}$$

where σ_i represent the measurement errors of the individual probes. If the errors are unknown but the probes are identical, they can be set to 1. The minimum of the merit function occurs, when its derivatives with respect to all M parameters a_k vanishes:

$$0 = \sum_{i=1}^{N} \left[B_i - \sum_{k=1}^{M} a_k f_k(\phi_i) \right] f_k(\phi_i) \text{ for } k = 1, ..., M \tag{B.3}$$

On the basis of this the coefficients a_k can be calculated by means of linear algebra.

Bibliography

[1] *World energy outlook 2011*, IEA, International Energy Agency OECD, Paris, 2011.

[2] *Climate change 2007 : synthesis report*, IPCC, Geneva, Switzerland, 2008.

[3] HUBA, J. D., *NRL PLASMA FORMULARY Supported by The Office of Naval Research*, Naval Research Laboratory, 2011.

[4] WESSON, J. A., *Tokamaks*, Clarendon Press - Oxford, 2004.

[5] GREEN, B. J. et al., Plasma Physics and Controlled Fusion **45** (2003) 687.

[6] ZOHM, H., Contribution to SOFT conference 2012 (2012).

[7] SCHITTENHELM, M. et al., Nuclear Fusion **37** (1997) 1255.

[8] SAIBENE, G. et al., Plas.Phys.Contr.Fusion **44** (2002) 1769.

[9] REIMERDES, H., *MHD Stability Limits in the TCV Tokamak*, PhD in Physics, Ecole Polytechnique Fédérale de Lausanne, 2001.

[10] WAGNER, F. et al., Physical Review Letters **49** (1982) 1408.

[11] WAGNER, F., Plasma Physics and Controlled Fusion **49** (2007) B1.

[12] FINKEN, K. et al., Nuclear Fusion **47** (2007) 522.

[13] ERCKMANN, V. et al., Phys. Rev. Lett. **70** (1993) 2086.

[14] SCHNEIDER, P. A., *Characterization and scaling of the tokamak edge transport barriert*, PhD in Physics, Ludwig Maximilians Universität München, 2012.

[15] BIGLARI, H. et al., Physics of Fluids B: Plasma Physics **2** (1990) 1.

[16] TERRY, P. W., Rev. Mod. Phys. **72** (2000) 109.

[17] DOYLE, E. J. et al., Physics of Fluids B: Plasma Physics **3** (1991) 2300.

[18] ASDEX Team, Nuclear Fusion **29** (1989) 1959.

[19] BURRELL, K. H., Physics of Plasmas **6** (1999) 4418.

[20] IDA, K., Plasma Physics and Controlled Fusion **40** (1998) 1429.

[21] SCHIRMER, J. et al., Nuclear Fusion **46** (2006) S780.

[22] HINTON, F. L. et al., Rev. Mod. Phys. **48** (1976) 239.

[23] SAUTER, O. et al., Physics of Plasmas **6** (1999) 2834.

[24] SAUTER, O. et al., Physics of Plasmas **9** (2002) 5140.

[25] BERGMANN, A. et al., 39th EPS Conference on Controlled Fusion and Plasma Physics (2012).

[26] DUNNE, M. et al., 39th EPS Conference on Controlled Fusion and Plasma Physics **39** (2012).

[27] FEDERICI, G. et al., Plasma Physics and Controlled Fusion **45** (2003) 1523.

[28] ZOHM, H., Plasma Physics and Controlled Fusion **38** (1996) 105.

[29] BURRELL, K. H. et al., Plasma Physics and Controlled Fusion **44** (2002) A253.

[30] GAROFALO, A. et al., Nuclear Fusion **51** (2011) 083018.

[31] LANG, P. et al., Nuclear Fusion **43** (2003) 1110.

[32] WENNINGER, R. P. et al., Plasma Physics and Controlled Fusion **53** (2011) 105002.

[33] EVANS, T. E. et al., Phys. Rev. Lett. **92** (2004) 235003.

[34] HUYSMANS, G. et al., Nuclear Fusion **47** (2007) 659.

[35] HERRMANN, A. et al., Fusion Science and Technology **44** (2003) 569.

[36] Coda for the TCV team, S., Nuclear Fusion **51** (2011) 094017.

[37] FUNDAMENSKI, W. et al., Plasma Physics and Controlled Fusion **49** (2007) R43.

[38] HUYSMANS, G. T. A., Plasma Physics and Controlled Fusion **47** (2005) B165.

[39] NUNES, I. et al., Nuclear Fusion **44** (2004) 883.

[40] BURCKHART, A. et al., Plasma Physics and Controlled Fusion **52** (2010) 105010.

[41] LOARTE, A. et al., Plasma Physics and Controlled Fusion **45** (2003) 1549.

[42] LOARTE, A. et al., Physics of Plasmas **11** (2004) 2668.

[43] EICH, T. et al., J.Nucl.Mater. **337-339** (2005) 669.

[44] PETRIE, T. et al., Nuclear Fusion **43** (2003) 910.

[45] KALLENBACH, A. et al., Nuclear Fusion **48** (2008) 085008.

[46] LAUX, M. et al., 28th EPS Conference on Controlled Fusion and Plasma Physics **28** (2001).

[47] PETRIE, T. et al., Journal of Nuclear Materials **196-198** (1992) 848 .

[48] KIRK, A. et al., Physical Review Letters **96** (2006) 185001.

[49] EICH, T. et al., Physical Review Letters **91** (2003) 195003.

[50] KIRK, A. et al., Physical Review Letters **92** (2004) 245002.

[51] KIRK, A. et al., Plasma Physics and Controlled Fusion **49** (2007) 1259.

[52] LINKE, J. et al., Journal of Nuclear Materials **367-370, Part B** (2007) 1422 .

[53] FREIDBERG, J. P., *Ideal magnetohydrodynamics*, Plenum Press, New York, 1987.

[54] BRAMBILLA, M., *Kinetic Theory of Plasma Waves*, Oxford University Press, 1998.

[55] CONNOR, C. W. et al., Proc. R. Soc. Lond. A **365** (1979) 1.

[56] GROEBNER, R. J. et al., Physics of Plasmas **5** (1998) 1800.

[57] WESSON, J., Nuclear Fusion **18** (1978) 87.

[58] MANICKAM, J., Physics of Fluids B: Plasma Physics **4** (1992) 1901.

[59] LAVAL, G. et al., Physics of Fluids **17** (1974).

[60] CONNOR, J. W. et al., Physics of Plasmas **5** (1998) 2687.

[61] WEBSTER, A. J. et al., Phys. Rev. Lett. **102** (2009) 035003.

[62] WILSON, H. R. et al., Plasma Physics and Controlled Fusion **48** (2006) A71.

[63] DEGTYAREV, L. et al., Computer Physics Communications **103** (1997) 10 .

[64] PITZSCHKE, A. et al., Plasma Physics and Controlled Fusion **54** (2012) 015007.

[65] OZEKI, T. et al., Nuclear Fusion **30** (1990) 1425.

[66] SAARELMA, S. et al., Plasma Physics and Controlled Fusion **47** (2005) 713.

[67] THOMAS, D. M. et al., Phys. Rev. Lett. **93** (2004) 065003.

[68] BURCKHART, A. et al., 39th EPS Conference on Controlled Fusion and Plasma Physics **39** (2012).

[69] SNYDER, P. B. et al., Physics of Plasmas **9** (2002) 2037.

[70] SNYDER, P. B. et al., Physics of Plasmas **12** (2005) 056115.

[71] COWLEY, S. et al., Plas.Phys.Contr.Fusion **45** (2003) A31.

[72] WILSON, H. R. et al., Physical Review Letters **92** (2004) 175006.

[73] CONNOR, J. W., Plas.Phys.Contr.Fusion **40** (1998) 191.

[74] STRAUSS, H. R., Physics of Fluids **19** (1976) 134.

[75] STRAUSS, H. R., Journal of Plasma Physics **57** (1997) 83.

[76] KRUGER, S. et al., 25th EPS Conference on Controlled Fusion and Plasma Physics **25** (1996).

[77] PAMELA, S., *Simulation Magnéto-Hydro-Dynamiques des Edge-Localised-Modes dans un tokamak*, PhD in Physics, Laboratoire de Physique des Ioniques et Moléculaires (PIIM) de Provence, 2010.

[78] HOLZL, M. et al., Physics of Plasmas **19** (2012) 082505.

[79] CZARNY, O. et al., Journal of Computational Physics **227** (2008) 7423 .

[80] HéNON, P. et al., Parallel Computing **34** (2008) 345 .

[81] CARTHY, P. J. M., Physics of Plasmas **6** (1999) 3554.

[82] BANK, R. E., *PLTMG: A Software Package for Solving Elliptic Partial Differential Equations. Users' Guide 10.0*, Department of Mathematics, University of California at San Diego, 2007.

[83] LANDAU, L. D. et al., *Electrodynamics of Continuous Media*, Pergamon Press, Moscow, 1984.

[84] GERNHARDT, J., IPP-Report **1/262** (1992).

[85] SCHMID, A., *Charakterisierung von Plasmauktuationen mit einer kombinierten Mirnov-Langmuir-Sonde am Tokamak ASDEX Upgrade*, Diploma thesis, Technische Universität München, 2005.

[86] SCHMID, A., IPP-Report **10/35** (2008).

[87] BOOM, J. et al., Nuclear Fusion **51** (2011) 103039.

[88] RATHGEBER, S. et al., Plas.Phys.Contr.Fusion, submitted (2012).

[89] KURZAN, B. et al., Review of Scientific Instruments **82** (2011) 103501.

[90] SCHORN, R. P. et al., Applied Physics B: Lasers and Optics **52** (1991) 71.

[91] SCHWEINZER, J. et al., Plasma Physics and Controlled Fusion **34** (1992) 1173.

[92] FISCHER, R. et al., Plasma Physics and Controlled Fusion **50** (2008) 085009.

[93] VIEZZER, E. et al., Review of Scientific Instruments, accepted (2012).

[94] CUPIDO, L. et al., Review of Scientific Instruments **77** (2006) 10E915.

[95] FISCHER, R. et al., Plasma Physics and Controlled Fusion **45** (2003) 1095.

[96] MORET, J.-M. et al., Review of Scientific Instruments **69** (1998) 2333.

[97] RYTER, F. et al., Nuclear Fusion **49** (2009) 062003.

[98] ROSSEL, J. et al., Nuclear Fusion **52** (2012) 032004.

[99] BRAAMS, B. J., Plasma Physics and Controlled Fusion **33** (1991) 715.

[100] KURZAN, B. et al., Physical Review Letters **95** (2005) 145001.

[101] SNYDER, P. et al., Nuclear Fusion **49** (2009) 085035.

[102] KENDL, A. et al., Physics of Plasmas **17** (2010) 072302.

[103] SY, F., *Diagnostic mapping of solitary magnetic perturbations*, Bachelor thesis, Technische Universität München, 2012.

[104] SOMMER, F. et al., Plasma Physics and Controlled Fusion **53** (2011) 085012.

[105] KOSLOWSKI, H. et al., Nuclear Fusion **45** (2005) 201.

[106] SOLANO, E. R. et al., Physical Review Letters **104** (2010) 185003.

[107] STRAIT, E. J. et al., Physics of Plasmas **4** (1997) 1783.

[108] KASS, T. et al., Nuclear Fusion **38** (1998) 111.

[109] PEREZ, C. et al., Nuclear Fusion **44** (2004) 609.

[110] EICH, T. et al., Journal of Nuclear Materials **390-391** (2009) 760 .

[111] VIANELLO, N. et al., Physical Review Letters **106** (2011) 125002.

[112] KIRK, A. et al., Plasma Physics and Controlled Fusion **47** (2005) 995.

[113] VALOVIC, M. et al., 21th EPS Conference on Controlled Fusion and Plasma Physics (1994).

[114] BECOULET, M. et al., Plasma Physics and Controlled Fusion **45** (2003) A93.

[115] BOBKOV, V. et al., 31th EPS Conference on Controlled Fusion and Plasma Physics (2004).

[116] NEUHAUSER, J. et al., Nuclear Fusion **48** (2008) 045005.

[117] VIEZZER, E. et al., Nuclear Fusion, submitted (2012).

[118] UZAWA., K. et al., Plasma Fusion Research **5** (2010) S1016.

[119] SCHMID, A. et al., 34th EPS Conference on Controlled Fusion and Plasma Physics (2007).

[120] REIMERDES, H. et al., Phys. Rev. Lett. **88** (2002) 105005.

[121] DRAZIN, P., *Solitons : an introduction*, Cambridge University Press, Cambridge England New York, 1989.

[122] WENNINGER, R. et al., Nuclear Fusion **52** (2012) 114025.

[123] DA GRAçA, S. et al., Plasma Physics and Controlled Fusion **49** (2007) 1849.

[124] MUELLER, H. W. et al., Contributions to Plasma Physics **50** (2010) 847.

[125] LUNT, T. et al., Nuclear Instruments and Methods in Physics Research Section A: Accelerators, Spectrometers, Detectors and Associated Equipment **623** (2010) 812 .

[126] KREBS, I., *Non-Linear reduced MHD Simulations of Edge-Localized Modes in Realistic ASDEX Upgrade Geometry*, Master thesis, Ludwig Maximilians Universität, München, 2012.

[127] BEURSKENS, M. et al., Nuclear Fusion **49** (2009) 125006.

[128] NOLD, B. et al., Plasma Physics and Controlled Fusion **52** (2010) 065005.

[129] VETTERLING, W. T. et al., *Numerical Recipes - Example*, Cambridge University Press, Cambridge, 2. aufl. edition, 1992.

Acknowledgments

I want to express my deep thankfulness to many people for their support contributing to the development of this thesis:

- Hartmut Zohm has acted as my direct adviser at the Max-Planck-Institut für Plasmaphysik. With a combination of excellent proposals and ideas and a very positive attitude he enabled me to address tough scientific challenges in an appropriate way. He has contributed a considerable amount of his time and energy in discussions with me. Thanks to this cooperation I was able to significantly extent my knowledge on plasma physics and MHD. Working with him is always an instructive pleasure.

- Harald Lesch has enabled me to do a doctorate at the faculty of physics at the Ludwig-Maximilians-Universität, Munich, Germany. Having him as thesis supervisor was highly motivating to me.

- A number of people supported the development of this thesis in a particular way. In numerous stimulating discussions on science and beyond Thomas Eich gave me absolutely appreciable advice. He helped me to make my abstracts understandable and successful. Josef Neuhauser was always ready to share his extensive knowledge on ELMs with me. Valentin Igochine helped me to get up and running with the development of the synthetic magnetic diagnostic. In the phase of completion of the thesis I was strongly supported by Darren McDonald and Bernhard Siegling. Furthermore I often used the opportunities arising from the presence of the people around me - in particular Timothy Stoltzfus-Dück and Alexander Bock.

- Also Sibylle Günter, Karl Lackner, Ulrich Stroth and Thomas Sunn Pedersen shared their extensive expertise with me and gave me highly beneficial advice during the development of this thesis.

- Mike Dunne and Andreas Burckhart have supported me on equilibrium reconstruction and linear stability calculations. A number of colleagues have spent time with me to discuss questions related to a large set of diagnostics and related analysis: Matthias Bernert, Jurrian Boom, Rainer Fischer, Manuel Garcia-Munoz, Sylvie da Graça, Louis Giannone, Bernd Kurzan, Tilmann Lunt, Marc Maraschek, Rachael McDermott, Alexander Mlynek, Hans Werner Müller, Sylvia Rathgeber, Philip Schneider, José Vicente, Eleonora Viezzer, Matthias Willensdorfer

- In general the climate at ASDEX Upgrade is characterized by a high level of willingness to help. In particular I have received valuable advice and support from Volodymyr Bobkov, Ivo Classen, Garrad Conway, Ralph Dux, Christoph Fuchs, Albrecht Herrmann, Jörg Hobirk, Arne Kallenbach, Otto Kardaun, Martin Kocan, Peter Lang,

Bernhard Nold, Thomas Pütterich, Matthias Reich, Patrick McCarthy, Francois Ryter, Pierre Sauter, Josef Schweinzer, Fabian Sommer, Jörg Stober, Wolfgang Suttrop, Frithjof Sy, Wolfgang Treutterer, Arthur Weller, Elisabeth Wolfrum and Hans-Peter Zehrfeld.

- Matthias Hölzl gave me all the assistance with respect to JOREK I could have wished. Furthermore Guido Huysmans was always prepared to discuss countless questions on MHD. Like there, it was always my aim to establish connections between experimental observations and theory. Without the support from Wolf-Christian Müller, Omar Maj, Emanuele Poli, Andreas Bergmann, Emiliano Fable, Tiago Ribeiro and Alessandro Biancalani this would have been much more difficult.

- The cooperation with CRPP was extremely efficient, professional and enjoyable. Especially Holger Reimerdes acted as the perfect contact for any type of TCV related problems. Above that he and Olivier Sauter gave me exceptional advice with respect to data analysis and connection to theory, which has strongly accelerated the progression to important results. Furthermore Jonathan Rossel, Andreas Pitzschke, Sergei Medvedev, Anthony Cooper and Basil Duval have helped me in the analysis of TCV data.

- Europe has a very strong fusion community. I am glad that I had excellent cooperation with a number of its key specialists. Among these are Duarte Borba, Alexander Kendl, Andrew Kirk, Gabor Kocsis, Alberto Loarte, Nicola Vianello, Sandor Zoletnik, Peter de Vries and Howard Wilson.

- Finally I always enjoyed a strong support by my wife Christina, my parents and my parents-in-law. Also my son Victor contributed by doing without the presence of his daddy in numerous situations.

All this support, ideas and encouragement were a key to the development of the scientific novelties gathered in this thesis. Again I would like to emphasize how much I appreciate this!